Search for solar axions with the Time Projection Chamber of the CERN Axion Solar Telescope with 4-Helium as buffer gas

Memoria presentada por
Jaime Ruz Armendáriz
para optar al grado de Doctor
en Ciencias Físicas

Laboratorio de Física Nuclear y Altas Energías
Departamento de Física Teórica
Área de Física Atómica, Molecular y Nuclear
Universidad de Zaragoza

September 2008

Acknowledgements

I would like to thank Professor Julio Morales, who gave me the oportunity to join the Particle Physics group of the Zaragoza University. I am really thankful that he has always believed in me. His knowledge, guidance and advice have always been an inspiration for me.

I also feel deeply grateful to Igor G. Irastorza. He, who I will always consider a friend, has adviced me at any time. Working with him has been an exciting experience from which I have learnt statistical and data analysis techniques, detector development and appropiate tunning of experimental setups.

The present thesis aims to summarize part of the work that I have developed within the CAST collaboration. Its subject is the analysis of the data gathered by the TPC detector during the ^{4}He run of the CAST experiment. Therefore, I would really like to thank all the TPC group that has contributed setting up the detector. Specially to Luigi Di Lella and Igor G. Irastorza, without their contribution the TPC would have just been a dream. I would also like to mention the help and unconditional support that I have experienced from every professor and colleague in the Zaragoza Particle Physics Group.

The experience of working and living at CERN is one of my warmest memories. I will gratefully remember the whole CAST group. Specially Prof. Konstantin Zioutas and Martyn Davenport: thanks for making CAST real and for keeping our dreams alive. I must say that you will always be a reference for me. We have spent so many hours together in the experiment that I am already missing it.

CERN has been a wonderful experience for me, but it would have not been such without the support of all my friends: Julia, Igor, Theopisti, Thomas, Hector, Asun, Silvia, Biljana, Daniel, Nuno, David, Javier ... and a large queue to whom I beg their perdon for not being mention. Special thanks to the friends that from the distance have always cared for me and to those that are thinking of me, you always managed to put a smile on my face.

Viele danke Julia, du bist meine inspirationsquelle.

I feel really lucky and indeed proud to have been accompanied and supported in all situations of my life by my family. My sincerest appretiation and my utmost respect belong to my mother Ana María, my father Rafael and my dear brother Jorge. My love and gratitud belongs to them.

"A mis padres, Ana María y Rafael, por vuestro inconmensurable apoyo, por creer en mí y darme todo lo que soy. Y a mi hermano Jorge, quien siempre está a mi lado, dándome ánimo en todo momento. Sin vosotros mi vida no tendría sentido."

Jaime Ruz Armendáriz

Contents

Chapter 1

Introduction

Quantum chromodynamics, also known as QCD, is the proposed theory of the so-called strong interactions that bind quarks and gluons together to form hadrons, the constituents of nuclear matter.

In order to explain the asymmetry that exist between matter and antimatter in the Universe, *CP-symmetry* must be violated. Besides the fact that the weak interaction slightly violates *CP-symmetry*, this feature has not been yet observed in the quantum chromodynamics field theory, althought it is an expected consequence.

The so-called quantum chromodynamics strong *CP-problem* might be solved by the introduction of a chiral symmetry that leads to the existence of a new pseudo-scalar particle. The Peccei-Quinn mechanism to protect the strong force from *CP-violating* effects, and which results in the axion, has endured for thirty years and is widely generally regarded as the best and most attractive solution to the strong *CP-problem*.

For axions, the ratio between mass and photon-coupling is given, up to model-dependent numerical factors, by the corresponding pion properties. This defines the "axion line" in the parameter plane of mass and photon coupling strength. Cosmological arguments point out that axions with eV-range masses would have thermalized in the early universe by their generic pion interactions and thus contribute to a hot dark matter component of the universe, similar to

neutrinos. At the present time, structure formation of the Universe constraints the axion masses to be below 1eV.

The axion, appart from being able to solve the strong *CP-problem*, is one of the two outstanding candidates to constitute the dark matter of the universe, along with the neutralino or WIMP.

There is a remarkable interest on axions, the rapidly growing experimental effort in axions around the world: CAST at CERN looking for solar axions, ADMX in the U.S. & CARRACK in Japan looking for dark matter axions, and more than half a dozen photon regeneration projects and proposals in various stages that have check the lately "excluded" anomaly of magnetically-induced vacuum birefringence and dichroism found by the PVLAS collaboration in Italy.

The CERN Solar Axion Telescope (CAST) is the most sensitive implementation of the "helioscope" concept to look for hypothetical axions (or axion-like particles) coming from the Sun. Axions can be produced via the so-called Primakoff effect in the presence of strong electromagnetic fields. The solar core is an ideal environment to produce them due to the strength of the solar plasma electric fields. In such conditions, a photon produced in the solar core might couple to the virtual photon of the electromagnetic fields and result in an axion that could be able to reach the Earth's surface. Those axions, could be reconverted into X-ray photons in a magnetic field.

CAST makes use of a decommissioned LHC prototype magnet with a length of 9.26 m that provides a 9 Tesla field to trigger the Primakoff conversion of solar axions into X-ray. Those photons can then be detected by the three different X-ray detectors placed at both ends of the magnet: a Time Projection Chamber, a sunsrise MICROMEGAS and a Charge Coupled Device, this last one together with an X-ray telescope that enhaces the signal-to-background ratio, which improves the sensitivity of the experiment.

Due to coherence requirements, during the First Phase (years 2003 and 2004), CAST was sensitive to axion masses under 0.02 eV. The loss of coherence over the full magnet length of CAST encountered while the magnet bores were under vacuum is restored for the Second Phase of the experiment by using a

buffer gas such that the arising photon from the Primakoff conversion acquires an effective mass. By varying the gas and its pressure the search for axions with higher masses is possible.

The Second Phase of CAST uses two different gases: the ^{4}He allows to look for axions with masses up to 0.39 eV, while the use of ^{3}He extends the sensitivity up to masses of about 1.2 eV.

Together with Tokio, CAST has been the first laboratory experiment to reach a sensitivity where the existence of "invisible axions" is tested. All previous experiments, including the CAST vacuum phase, were only able to search for generic axion-like particles with masses much smaller than the ones that would be expected if they are indeed responsible for solving the strong *CP-problem*.

As a tuning experiment planning to explore the axion mass region up to 1.2 eV, CAST would also be sensitive to the existence of large extra dimensions. The detection of X-ray at least in two gas-pressures inside the magnetic pipes can be the potential new signature of (two) large extra dimensions with the compactification radius down to around 170 nm.

The aim of the present book is to summarize the work that has been developed during the ^{4}He run using the TPC X-ray detector of the CAST experiment in order to look for solar axions.

CAST data taking procedure during its Second Phase has been choosen in a way such that allows to scan for axion masses from 0.02 to 1.20 eV in little steps. The procedure used for the ^{4}He run during the years 2005 and 2006 was to daily increase the ^{4}He gas density in the magnet bore, mechanism that has allowed CAST to restore the coherence for axion masses up to 0.39 eV.

The first part of this book introduces the theoretical motivation for the axion searches. The axion properties and its production mechanisms will be reviewed in the Chapters 2, 3 and 4. The second part is devoted to the description of both, the CAST experiment and the TPC detector, which will set the proper framework for the introduction of the third part of the book where the method applied for the analysis of the TPC data is explained and the final results are presented.

The TPC detector has been able to look for axions with masses below 0.39 eV during the Second Phase of the CAST experiment. As a result, the TPC is able to set a stronger limit to the axion-to-photon coupling in the axion mass range from 0.02 to 0.39 eV.

This work has been supported by the MEC (former CICyT) under the project FPA2004-00973 and thanks to the spanish fellowship BES-2005-8542.

Part I

Axions

Chapter 2

Axion motivation

Quantum chromodynamics, also known as QCD, is the proposed theory of the so-called strong interactions, which bind quarks and gluons together to form hadrons, the constituents of nuclear matter. It describes the formation of protons and neutrons, the mediation of the forces between hadrons and describes the nuclei formation.

2.1 The quantum chromodynamics Lagrangian

Quantum chromodynamics is a gauge theory of the non-Abelian[1] $SU(3)$ group obtained by taking the color charge to define a local symmetry. In physics, gauge theories are based on the idea that symmetry transformations can be performed locally as well as globally.

Most powerful physical theories are described by Lagrangians which are invariant under certain symmetry transformation groups. In the case of being invariant under a tranformation identically performed at every space-time point it is said they have a global symmetry. Gauge theory extends this idea by requiring that the Lagrangians posses local symmetries under transformations performed independently for for every space-time point.

In quantum physics, a symmetry is a transformation between physical states that preserves the expectation values of all observables O, in particular of the Hamiltonian. Let S represent a symmetry transformation between the initial state $|\varphi\rangle$ and the final physical state $|\psi\rangle$, then:

$$\begin{aligned} |\varphi\rangle \rightarrow |\psi\rangle = S|\varphi\rangle \\ |\langle\varphi|O|\varphi\rangle|^2 = |\langle\psi|O|\psi\rangle|^2. \end{aligned} \tag{2.1}$$

The importance of gauge theories for physics is based in the success of the mathematical formalism in providing a unified framework to describe quantum field theories for *electromagnetism*, the *weak force* and the *strong force*. This theory, known as the *Standard Model*, accurately describes the experimental results regarding three of the four fundamental forces of nature, and is a gauge theory with the gauge group $SU(3) \times SU(2) \times U(1)$.

The strong force is described by the QCD Lagrangian. Once the generators of $SU(3)$ are chosen, this gauge invariant Lagrangian can be written as

$$\mathcal{L}_{QCD} = \bar{\psi}\left(i\gamma^\mu \partial_\mu - m\right)\psi - g\left(\bar{\psi}\gamma^\mu \lambda_a \psi\right) G^a_\mu - \frac{1}{4} G^a_{\mu\nu} G^{\mu\nu}_a, \tag{2.2}$$

where ψ represents the quark field and G^a_μ are the eight gauge fields. In the

[1] Non-Abelian is a non conmutative group.

equation, γ^μ are the Dirac matrices and λ_a the generators chosen for the $SU(3)$ group, the Gell-Mann matrices. The term labeled $G^a_{\mu\nu}$ represents the equivalent to the electromagnetic tensor $F^{\mu\nu}$ found in quantum electrodynamics[2] for each generator of the group $SU(3)$: where G^a_μ is the equivalent to the 4-vector potential of the electromagnetic tensor for this theory, and f_{abc} are the structure constants which need to be introduced owing to the commutation relations between the Gell-Mann matrices:

$$G^a_{\mu\nu} = \partial_\mu G^a_\nu - \partial_\nu G^a_\mu - g f_{abc} G^b_\mu G^c_\nu. \tag{2.3}$$

Each flavor of quark belongs to the fundamental representation $SU(3)$ and contains a triplet of fields together denoted by ψ, while the antiquark field $\bar{\psi}$ belongs to the complex conjugate representation (3^*) containing as well a triplet of fields as shown in *equation (2.4)*. The gluon contains an octect of fields that belong to the adjoint representation (8), and using the Gell-Mann matrices it can be written as $G_\mu = G^a_\mu \lambda_a$.

$$\psi = \begin{pmatrix} \psi_1 \\ \psi_2 \\ \psi_3 \end{pmatrix} \qquad \bar{\psi} = \begin{pmatrix} \bar{\psi}^*_1 \\ \bar{\psi}^*_2 \\ \bar{\psi}^*_3 \end{pmatrix} \tag{2.4}$$

The rest of particles belong to the trivial representation (1) of color $SU(3)$. In the simple language introduced previously, the three indices $1, 2, 3$ of the quark triplet of *equation (2.4)* are usually identified with the three colors.

The color of a gluon is similary given by the a index in the Lagrangian of *equation (2.2)*, index that corresponds to the paticular Gell-Mann matrix it is associated with. This matrix has indices i and j, the color labels on the gluon. Therefore, at the interaction vertex, one has $q_i \to g_{ij} + q_j$ and the color-line representation tracks these indices *(see figure 2.1)*.

[2]Quantum electrodynamics is also know by the acronym QED

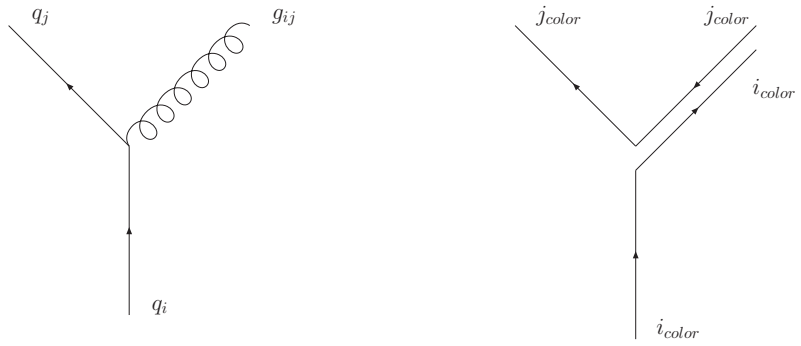

Figure 2.1: *Diagram of interaction between quarks with different color charge i and j mediated by a gluon g_{ij}. On the right diagram, the color lines conservation coming from the non gauge invariance.*

2.2 CP-invariance in quantum chromodynamics

This symmetry, *CP*, is the product of two symmetries, C for charge conjugation an P for parity. *CP-symmetry* must be violated in order to explain the asymmetry that exist between matter and antimatter in the Universe. Its violation, discovered in the neutral kaon decays[3] makes such a symmetry a vibrant area of study.

2.2.1 C-symmetry

In physics, *C-symmetry* is the symmetry of physical laws under charge conjugation transformation, obeyed by electromagnetism, gravity and the strong interaction, but violated by the weak interactions. Electromagnetism laws are invariant under the transformation that sustitute a charge q for a charge $-q$ and the directions of the electric and magnetic fields are reversed, preserving in that sense the dynamics behind the electromagnetic laws. In elementary particle physics, this would mean the following transformations:

[3]The discovery of *CP* violation was made by James Cronin and Val Fitch regarded with the Nobel Prize in Physics in the year 1980 for such a discovery.

$$\begin{array}{rcl} \psi & \rightarrow & -i(\bar{\psi}\gamma^0\gamma^2)^T \\ \bar{\psi} & \rightarrow & -i(\gamma^0\gamma^2\psi)^T \\ A^\mu & \rightarrow & -A^\mu. \end{array} \tag{2.5}$$

Such transformations do not alter the chirality of particles. in that sense, a left-handed neutrino under the transformation above described will transform into a left-handed antineutrino, which does not exist. Therefore, the charge conjugation is not a symmetry of the weak interactions.

2.2.2 P-symmetry

In physcis, a *parity transformation* is the simultaneous flip in the sign of all spatial coordinates

$$P: \quad \begin{pmatrix} x \\ y \\ z \end{pmatrix} \rightarrow \quad \begin{pmatrix} -x \\ -y \\ -z \end{pmatrix}. \tag{2.6}$$

A 3×3 matrix representation for P would have determinant equal to -1, and hence it cannot be reduced to a rotation.

Classical geometrical objects can be classified under rotations into scalars, vectors and tensors of higher rank. A clasification of particles could be given by parity as follows:

- *Scalars (P=1)* and *Pseudoscalars (P=-1))* which are rotationally invariant.
- *Vectors (P=-1)* and *Axial vectors (P=1)* which both transform as vectors under rotation.

An example of this kind of classification can be provided if we focus in classical mechanics. For example, let us have a look to Newton's equation of motion when mass is conserved, $\vec{F} = m\vec{a}$, which indicates that is a vector that scale with the mass to the acceleration vector. If we make a parity transformation to the equation of motion, the acceleration vector and the force will inmediatly transform. However, angular momentum is an axial vector $\vec{L} = \vec{r} \times \vec{p}$ and then by the parity transformation $P(\vec{L}) = (-\vec{r}) \times (-\vec{p}) = \vec{L}$, invariant under parity

transformation.

In quantum mechanics, space time transformations act on the quantum states, being the parity transformation P a unitary operator acting on a state $P\psi(\vec{r}) = \psi(-\vec{r})$. It can also be noticed that in general $P^2\psi(\vec{r}) = e^{i\varphi}\psi(\vec{r})$, since an overall phase is unobservable.

The operator P^2 reverses the parity of a state twice and leaves the spacetime invariant. In that sense it is an internal symmetry that rotates the eigenstates by phases $e^{i\varphi}$. If P^2 is an element e^{iR} of a continuous $U(1)$ symmetry group of phase rotations, then $e^{-iR/2}$ is part of this $U(1)$ and so is also a symmetry. The parity of a multiparticle state is the product of the parities of each state; parity is a *multiplicative quatum number*.

In quantum mechanics, Hamiltonians are invariant under a parity transformation if P commutes with the Hamiltonian. This happens for any scalar potential $V = V(r)$ in non-relativistic quatum mechanics, which means that no transition between states of opposite parity occur.

For quantum field theory, if we can show that the vacuum state is invariant under parity, $P|0\rangle = |0\rangle$, that the Hamiltonian is parity invariant and the quantization conditions do not change under parity, then this means that every state has a good parity, and this parity is conserved in any reaction.

Although parity is conserved in electromagnetism, strong interactions and gravity, it turns out to be violated in weak interactions. The Standard Model incorporates parity violation by expressing the weak interaction as a chiral gauge interaction. Only the left-handed components of particles and right-handed components of antiparticles participate in weak interactions in the Standard Model.

2.2.3 CP-symmetry

Strong interactions and electromagnetism are invariant under the CP transformation, but the weak interaction slightly violates it. *CP-symmetry* was originally proposed after the discovery of *P-symmetry* violation[4].

[4]The violation of *P-symmetry*, was verified in the beta decay of the ^{60}Co nuclei. The proposal came from Tsung-Dao Lee and Chen Ning Yang in 1956, but it was Chien-Shrung-

It was believed that *C-symmetry* could be combined with the parity inversion transformation and then *CP-symmetry* would be the one conserved. However, the observed asymmetry between mater and antimater in the Universe, appear as a consequence of *CP-symmetry* violation[5].

In the Standard Model, this *CP* violation is due to a single phase in the Cabbibo-Kowayashi-Maskawa[6] matrix, which contains the quark mixing flavor information on the strength of weak decays and specifies the mismatch of the quantum states of quarks when they propagate freely and when they take part in weak interactions. This mixing was introduced for two generations of quarks by Nicola Cabbibo and later on was generalized to three generations by M.Kobayashi and T.Maskawa:

$$\begin{pmatrix} V_{ud} & V_{us} & V_{ub} \\ V_{cd} & V_{cs} & V_{cb} \\ V_{td} & V_{ts} & V_{tb} \end{pmatrix} \begin{pmatrix} |d\rangle \\ |s\rangle \\ |b\rangle \end{pmatrix} = \begin{pmatrix} |d'\rangle \\ |s'\rangle \\ |b'\rangle \end{pmatrix}. \tag{2.7}$$

Let us assume that there exist N generations of quarks; then, there will be $2N$ flavors. A matrix $N \times N$ contains $2N^2$ real numbers, from which N^2 are fixed real numbers due to the unitary condition of the matrix, and $2N-1$ of the rest can be absorbed as phases for each quark field, which leaves $(N-1)^2$ free variables. Of these, $N(N-1)/2$ are rotation angles called quark mixing angles, and the remaining $(N-1)(N-2)/2$ are complex phases, cause of *CP* violation.

For the case *N=2*, there is only one parameter, which is a mixing angle between two generations of quarks, but the Standard Model has three generations of quarks, for which we have three mixing angles and one *CP-violating* complex phase.

2.2.4 CPT-symmetry

Since violation of *CP* was discovered in a kaon decay in 1964, a weaker version of the symmetry was proposed in order to be preserved by physical

Wu who carried the experimental confirmation in 1957.

[5]The violation of *CP-symmetry* has been observed even in weak interactions. Kaons and B mesons no longer conserve *CP*.

[6]Also known as the CKM matrix.

phenomena. The so-called *CPT-symmetry* introduces to *CP-symmetry* a time reversal transformation that is called *T-symmetry*. Invariance under time implies that whenever a motion is allowed by the laws of physics, the reversed motion is also an allowed one.

The combination of C, P and T transformation operators is thought to constitute an exact symmetry of all types of fundamental interactions. The existence of a *CP-symmetry* violation implies a violation of the *T-symmetry*, or the equivalent non conservation of *T-symmetry*, provided that CPT theorem is valid.

Recently, a new generation of experiments, including BaBar Experiment at the Stanford Linear Accelerator Center (SLAC) and the Belle Experiment at the High Energy Accelerator Research Organisation (KEK), Japan, have observed CP violations using B mesons, which confirms the fact that CP violation is not a confined propierty of the kaon physics. This experiments dispelled any doubt that the interactions of the Standard Model violated *CP-symmetry*.

2.3 An explanation to the strong CP-problem

QCD is a description of the strong interactions of quarks and gluons based in a color $SU(3)$ gauge theory and *CP-symmetry* breaking is expected as it involves three generations of quarks that have a *CP-violating* complex phase θ.

The known phenomena called strong *CP-problem*, is the non observation of *CP-symmetry* breaking in the quantum chromodynamics field theory.

A possible solution to the invariance of CP in QCD is given by the Peccei-Quinn mechanism [1].

In the standard model, quarks acquire their mass by means of a Yukawa coupling to a scalar field. This field, that has a nonzero vacuum expectation value, is called the Higgs. Peccei-Quinn proposal to explain CP invariance as a natural consequence of quantum chromodynamics introduces a new scalar field (Higgs doblet) to the Standard model.

2.3.1 The electric dipole moment of the neutron

The selection of the QCD vacuum from an infinity of equivalent choices [2], allows the reinterpretation of θ as an additive term to the usual quantum chromodynamics Lagrangian:

$$\mathcal{L}_{QCD} = \mathcal{L} + i \cdot \mathcal{L}_{\theta}. \tag{2.8}$$

A scalar potential dependent on θ must be applied, but there will be particular choices of phases for which the various scalar vacuum expectation values minimize the potential:

$$|\theta\rangle = \sum_{n=-\infty}^{n=+\infty} e^{-in\theta}|n\rangle. \tag{2.9}$$

The θ dependent term of the QCD Lagrangian can be written as

$$\mathcal{L}_{\theta} = \theta \frac{g^2}{32\pi^2} G_{\theta}^{\mu\nu} \widetilde{G}_{\theta\mu\nu} \tag{2.10}$$

and, according with *equation 2.9*, the vacuum expectation of θ is zero. However, experimental results on the neutron electric dipole moment [57,58] bound the θ vacuum expectation to be $\simeq 10^{-10}$, which is compatible with zero:

$$\begin{gathered} |d_n| < 12 \times 10^{-26}\,\mathrm{e}\cdot\mathrm{cm} \\ d_n \simeq \theta \cdot e \cdot \frac{m_q}{M_N^2} = \theta \cdot 5 \times 10^{-16}\,\mathrm{e}\cdot\mathrm{cm}. \end{gathered} \tag{2.11}$$

2.3.2 The $U(1)_{PQ}$ symmetry. An axion interpretation

To explain the strong *CP-conservation* of QCD [5,6], Peccei-Quinn mechanism interprets the θ-term of the QCD Lagrangian *(equation 2.10)* as an scalar field that later on will be called the "axion" field.

The chiral anomaly of the $U(1)_{PQ}$ symmetry is then implemented at the level of an effective Lagrangian with the introduction of a term linear in the axion field coupled to the anomaly (which is proportional to $G_a^{\mu\nu}\widetilde{G}_{a\mu\nu}$).

In terms of the new scalar field, the Lagrangian term of QCD can be written as

$$\mathcal{L}_\theta \equiv \mathcal{L}_a = \frac{a}{f_a}\xi\frac{g^2}{32\pi^2}G_a^{\mu\nu}\widetilde{G}_{a\mu\nu}. \tag{2.12}$$

This Lagrangian term violates P and T *symmetries*, but conserves *C-symmetry*, which allows then the Global quantum chromodynamics Lagrangian to violate *CP*-symmetry. Feature expected from the three generations of quarks that compose it.

The scalar field of the axion is then a potential with minimum founded to be at

$$< a >= -\frac{f_a}{\xi}\,\theta_{total}, \tag{2.13}$$

being the constant f_a the so-called Peccei-Quinn scale. The expected value of the axion that minimizes the potential is given by *equation 2.13* while its field is invariant against transformations of the type $a \rightarrow a + 2\pi f_a$ since the axion field is a phase $\phi = [(f_a + \rho)/\sqrt{2}] \cdot e^{ia/f_a}$.

An expansion of such effective potential at minimum gives a mass to the axion:

$$m_a^2 =< \frac{\partial^2 V_{eff}}{\partial a^2} >= -\frac{\xi}{f_a}\frac{g^2}{32\pi^2}\frac{\partial}{\partial a} < G_a^{\mu\nu}\widetilde{G}_{a\mu\nu} >_{<a>} \tag{2.14}$$

and considers the "axion" as a particle that is candidate to explain the strong *CP*-problem.

Chapter 3

The axion dynamics

The spontaneous breakdown of the chiral $U(1)_{PQ}$ implies the appearance of a new particle. The "*axion*" [3, 4], a very light pseudoscalar Goldstone boson.

3.1 Axion models

Axions can be seen as generically mixing with pions so that their mass and their couplings to photons and nucleons are proportional to those of π^o by the factor f_π/f_a. However, the specific Peccei-Quinn mechanism implementation leads to different axion models.

The distinguishing feature between the two major axion model classes is the size of the Peccei-Quinn scale f_a, which is inversely proportional to the axion mass m_a.

3.1.1 The "Visible" Axions: large axion mass

The standard axion model assumes an axion decay constant f_a related to the electroweak constant $f_{weak} \equiv (\sqrt{2}G_F)^{-1/2} \approx 250\,\mathrm{GeV}$. Since by construction the scalar field Φ added to QCD by the Peccei-Quinn symmetry cannot be the standard Higgs field, we must introduce two independent Higgs fields Φ_1 and Φ_2 with expectation vacuum values $f_1/\sqrt{2}$ and $f_2/\sqrt{2}$ such that $f_{weak} = (f_1^2 + f_2^2)^{1/2}$ and, therefore, an axion mass of the order of $m_a \approx 200\,\mathrm{keV}$:

$$f_a = f_{weak}\left[3\left(\frac{f_1}{f_2} + \frac{1}{f_1/f_2}\right)\right] \quad \lesssim 42\,\mathrm{GeV}. \tag{3.1}$$

This kind of axions, known as visible or *PQWW-axions*[1], have been ruled out by numerous experiments as well as astrophysical considerations [19].

3.1.2 The "Invisible" Axions: strong decay constant

Since due to cosmological constraints and experimental results the axion mass cannot be so large *(see Section 3.3.2)*, we should try to get $f_a \gg f_{weak}$. Models of this kind introduce an electroweak singlet Higgs field Φ with a vacuum expectation value of $f_a/\sqrt{2}$ that is not related to the weak scale of interactions f_{weak} anymore.

There are two important models that describe such an interaction, the KSVZ[2]

[1] The *standard axion model* was originally proposed by Peccei, Quinn, Weinberg and Wilczek

[2] Introduced by Kim, Shifman, Vainshtein and Zakharov.

and the DFSZ[3] model. Their main differences are based on the coupling of axions to electrons and they both manage to solve the strong *CP-problem*.

The KSVZ model It is the very first suggested model [20,21] for invisible axions and it considers a exotic heavy quark Q intervining in the interaction of axions with matter. The implications of such a model is that neither quarks or leptons carry the so-called Peccei-Quinn charge, $C_u = C_d = C_s = C_e = 0$, but a heavy quark Q does.

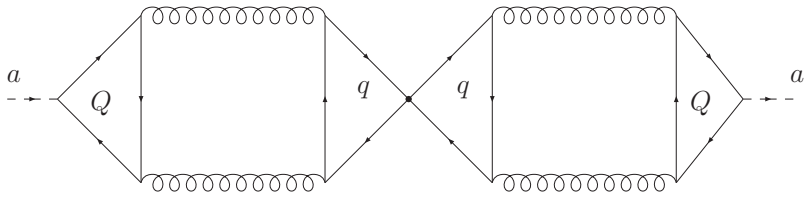

Figure 3.1: *Feynman diagram for axion coupling to an ordinary quark in the KSVZ model via the new quark Q and the gluon (curly lines) loops.*

Following the model independent equation of the axion coupling to nucleons (N),

$$g_{aN} = \frac{C_N m_N}{f_a} = C_N \ 1.56 \times 10^{-7} \ m_{eV} \tag{3.2}$$

and, since Peccei-Quinn charge is not carried by leptons or quarks, we can express the coupling to nucleons of axions belonging to this model as:

$$\begin{aligned} g_{ap}^{KSVZ} &= \tfrac{C_p m_p}{f_a} = -6.01 \times 10^{-8} m_{eV} \\ g_{an}^{KSVZ} &= \tfrac{C_n m_n}{f_a} = -0.69 \times 10^{-8} m_{eV}. \end{aligned} \tag{3.3}$$

[3]Model that was originaly proposed by Dine, Fischler, Srednicki and Zhitnitskiĭ

On the other hand, for axion interaction with photons, the equation

$$g_{a\gamma\gamma} = -\frac{\alpha}{2\pi f_a}\left(\frac{E}{N} - \frac{2}{3}\frac{(4 + m_u/m_d + m_u/m_s)}{(1 + m_u/m_d + m_u/m_s)}\right) \tag{3.4}$$

remains, though different type of KSVZ models suggest different values of E/N either suppresing or enhancing the coupling via the Primakoff effect.

The DFSZ model It is an hybrid between standard and KSVZ models in which an electroweak singlet scalar field Φ with expectation values $f_a/\sqrt{2}$ and two electroweak doublet fields Φ_1 and Φ_2 [22, 23]. In this model, the fundamental fermions are the ones carrying the Peccei-Quinn charge and, therefore, there is no need for exotic quarks like in the KSVZ model.

Being f_1 and f_2 the expectation values of Φ_1 and Φ_2, its branching ratio f_1/f_2 can allow us to define a mixing angle β such that

$$\cos^2\beta = \frac{(f_1/f_2)^2}{(f_1/f_2)^2 + 1}. \tag{3.5}$$

Direct coupling to QCD fermion families is possible in this model. Although the number of fermion families is likely to be *3*, we will refer to them as N_f in a first stage. In the coupling to nucleons, this model follows *equation 3.2* but the value of the nucleon coeficients differ from the ones of KSVZ, being now $C_d = C_s = (cos^2\beta)/N_f$ and $C_u = (sin^2\beta)/N_f$, so that using $N_f = 3$:

$$\begin{aligned} C_n &= -0.18 + 0.39\ cos^2\beta \\ C_p &= -0.10 - 0.45\ cos^2\beta. \end{aligned} \tag{3.6}$$

Introducing this new result in the calculation of the coupling with nucleons for the DFSZ model, we can conclude that the strength of the coupling to nucleons in this model goes like

$$\begin{aligned} g_{ap}^{DFSZ} &= \tfrac{C_p m_p}{f_a} = \left[-0.10 - 0.45\ cos^2\beta\right] \times \tfrac{m_p}{f_a} \\ g_{an}^{DFSZ} &= \tfrac{C_n m_n}{f_a} = \left[-0.18 + 0.39\ cos^2\beta\right] \times \tfrac{m_n}{f_a}. \end{aligned} \tag{3.7}$$

The direct interaction of axions to electrons is also allowed in this models and therefore, since the electrons are able to carry Peccei-Quinn charge $C_e = (cos^2\beta)/N_f$, its coupling can be written as

$$g_{aee}^{DSFZ} \;=\; 0.85 \times 10^{-10} m_{eV}\; \frac{cos^2\beta}{N_f} \;=\; 0.28 \times 10^{-10} m_{eV}\; cos^2\beta. \tag{3.8}$$

On the other hand, interaction with photons is given by

$$g_{a\gamma}^{DSFZ} \simeq -0.75 \frac{\alpha}{2\pi f_a}. \tag{3.9}$$

3.2 Axion couplings

The interaction of axions with fundamental bosons, such gluons and photons, as well as with fermion like, electron and nucleons are described by the Lagrangian term $\mathcal{L}_{int}[\gamma^\mu a/f_a; \psi]$. From this term, we know how the axion couples with mater. Not only the nature of the coupling, but also the strength of it.

3.2.1 Coupling to gluons

The dimensionless Yukawa coupling of the scalar field for the interactions is $g_a = m_f/f_a$, with m_f the mass of the fermion involve in the interaction and f_a the Peccei-Quinn scale.

The chiral anomaly *(see figure 3.2)*, allows an axion coupling to gluons and it is the mechanism for the axions to acquire mass.

The coupling of axions to gluons is the feature that distinguishes the axions from other pseudoscalar particles:

$$\mathcal{L}_{aG} = \alpha_s \frac{1}{8\pi f_a}\; a G_a^{\mu\nu} \widetilde{G}_{a\mu\nu} = \frac{g_s^2}{4\pi} \frac{g_a}{8\pi m_f}\; a G_a^{\mu\nu} \widetilde{G}_{a\mu\nu}. \tag{3.10}$$

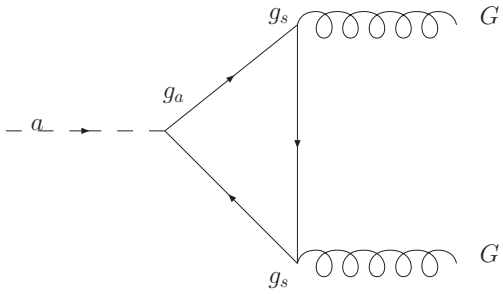

Figure 3.2: *Feynman diagram of the axion-to-gluon coupling, where g_s is the strong coupling constant, while g_a represents the axion-to-fermion copling constant.*

Moreover, since from the mixing of pions we know that the mass $m_\pi = 135\ MeV$ and its deacay constant $f_\pi = 93\ MeV$, we are in conditions to give an approximate value to the axion mass *(see equation 3.11)* by introducing the corresponding quark mass ratios [7]:

$$m_a = \frac{m_\pi f_\pi}{f_a}\left(\frac{m_u/m_d}{(1+m_u/m_d+m_u/m_s)(1+m_u/m_d)}\right)^{1/2}. \tag{3.11}$$

The only attention to take is the fact that the value of the coefficients (m_u/m_d) and (m_u/m_s) in *equation 3.11* variate depending on the specific model [8,9]:

$$m_a \approx\ 0.60\,\mathrm{eV}\frac{10^7\,\mathrm{GeV}}{f_\mathrm{a}}. \tag{3.12}$$

3.2.2 Coupling to photons

The pion coupling of axions opens the possibility of axions coupling with photons via the Primakoff effect [10,12]. An axion can couple to two photons in a triangle loop via the mechanism shown in the *figure 3.3*. The Lagrangian

term for such an interaction can be written as

$$\mathcal{L}_{a\gamma} = -\frac{g_{a\gamma\gamma}}{4} F_{\mu\nu}\widetilde{F}^{\mu\nu}\ a = g_{a\gamma\gamma}\vec{E}\cdot\vec{B}\ a, \tag{3.13}$$

where $g_{a\gamma\gamma}$ is the coupling constant and $F^{\mu\nu}$ the electromagnetic tensor that generates the electromagnetic fields $\vec{E}$ and $\vec{B}$.

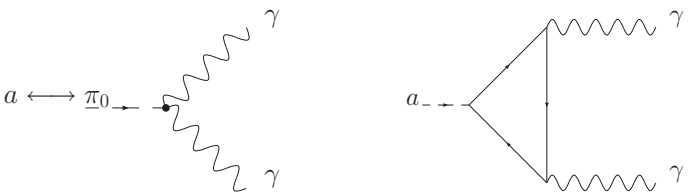

Figure 3.3: *Two Feynman diagrams contributing to the axion-to-photon coupling. On the right the coupling of the axion to photons via a triangle loop through fermions carrying Peccei-Quinn and electric charges. On the left, an axion-to-pion mixing, which produces the generic coupling of axions to photons.*

The coupling constant is given as function of the fine structure constant α and the axion model dependent ratio between the color anomaly N of the axion current and the electromagnetic anomaly E:

$$g_{a\gamma\gamma} = -\frac{\alpha}{2\pi f_a}\left(\frac{E}{N} - \frac{2}{3}\frac{(4 + m_u/m_d + m_u/m_s)}{(1 + m_u/m_d + m_u/m_s)}\right). \tag{3.14}$$

The coeficients E and N are defined in terms of the electric and Peccei-Quinn charges carried by fermions. For fermions carrying both types of charges (Q_j and X_j) $E \equiv 2\sum_j X_j Q_j^2 D_j$, where $D_j = 3$ for quarks and $D_j = 1$ for leptons, and $N \equiv \sum_j X_j$, where the sum is over all fermions carrying Peccei-Quinn charge X_j.

Such a coupling allows a model independet axion decay of the kind $a \to \gamma\gamma$ via Primakoff effect in the presence of electromagnetic fields.

3.2.3 Interaction of axions with fermions

One of the processes for stelar emission of weakly interacting particles from the hot dense interior is the Compton process. Non negligible efects to the stelar flux of such particles can be due to axions. Compton scattering of axions are analogous to the usual Compton scattering of photons with the difference that now one of the photons of the interaction has became an axion. The mechanism that allows such exchange is shown in *figure 3.4 and 3.5.*

$$\mathcal{L}_{af} = \frac{g_{af}}{2m_f}\ \bar{\psi}_f \gamma^\mu \gamma_5 \psi_f \partial_\mu a \tag{3.15}$$

is the Lagrangian expression for the coupling, where ψ_f denotes the fermion. In that case, being m_f the mass of the fermion and C_f the effective Peccei-Quinn charge, the coupling g_{af} can be written as

$$g_{af} = \frac{C_f m_f}{f_a}. \tag{3.16}$$

Like that, if quarks and electrons do carry Peccei-Quinn charge, these couplings can be observed.

Coupling to electrons If electrons do carry Peccei-Quinn charge, as they do in the DFSZ models *(see Section 3.1)*, there will be a tree-level coupling with axions in the Lagrangian of *equation 3.15.*

There also exists radiatively induced coupling of axion to electrons at the one-loop level with a coupling g_{aee}^{rad}, which is more complicated and smaller than the g_{aee}^{tree} coupling. An interaction of this kind, leads to a smaller contribution to the Lagrangian if we compare it to the tree level one *(see figures 3.4 and 3.5)*.

The coupling g_{af} for the electron is then written like

$$g_{aee}^{tree} = \frac{C_e m_e}{f_a} = C_e\ 0.85 \times 10^{-10}\ m_{eV}, \tag{3.17}$$

where m_{eV} is the axion mass given in electronvolts and C_e depends on the effective Peccei-Quinn charge of the electron $C_e = X'_e/N$.

On the other hand, for models like KSVZ *(see Section 3.1)*, $X'_e = 0$.

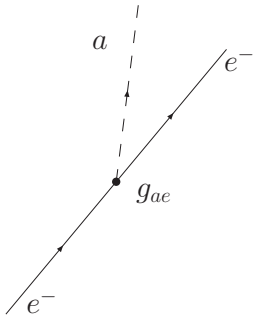

Figure 3.4: *Direct axion-to-electron interaction, only possible depending on the axion model (only possible for DFSZ axions) which can then be used to distinguish these axions from the hadronic or KSVZ axions.*

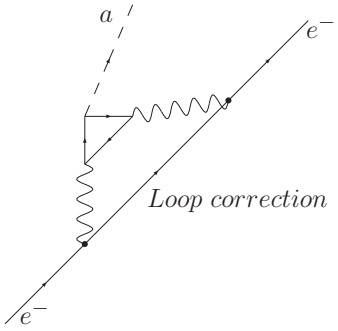

Figure 3.5: *A higher order coupling of axion-to-electron, mechanism used by hadronic axions to interact (KSVZ model).*

Coupling to nucleons It is known that axion models differ in their assignment of Peccei-Quinn charges to the axion, but not on the value of the coeficient N.

Independently of the axion models, an axion-to-nucleon coupling transforms the constant g_{af} of *equation (3.16)* into *equation (3.2)*. Being C_N different for proton and neutron.

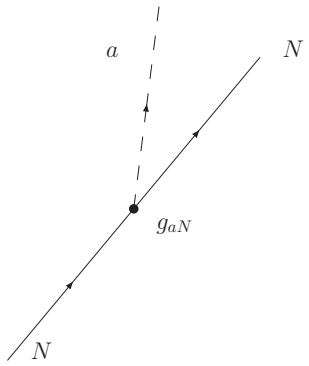

Figure 3.6: *Feynman diagram of axion-to-nucleon coupling.*

We can find then a model independent general expresion for the Peccei-Quinn charges of protons and neutrons:

$$\begin{aligned} C_p &= (C_u - \eta)\Delta u + (C_d - \eta\ m_u/m_d)\Delta d + (C_s - \eta\ m_u/m_s)\Delta s \\ C_n &= (C_u - \eta)\Delta d + (C_d - \eta\ m_u/m_d)\Delta u + (C_s - \eta\ m_u/m_s)\Delta s. \end{aligned} \tag{3.18}$$

In the equation above, $\eta = (1 + m_u/m_d + m_u/m_s)^{-1}$, while $\Delta q_{u,d,s}$ is the helicity contribution of the nucleon carried by the quarks [11],

$$\Delta u = +0.85 \pm 0.03, \qquad \Delta d = -0.41 \pm 0.03, \qquad \Delta s = -0.08 \pm 0.03. \tag{3.19}$$

By introducing the corresponding axion masses in the *equation 3.18*, we could obtain the Peccei-Queen charges carried by the nucleons, but we should not forget that the PQ charge carried by the quarks is model dependent *(see Section 3.1)*.

3.3 Theoretical limits on the axion masses and its couplings

Astrophysics and cosmology provides a natural laboratory for elementary particle physics. Solutions to phenomena such as the strong *CP-problem* can be crosschecked in the "outer space". Axion existence in the early universe may have affected the big-bang cosmology.

The implications of axions in the development of the universe depend on the different scenarios for which axions would have coexisted in the early universe. As a matter of fact, axions could have been in thermal equilibrium for those temperatures $T_U \gg f_a$. Moreover, once the temperature is satisfying $f_a \gg T_U$, the axion could have decoupled and behave as a free massless scalar field.

The value of f_a is then a really important parameter. Unfortunately, the Peccei-Quinn mechanism allows any value of f_a to solve the strong *CP-problem* and many scenarios can be considered.

There are different mechanisms to generate relic axions, but it is not determined which one of them dominates, since it depends on both, the axion mass and whether or not inflaction took place:

- Thermal production [15] : if axions were strongly interacting, $f_a \lesssim 10^8$ GeV, they would have thermalized before the QCD phase and therefore there would be a sea of "invisible" axions.
- Missalingment affecting the early universe [16, 17]: it could have excited coherent oscillations of the axion field in the early universe. When the temperature of the universe drops below f_a, axions could have acquired mass and become a part of the cold dark matter.

3.3.1 Astrophysical limits

Despite their small interaction with normal matter, axions have a considerable influence on the evolution of stars. Axions could be produced in the interior of stars by different processes and, hence, provide an additional loss of energy. As a consequence, the star will contract and increase its luminosity as well as its central temperature in order to adjust to the new situation. This will lead to a shortening of the star's lifetime due to a faster consumption of fuel. It is possible to put limits on the coupling of axions to photons, electrons and nucleons by demanding that time scales of stelar evolution must match with observational limits.

The best limits on axion-to-photon coupling can be obtained from low mass stars with a helium burning core. The stars on the Horizontal branch (HB) have reached helium burning and therefore they generate energy by fusing helium to carbon and oxygen. A Primakoff energy loss rate would accelerate the consumption of helium and thus reduce the Horizontal Branch lifetime [47].

By observing the ratio between the number of HB referred to the low-mass red giants in globular clusters for which axion emission is suppresed since $\gamma + Ze \rightarrow Ze + a$ is not dominant , we can obtain the coupling constant $g_{a\gamma} \lesssim 10^{-10}\,\mathrm{GeV}^{-1}$. This horizontal branch limit, which is also referred to as globular cluster limit, might however vary due to the uncertainties of its determination.

Helium ignition could also be delayed due to axion cooling and, therefore, the core of these stars would grow more massively before the helium ignites. As a consequence, an evolution of RGB[4] stars to brighter stars could occur. Last studies, however, agree that the core mass at helium ignitium agrees with theoretical expectations within $5 - 10\%$ [10]. Since the Primakoff loss rate is suppressed in the degenerated red-giant cores, for bremsstrahlung $e + Ze \rightarrow Ze + e + a$ applied to the red-giant core conditions [48], it can be obtained that $g_{aee} \lesssim 3 \times 10^{-13}\,\mathrm{GeV}^{-1}$.

A rather strict constrain on the axion-to-nucleon coupling can be derived from observing he measured neutrino signal from the supernova SN 1987A [10]. From the duration of this supernova it is possible to place a limit. Neutrinos

[4] Red Giant Branch stars.

are trapped inside the hot and dense core after the collapse and, its escape is only possible by diffusion, while axion emission would carry away energy from the interior. If axions interact too strongly, they are trapped in the *SN* core. Also, they cannot be excluded by the *SN* signal if their mass is larger than $m_a \gtrsim 10^{-2}\,\mathrm{eV}$.

3.3.2 Cosmological limits

In most axion models, Peccei-Quinn symmetry breaking occurs when the complex scalar field develops the vacuum expectation value $f_a/\sqrt{2}$. For this to happen, the Universe temperature T_U has to cool down to the Peccei-Quinn scale f_a. In this stage, the effective potential develops its expectation vacuum value, but still has rotational symmetry and thus, the value of $\bar{\Theta}$ is not yet fixed and the axion appears as this massless degree of freedom $\bar{\Theta}$.

String Scenario One consequence of the $U(1)_{PQ}$ symmetry breaking is the appearance of axion strings as topological defects [13, 49]. The contribution to the density of axions today Ω_a coming from the string decay, depends on when the inflaction took place.

In the case of axions interacting strongly enough, let's say $f_a \lesssim 10^8\,\mathrm{GeV}$, a thermal equilibrium state would have been reached in the early universe before the quantum chromodynamics phase transition ocurred. At this point, each string would have become the boundary of a domain wall, which eventually would have decayed, contributing like that to the axion density.

In order to performe the calculation of the axion density due to string emission, the radiated axion spectrum has to be estimated. With the help of computer simulations [14], it has been found that the dominant source of axion radiation are string loops rather than the long strings, and that the axion radiation is strongly peaked at wavelegths of the order of the loop size. The loop contribution to the cosmic axion density is:

$$\Omega_{strings} h^2 \simeq 88 \times 3^{\pm 1}[(1+\alpha/\kappa)^{3/2} - 1]\Big(\frac{1\,\mu\mathrm{eV}}{m_a}\Big)^{1.175}. \qquad (3.20)$$

Here, $\Omega_{strings}$ is the ratio of the axion density ρ_a to the critical density for closing the universe ρ_{crit}, h is the Hubble constant in units of $100\,\mathrm{km\,s^{-1}\,Mpc^{-1}}$,

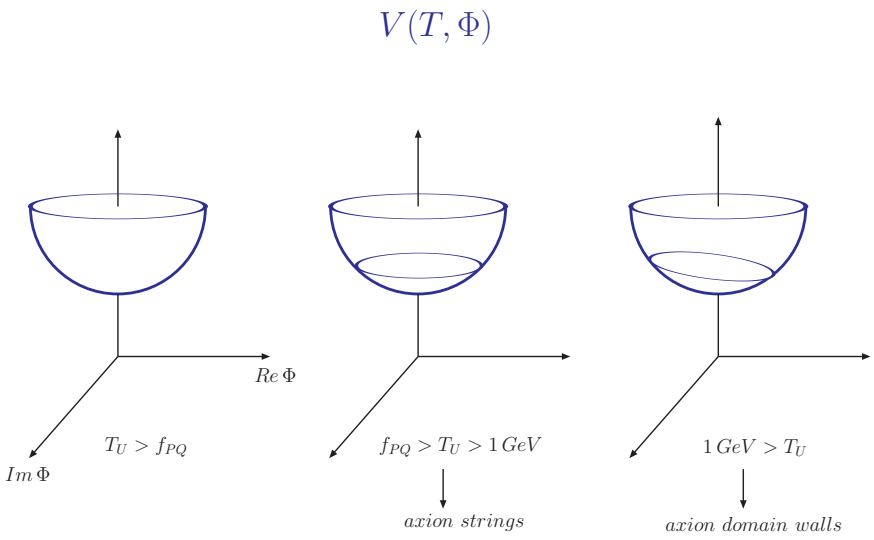

Figure 3.7: *Evolution of the effective axion potential as a function of the temperature T_U of the universe.*

and the stated range reflects the recognised uncertainties of the cosmic conditions at the QCD phase transition and of the temperature dependent axion mass. The values α and κ are not known, but most probably, their ratio is within the range $0.10 < \alpha/\kappa < 1.0$, which would make the expression in squared brackets to become $0.15 - 1.83$, fact that allows Sikivie *et al.* to find that the motion of global strings is strongly damped, which leads to a flat axion spectrum:

$$\Omega_{strings}h^2 \simeq 1.9 \times 3^{\pm 1}\Big(\frac{1\,\mu\text{eV}}{m_a}\Big)^{1.175}. \tag{3.21}$$

Vacuum misalignment Still, the misalignment mechanism [15–17], could be able to excite coherent oscillations of the axion field until the temperature of the early universe approaches the QCD scale Λ_{QCD}. At $T_U > \Lambda_{QCD}$ all the values of $\bar{\Theta}$ were equally probable, but, once the axion mass turns on, the

axion field begins to roll towards its nowadays value $\bar{\Theta} = 0$. The axion field oscillations do not dissipate in other forms of energy and hence, contribute to the energy density today. The density of axions produced by the vacuum realignment mechanism is proportional to the initial realignment angle $\bar{\Theta}_i$ where the axion field was sitting for $T > \Lambda_{QCD}$

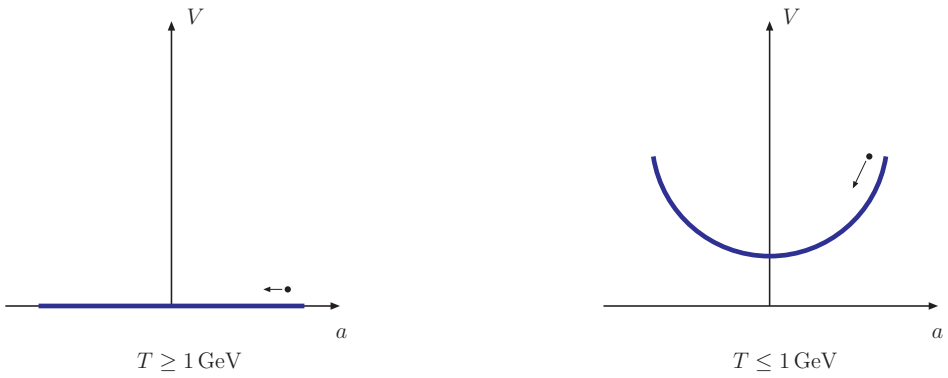

Figure 3.8: *Turn on of the axion effective potential at $T_U \simeq 1\,\mathrm{GeV}$ and the initial value of $\bar{\Theta}$ at this moment.*

Again, the contribution to the total axion densty today in the Universe through this mechanism depends on the inflation ocurring before or after the Peccei-Quinn symmetry breaking. In the first case, the value of $\bar{\Theta}_i$ is uniformly distributed. Therefore, inflation could have also suppressed this axion production mechanism. We could express the contribution to the cosmic critical density due to vacuum misalignment as

$$\Omega_{mis}h^2 \simeq 1.9 \times 3^{\pm 1}\Big(\frac{1\,\mu\mathrm{eV}}{m_a}\Big)^{1.175}\bar{\Theta}_i^2 F(\bar{\Theta}_i), \tag{3.22}$$

where the function $F(\bar{\Theta})$ accounts for anharmonic corrections to the axion potential. In order to avoid fine tunning of the initial misalignment conditions $\bar{\Theta}_i^2 F(\bar{\Theta}_i) \sim 1$, in which case, we have that the contribution to the axion density is of the same order as the given by the axion strings *(equation 3.21)*

Thermal production Since the axion coupling to matter happen to be proportional to $(f_a)^{-1}$, if f_a is sufficiently small so that the axion can interact sufficiently strongly, they will thermalize in the early universe. We could say that when the reaction rate R for a given process that creates and destroy a particle specie occurs rapidly compared to the expansion rate of the universe H, this particle specie will be in thermal equilibrium. There is a time interval in the early universe, which depends on the main axion processes considered for the calculation of R, where these condition is fulfilled and axions are in good thermal contact with the universal plasma. Then, when the condition $R \gtrsim H$ is not satisfied anymore, thermal axion decouple while they are still very relativistic, and survive until today as thermal relics.

Thermal production of axions [15] could happen for $f_a \lesssim 10^8\,\mathrm{GeV}$ considering that the main axion creation and destruction reactions would be the Primakoff process $\gamma + q \to a + q$ and $\gamma + Q \to a + Q$. Recent reviews on the matter have considered different thermalizing processes. Independently of the models, at a present day the axion density of thermal axions is found to be of the order of 1 to $100\,\mathrm{cm}^{-3}$, with the caracteristic that

$$\Omega_{thermal} h^2 \propto m_a, \tag{3.23}$$

which differs with

$$\Omega_{string,miss} h^2 \propto (m_a)^{-1}. \tag{3.24}$$

By taking into account all the constraints, there is not but a little window from μeV to some meV for which the existence of hadronic axions is allowed. Nevertheless, experiments also searched the prohibited regions, because neither astrophysical nor cosmological considerations are absolutely stringent *(see figure 3.9)*.

3.3.3 Axions as a Dark Matter candidate

Several facts, such as galactic rotational curves or the cosmic microwave background anisotropies, hint the fact that most of the matter density of the universe today is composed of a non-luminous and non-absorbing component,

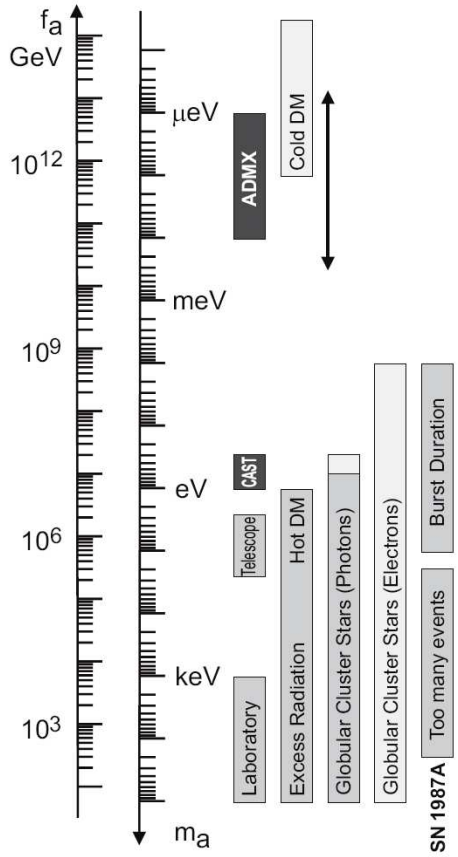

Figure 3.9: *Astrophysical and cosmological exclusion regions for the axion mass m_a and, equivalently, the Peccei-Quinn scale f_a. Since the globular-cluster limit is derived from axion-to-photon coupling, it is a model dependent estimation.* GUT *or* DFSZ *models with $E/N = 8/3$ were used here. The limit from the SN 1987A depends on the axion-to-nucleon coupling and thus, what is shown here is exact for KSVZ and approximately for DFSZ axions. The dotten regions indicate where axions could form the cosmic dark matter. Some experiments searching for galactic dark matter axions are also included. Figure taken from [47].*

called Dark Matter [18]. Its determining propierty is that it does not emit any electromagnetic radiation, and therefore, can be only inferred by its gravitational effects. Two possibilities exist for the nature of the Dark Matter: either it is like the conventional matter, i.e, made of atoms (baryonic Dark Matter) or single particles. However, its nature has not been yet proven.

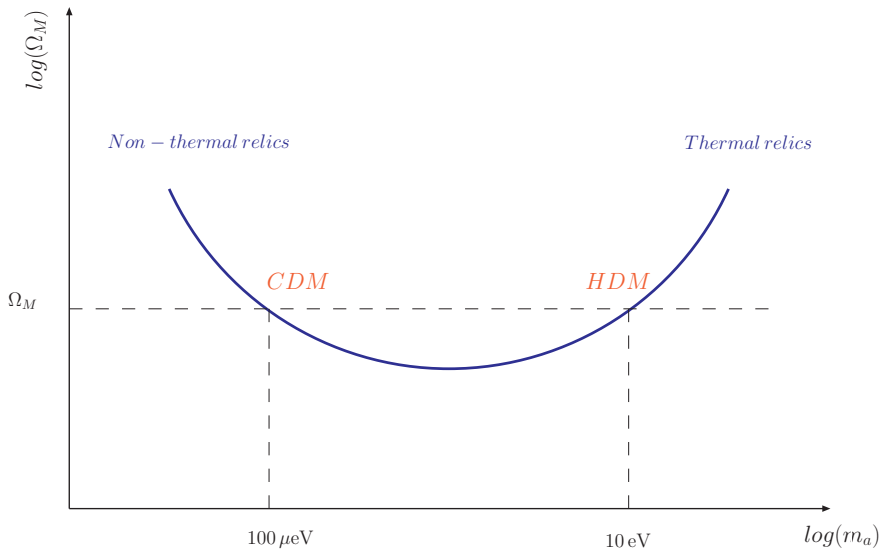

Figure 3.10: *Lee-Weinberg curve for axions, where their density contribution to the Dark Matter is shown as a function of the axion mass.*

The non-baryonic Dark Matter is usually divided in two groups: hot dark matter (HDM)[5] and cold dark matter (CDM)[6]. Axions are bosons and therefore could be a non-baryonic candidate for dark matter. In principle, an axion could account for both, HDM and CDM, depending on their mass. If f_a is so large (small mass), that they never reached the thermal equilibrium, the thermal production is suppressed and then the misalignment mechanism will take over. As axions are not relativistic from the moment of their first appearance at 1 GeV temperature, they might be an important component of the CDM.

[5] Relativistic
[6] Non-relativistic

If, on the other hand, the Peccei-Quinn scale is small enough for the axion to thermalize in the early universe, a relativistic axion density would exist today, which could contribute to the HDM component *(see figure 3.10)*. In this case, the density of axions is proportional to the axion mass, which will be of the order of the eV since we are dealing with thermic axions.

3.4 Axion detection

Since the stelar evolution excludes a possible scenario in which "visible" axions could be possible *(see 3.3.2)*, Pierre Sikivie [24] proposal to look for "invisible" axions coming from stars became of most interest. Axions should be able to leave traces in detectors as mono-energetic photons produced via the Primakoff effect that such a particle could suffer in the presence of a magnetic field.

Since the axion-to-photon coupling is a consequence of the Peccei-Quinn interactions between axion and gluons, it can be found in all the axion models mentioned in *Section 3.1*. This property can be used by the experiments in order to detect the hypothetical particle. Experiments in which an axion or an axion-like particle couples to a photon have become of maximum interest.

- Solar axions: Helioscopes.
- Galactic axions: Haloscope and Telescope Searches.
- Laboratory axions: Laser experiments.

3.4.1 Helioscopes

Search for axions can be performed by looking into the stars. Axion emission by hot and dense plasma of the stars could generate a flux of such particles arriving to the Earth. Helioscopes look into the Sun and, by the use of electromagnetic fields, try to provoke an axion-to-photon conversion via the Primakoff effect to detect them.

Since the Primakoff effect can be produced due to electric or magnetic fields,

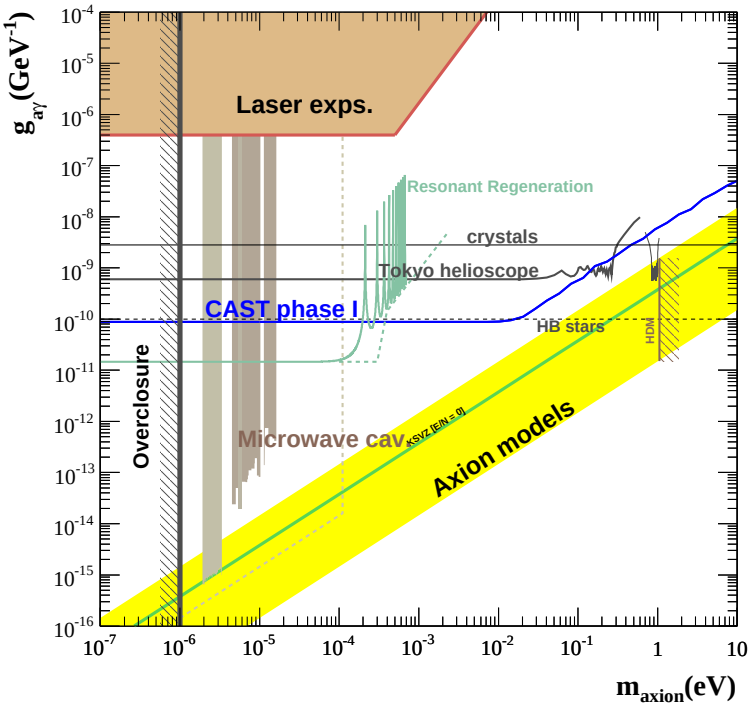

Figure 3.11: *Axion to photon coupling constant plotted versus the axion mass for the different kind of experiments looking for axions. The astrophysical limit for the horizontal branch stars (HB) is added as well. This exclusion plot is valid for any axion-like particle, except if haloscope are used, since these searches assume that the particles are galactic dark matter.*

we can divide the Helioscope search in two areas: the magnet searches and the crystal searches.

Magnet searches A first type of "axion helioscopes" applies a transverse magnetic field to convert the incoming axions into photons. The first experiment to use this technique was performed by Lazarus et al. [35] obtaining a coupling axion-to-photon $g_{a\gamma\gamma} \lesssim 3.6 \times 10^{-9}\,\mathrm{GeV}^{-1}$ for axion masses below

0.03 eV and $g_{a\gamma\gamma} \lesssim 7.7 \times 10^{-9}\,\mathrm{GeV}^{-1}$ for axion masses in the region between 0.03 and 0.11 eV.

Following this experiment, the Tokyo Axion Helioscope continued the search using the same method, but providing better sensitivity, and thus leading to a more restrictive limit $g_{a\gamma\gamma} \lesssim 6.0 \times 10^{-10}\,\mathrm{GeV}^{-1}$ for $m_a \lesssim 0.03\,\mathrm{eV}$.

At the present time, the CERN Axion Solar Telescope[7] [45, 68], which will be described in more detail in *Chapter 5*, is looking for axions using the same basic principle, but with a considerably increased sensitivity:

$$g_{a\gamma\gamma} \lesssim 8.8 \times 10^{-11}\,\mathrm{GeV}^{-1}\ (95\%\ \mathrm{CL})\ \text{for}\ m_{\mathrm{a}} \lesssim 0.02\,\mathrm{eV}. \tag{3.25}$$

Crystal Searches Electric fields can be provided by crystalline detectors. The axion-to-photon conversion is coherent if the Bragg condition is fulfilled [29,30]. Three experiments were looking for this characteristic Bragg patterns:

- The SOLAX[8] [31] experiment used a Germanium Spectrometer giving a bound for axion masses up to 1 keV of $g_{a\gamma\gamma} \lesssim 2.7 \times 10^{-9}\,\mathrm{GeV}^{-1}$
- The COSME[9] [32] detector at the Canfranc Underground Laboratory accomplished to reach a mass independent result that depends on the solar model $g_{a\gamma\gamma} \lesssim 2.78 \times 10^{-9}\,\mathrm{GeV}^{-1}$.
- The DAMA[10] [33] experiment on its part used NaI(Tl) crystals and achieved a limit of $g_{a\gamma\gamma} \lesssim 1.7 \times 10^{-9}\,\mathrm{GeV}^{-1}$ in the eV range.

However, the approach to detect solar axions with the help of an electric field turned out to be limited [34], because neither present nor future crystal detector experiments will be able to achive the limit set by globular clusters.

3.4.2 Haloscope and Telescope searches

Haloscopes Microwave cavity experiments look for galactic halo axions, activity from which they inherit their name. Axions whose mass is of the order

[7] CAST
[8] SOlar AXion search in Argentina
[9] Germanium detector
[10] Particle DArk MAtter searches with highly radiopure scintillators at Gran Sasso.

of μeV trapped in the galactic halo may converte into photons in the presence of a magnetic field. The two first experiments of this kind were held in the Rochester-Brookhaven-Fermilab and the University of Florida. Since only those axions sensing a transverse magnetic field may transform, the allowed axion masse range was found to be between $4.5\,\mu$eV and $16.3\,\mu$eV.

Follow-up experimets are showing higher sensitivity. Similar setups with improved technologies allow the Axion Dark Matter eXperiment at the Lawrence Livermore National Laboratory to restrict the relic axion masse into a bound between $1.9\,\mu$eV and $3.3\,\mu$eV.

A different approach, as set up in Kyoto, Japan with CARRACK[11] is investigating the mass ranges included in the bound of $2\,\mu$eV to $50\,\mu$eV.

Telescopes Thermally produced axions, can be searched for with telescopes. The most likely places to find such axions are cluster of galaxies, places in which the axions would produce an emission line once they decay. The radio telescope at the Haystack Observatory was able to rule out coupling constants of $g_{a\gamma\gamma} \lesssim 1.0 \times 10^{-9}\,\mathrm{GeV}^{-1}$ for axion masses in the range of $298\,\mu$eV to $363\,\mu$eV [26].

3.4.3 Laser experiments

"Shining light through walls" experiments In "Shining Light through Walls" or beam dump experiments, a strong laser beam is sent through a magnetic field in which a part of the photons will be converted into axions.

Then, a wall or shield blocks the photons, while the feebly interacting axions can pass through to the other side, where they are reconverted into photons by another magnetic field, and therefore detected [36,37].

This procedure is described by *figure 3.12*. Instead of the beam lines, resonating cavities can be used on either side as well [38]. Results from such an experiment have yielded an upper boundary for $m_a \lesssim 10^{-3}\,\mathrm{eV}$ [39]:

[11] Cosmic Axion Research using Rydberg Atoms in a resonant Cavity in Kyoto

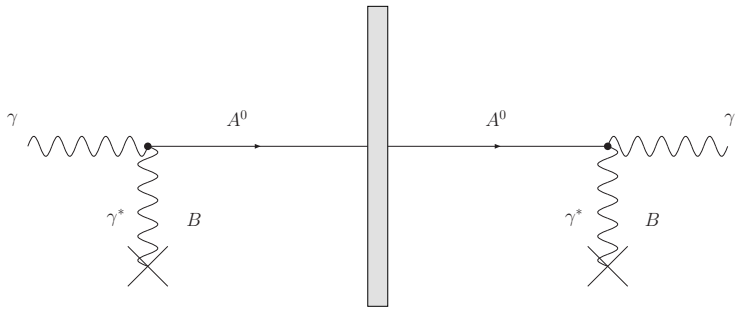

Figure 3.12: *Basic principle of a "Shining Light through Walls" experiment. An incoming photon beam is partly converted into axions. A wall keeps the remaining photons from getting to the other side, while the axions pass the shield. Beyond the barrier, the axions can be reconverted into photons by the use of another magnetic field.*

$$g_{a\gamma\gamma} \lesssim 7.7 \times 10^{-7}\,\mathrm{GeV}^{-1}. \tag{3.26}$$

Polarization experiments This experiments make use of an incident laser beam composed of coherent photons going into a region in which a magnetic field is applied.

An axion-to-photon coupling of the beam in the magnetic region, would introduce linear birrefringence *(phase factor)* and linear dichroism *(rotation)* to the incoming polarization plane of the beam.

First results of this kind [25] have given an axion-to-photon coupling of $g_{a\gamma\gamma} \lesssim 2.5 \times 10^{-6}\,\mathrm{GeV}^{-1}$ for axion masses below $700\,\mu\mathrm{eV}$.

A more recent experiment, PVLAS[12] [27], observed a strong coupling effect

[12]Polarizzazione del Vuoto con Laser

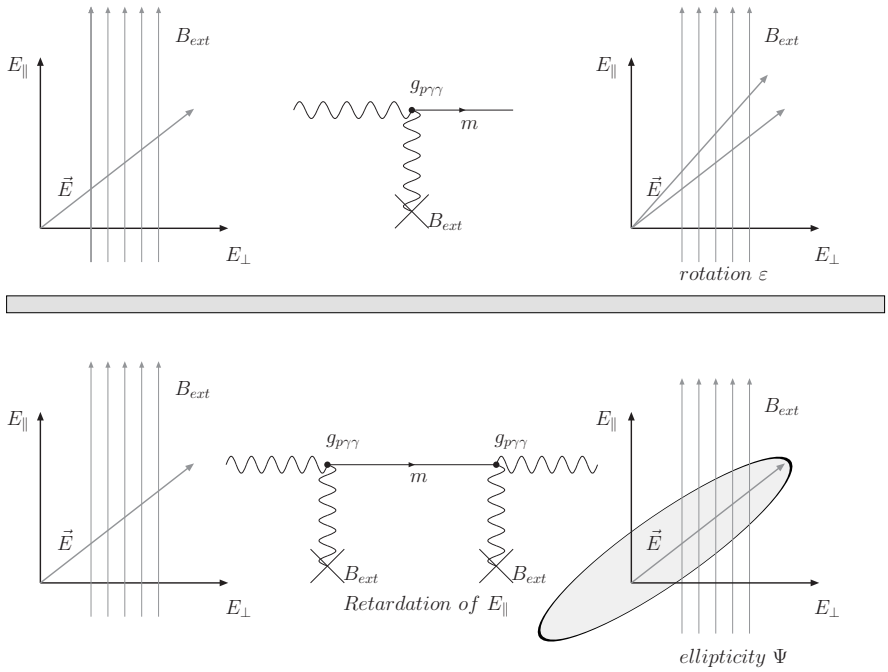

Figure 3.13: *The priciple of the formation of Dichroism, a rotation of the polarization plane induced by the creation of massive particle coupling to two photons it is shown in the upper image, while the lower one shows the principle of development of Ellipticity induced by the retardation of an electric field compontent relative to the oder when a massive particle is produced.*

corresponding to an axion-like particle of around $3.6 \times 10^{-6}\,\mathrm{GeV}^{-1}$. However, the analysis of the systematics of the experiment have ruled out the preliminary result.

Nevertheless, there have been attempts to find a new model of particle physics in which PVLAS signal would fit. A recent paper by E. Massó and J. Redondo [28] suggests that both results could be accommodated in models were axion-like particles suffer a strong interaction that traps them in the stellar plasma, or models where the axion-photon vertex could be suppressed in the solar core.

Several experiments are already searching for axion-like particles. OSQAR for example makes use of a long LHC magnet of 15 m and $B \simeq 9$ Tesla and it is presently running at CERN [40, 41]. Other experiments like LIPPS [42] are looking for a possible signal of axion-like particles coupling to photons but so far no evidence has been found. ALPS is also looking for axion-like signatures in the X-Ray laser facility of DESY [43].

Chapter 4

The Solar axion

The axion arise so weakly interacting that was called “invisible”. Fortunately, Pierre Sikivie [24] proposed some experimental test to address the question of the existence of the “invisible” axions.

4.1 The Primakoff conversion

The two photon decay mode of the π^0 meson involves the explicit breaking of a classical symmetry due to quantum fluctuations of the quark fields coupling to a gauge field. This phenomenon, called anomalous symmetry breaking is of pure quantum mechanical origin, and in this case involves the coupling of quarks to photons.

Independently to the mechanism of the two-photon decay, its existence implies an interaction between the π^0 wave function and the electromagnetic wave field [12]:

$$\text{Interaction Energy density } = \eta \left(\frac{\hbar}{\mu c}\right) \frac{1}{\sqrt{\hbar c}} \varphi \, \mathbf{E} \cdot \mathbf{H}. \tag{4.1}$$

The factors $\hbar/\mu c$ and $1/\sqrt{\hbar c}$ are introduced for dimensional reasons, being μ the rest mass of π^0, η a dimensionless constant determinated by the decay mechanism and φ the pseudoscalar field of the pion.

In the context of quantum chromodynamics, the coupling of two-photons producing π^0 is not but the confirmation of a decay channel of pseudoscalar particles into two-photons.

Since the Peccei-Quinn solution to the strong *CP-problem* of QCD involves a new pseudoscalar particle, a two-photon decay channel is expected for the axion, as it happens to π^0 *(See figure 4.1)*.

To make the axion "visible", we will make use of its coupling to the electromagnetic fields and the fact that in the Earth we are able to provide static electric or magnetic fields.

4.2 The production of axions in the Solar core

Blackbody photons in the solar core could be converted in axions due to the fluctuating electric fields of the charged particles in the hot plasma.

Following Sikivie's proposal [24], we will first describe the process of production of axions in the presence of electrons and nuclei in the dense plasma of

Figure 4.1: *Feynman diagram for the Primakoff production of axions by the interaction with a virtual photon. On the left, the diagram for the Primakoff effect that a photon suffers in the electric fields produced by a nucleous or a certain density of electrons in the solar core. The right diagram represents the Feynman diagram for the interaction of an axion converting to a photon via virtual photon in the presence of magnetic fields.*

the solar core. According to the left Feynman diagram shown in the *figure 4.1*,

$$\gamma + (e^-, Ze) \rightarrow (e^-, Ze) + a. \tag{4.2}$$

In the solar core, a charge distribution $\rho(\vec{r})$ is able to provide an external electric field $\vec{E}(\vec{r})$ in which a photon whith energy $\omega = kc$ could convert into an axion. The diferential cross section of the process is found to be

$$\frac{d\sigma_a}{d\Omega} = \frac{1}{2}\frac{g_{a\gamma\gamma}}{4\pi}\left[\frac{e}{m_e}\right]^2 \frac{|\vec{k}\times\vec{p}_a|^2}{|\vec{q}|^4}\cdot|F(\vec{q})|^2, \tag{4.3}$$

where the momentum transfer to the axion in the Primakoff conversion that the blackbody photons suffer is represented as $\vec{q} = \vec{k} - \vec{p}_a$. The momentum of the initial photon is represented by $\vec{k}$ while the momentum of the outcoming axion is $\vec{p_a}$. A factor $\frac{1}{2}$ averages over photon polarizations. Also, the charge distribution in the solar plasma is defined by the form factor

$$F(\vec{q}) = \frac{1}{e}\int d^3\vec{r}\rho(\vec{r})e^{i\vec{q}\cdot\vec{r}}. \tag{4.4}$$

If the plasma frecuency and the axion mass are assumed to be small in comparison to the energy of the photon that suffers the Primakoff effect, we are

able to express the cross section as

$$\frac{d\sigma_a}{d\Omega} = \frac{1}{2}\frac{g_{a\gamma\gamma}}{4\pi}\left[\frac{e}{m_e}\right]^2 \frac{\sin^2\theta}{\left[2(1-\cos\theta)+(q_0/\omega)^2\cos\theta\right]^2}\cdot|F(\vec{q})|^2. \tag{4.5}$$

Point like charges of magnitude Ze present in the solar plasma make the form factor to become $|F|^2 = Z^2$. However, considering the case of a plane electromagnetic wave incident on a stationary charge distribution of N point charges with magnitude $Z_i e$ at locations $\vec{r}_i$, the relevant squared form factor for the Primakoff cross section is

$$|F_N(\vec{q})|^2 = \sum_{i=1}^{N} Z_i^2 + \sum_{i,j=1}^{N} Z_i Z_j \cos\vec{q}\cdot\vec{r_{ij}}, \tag{4.6}$$

with $\vec{r}_{ij} = \vec{r}_i - \vec{r}_j$ being the relative coordinates of the point like charges.

The physical interpretation is straightforward: In a plasma, the particles mutually interact through their Coulomb fields and their motion is sligthtly correlated [50]. According to the theory of Debye and Hückel [51], stelar plasmas [52] may not make use of the Coulomb potential of a charge Ze, since in a medium of freely moving electric charges a Yukawa potential should be used instead:

$$\frac{Ze}{4\pi}\frac{1}{r} \rightarrow \frac{Ze}{4\pi}\frac{e^{-\kappa r}}{r}. \tag{4.7}$$

The main difference between both potentials is that the Yukawa one introduces on average a charge cloud at around a particle. Such effect is described by an exponential that multiplies the Coulomb potential and it is ruled by κ, the inverse of the Debye-Hückel radius. Cosidering the fine structure constant $\alpha = e^2/4\pi$ and a plasma volume V at temperature T, the Debye-Hückel radius can be defined as

$$\kappa^2 \equiv \frac{4\pi\alpha}{T}\sum_{i=1}^{N}\frac{Z_i^2}{V}. \tag{4.8}$$

The form factor that arises from the use of the Yukawa potential in a stelar plasma is described by the use of the Debye and Hückel radius and assigns to

each particle of charge Ze on it an effective from factor:

$$|F_{eff}(\vec{q})|^2 = Z^2 \frac{|\vec{q}|^2}{\kappa^2 + |\vec{q}|^2}. \tag{4.9}$$

4.2.1 Axion emission from the solar plasma

Axions can efficiently be produced in the Sun via the Primakoff effect. In the interior of the Sun, blackbody photons can convert into axions thanks to the fluctuating electric fields of the charged particles that constitute the solar plasma. The differential cross section for the Primakoff production of axions in the Sun *(equation 4.3)* allows to obtain [47] the transition rate for a blackbody photon whose energy is ω:

$$\frac{d\sigma_a}{d\Omega} = \frac{1}{2}\frac{g_{a\gamma\gamma}}{4\pi}\left[\frac{e}{m_e}\right]^2 \cdot Z^2 \left[\frac{1}{4}\left(\frac{1+\cos\theta}{1+2(\kappa/2\omega)^2-\cos\theta}\right)\right]. \tag{4.10}$$

The expression of *equation 4.10* is obtained for scattering angles near the forward direction and integration over the scattering angles yields the total cross section:

$$\sigma_a(\gamma \to a) = \frac{1}{2}\frac{g_{a\gamma\gamma}}{4\pi}\left[\frac{e}{m_e}\right]^2 \cdot Z^2 \left[\frac{4\pi}{4}\left(\left(1+\frac{\kappa^2}{4\omega^2}\right)\ln\left(1+\frac{4\omega^2}{\kappa^2}\right)-1\right)\right]. \tag{4.11}$$

4.2.2 Differential axion flux on Earth

Hans Bethe[1] modeling of stellar nucleosynthesis provides an explanation for the energy source of the stars. Two are the main processes of energy loss in stars: the proton-proton chain and the Carbon-Nitrogen-Oxygen cycle.

According to the standard solar model, proton-proton chain provides more than ninety-eight percent of the energy required to produce the presently observed

[1] Nobel Prize for his paper "Energy Production in Stars" (1939).

solar luminosity, while the Carbon-Nitrogen-Oxygen cycle is the responsible for an extra 1.5% [55].

The core is the only location of the Sun that produces an appreciable ammount of heat via fusion reactions[2] $T_c \sim 4.5 \times 10^6\,\mathrm{K}$. Its dimension is about 20 % of the solar radius and has a density up to $\rho_c \sim 1.5 \times 10^5\,\mathrm{kg/m^3}$. The knownledge of this quantities allows to determine the Debye-Hückel radius ($\kappa = 9\,\mathrm{keV}$) since the plasma frequency in the solar core is $\omega_p = 0.3\,\mathrm{keV}$ [56].

Rewriting *equation 4.11* in terms of the known parameters enables the calculation of the photon-to-axion rate generation in the solar core:

$$\sigma_a(\gamma \to a) = \frac{1}{2} g_{a\gamma\gamma} \left[\frac{1}{m_e}\right]^2 \cdot \kappa^2 T \left[\frac{1}{4}\left(\left(1 + \frac{\kappa^2}{4\omega^2}\right)\ln\left(1 + \frac{4\omega^2}{\kappa^2}\right) - 1\right)\right]. \tag{4.12}$$

The axion luminosity of the Sun can be obtained considering the rate of axion production coming from photons of energy ω *(equation 4.12)* and the blackbody photon distribution of the solar core. The axion emission from the Sun is directly related to the temperature of its plasma and, since there exists a gradient of the interior temperature of the Sun, the flux of axions is related to the Sun radius considered for its calculation.

G. Raffelt [47] calculates the total diferential axion flux convolutioning the standard model of the Sun and its luminosity $L_\odot = 3.85 \times 10^{33}\,\mathrm{erg\,sec^{-1}}$ to the rates of axion production that arise after using the blackbody radiation spectrum applied to the temperature of the solar core. A parametrization for the differential axion flux on Earth can be given as

$$\frac{d\phi_a}{dE_a} = 6.020 \times 10^{10} \cdot g_{10}^2 \cdot E_a^{2.481} e^{-E_a/1.205}\,\mathrm{cm^{-2}s^{-1}keV^{-1}}. \tag{4.13}$$

The differential axion flux on Earth relative to $g_{10}^2 = (g_{a\gamma\gamma}/10^{-10}\,\mathrm{GeV^{-1}})$ can be plotted as it appears in *figure 4.2*.

Figure 4.3 is a contour plot of the solar surface luminosity of axions $\psi_a(E_a, r)$

[2] Proton-proton chain.

as a function of the axion energy E_a and a dimensionless radial coordinate r on the solar disc.

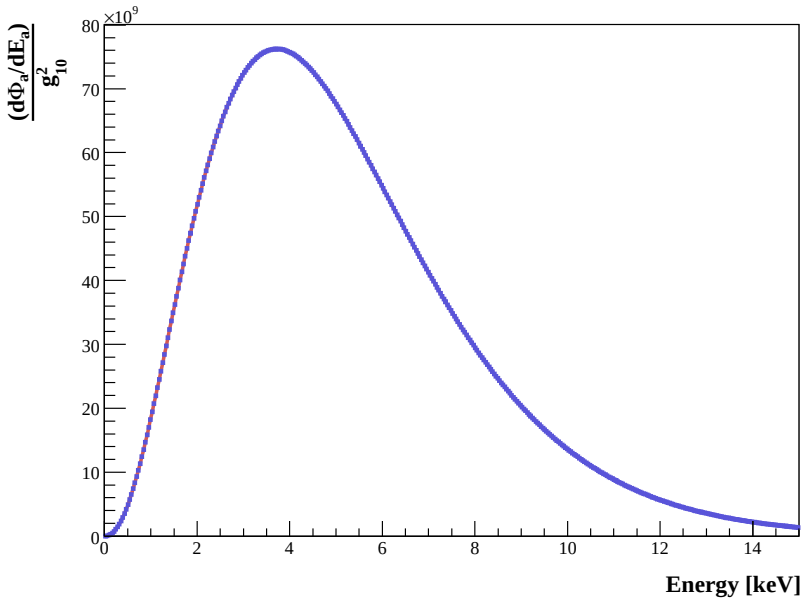

Figure 4.2: *Differential axion flux at the Earth surface due to Primakoff production in the solar core.*

4.3 Probability of axion conversion

The proposed detection mechanism for solar axions arriving to Earth is their reconvertion to X-ray photons via the Primakoff effect in the presence of electromagnetic fields. Existing large superconducting magnets would be suitable for such purpose.

Axion-to-photon conversion in the presence of a nearly homogeneous magnetic field B is only effective when the polarization plane of the photon is parallel to the magnetic field [54]. The axion flux on Earth satisfies the differential spec-

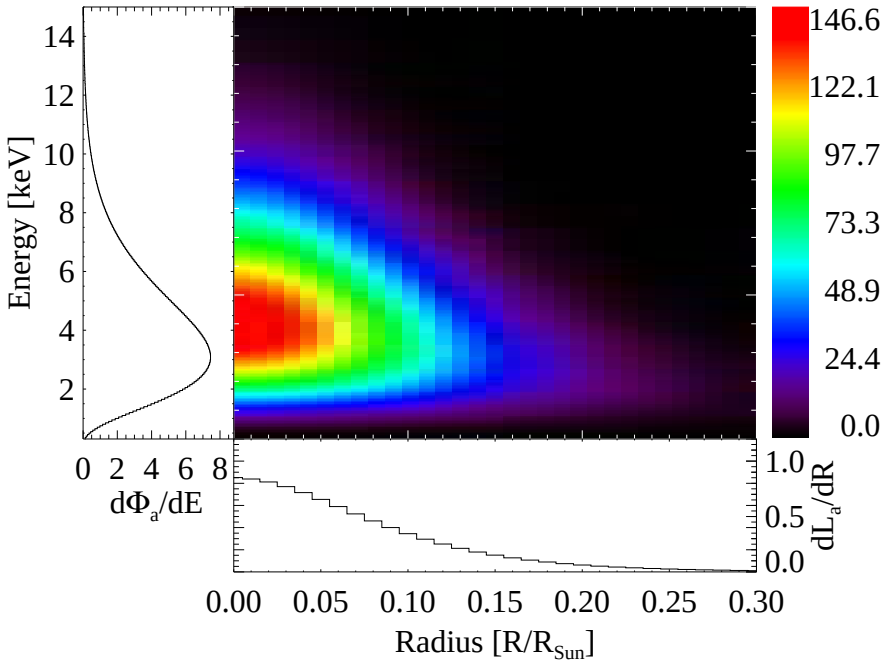

Figure 4.3: *Solar axion surface luminosity depending on the blackbody photon energy for a certain radius r of the solar disc* (taken from ref. [68]).

trum of *equation 4.13* and their propagation through the proposed conversion region must be transverse to the magnetic field.

Denoting by $A_{||}$ the amplitude of the parallel photon component and by *"a"* the axion, the wave *equation 4.14* defines the state of the particle in a media that has a transverse magnetic field $B_{\perp}$ along the coordinate z:

$$\begin{pmatrix} A_{||} \\ a \end{pmatrix}_f = -\int i \cdot dz \begin{pmatrix} E_a - \dfrac{m_\gamma^2}{2E_a - i\Gamma/2} & g_{a\gamma\gamma} \cdot \dfrac{B_\perp}{2} \\ g_{a\gamma\gamma} \cdot \dfrac{B_\perp}{2} & E_a - \dfrac{m_a^2}{2E_a} \end{pmatrix} \begin{pmatrix} A_{||} \\ a \end{pmatrix}_i . \tag{4.14}$$

While g_{10} rules the strength of the axion-to-photon coupling, the $(1,1)$-term of the matrix $(\mathcal{H}_{11})$ reflects the fact that in a given media, the photon acquires an effective mass m_γ and it observes a refractive index. Moreover, the existence of media implies an specific free path for the photon, phenomenon that can be described by introducing Γ, the damping factor for the X-ray in the media.

In general, B, Γ and m_γ depend on the *z-coordinate*. I will consider the wave equation *4.15* since it generalizes the particle state for a given *z-coordinate*:

$$\begin{pmatrix} A_{||} \\ \\ a \end{pmatrix}_f = \mathcal{H}(z) \begin{pmatrix} A_{||} \\ \\ a \end{pmatrix}_i . \tag{4.15}$$

The probability of having an X-ray photon at a given *z-coordenate* due to a Primakoff conversion into the magnet is given by the Fermi's golden rule:

$$\mathcal{P}_{a\to\gamma} = \frac{2\pi}{\hbar}|\langle a(z=0)|\mathcal{H}(z)|A_{||}(z)\rangle|^2\rho(E_a). \tag{4.16}$$

Assuming homogeneity for the media immersed on the magnetic region in which the conversion is expected to happen, we can consider m_γ and Γ as constants. In such a case, the transfer of momentum q between an axion and a photon in the media is

$$q = \Big|\frac{m_\gamma^2 - m_a^2}{2E_a}\Big|. \tag{4.17}$$

For the case of a uniform magnetic field $B_\perp$ applied for a length $z = L$, the probability of conversion of an axion into a photon due to the Primakoff effect in the media can be written as

$$\mathcal{P}_{a\to\gamma} = \Big[\frac{g_{a\gamma\gamma}}{10^{-10}GeV^{-1}}\Big]^2\Big[\frac{B_\perp}{2}\Big]^2\cdot\frac{1}{q^2+\Gamma^2/4}\cdot[1+e^{-\Gamma L}-2e^{-\Gamma L/2}\cos qL], \tag{4.18}$$

with $g_{a\gamma\gamma}$ ruling the strength of the axion-to-photon interaction.

4.3.1 Coherence of the interaction

In absence of a damping gas For the case of vacuum in the conversion region, the probability of the axion-to-photon coupling of *equation 4.18* can be written replacing $\Gamma = 0$:

$$\mathcal{P}_{a\to\gamma} = \Big[\frac{g_{a\gamma\gamma}}{10^{-10}GeV^{-1}}\Big]^2\Big[\frac{B_\perp L}{2}\Big]^2 \cdot \frac{2}{q^2L^2} \cdot [1-\cos qL]. \tag{4.19}$$

Calling $|\mathcal{M}|^2$ the factor that rules the coherence of the interaction, the probability of conversion can be written as

$$\mathcal{P}_{a\to\gamma} = \frac{1}{4}\Big[\frac{g_{a\gamma\gamma}}{10^{-10}GeV^{-1}}\Big]^2 B_\perp^2 L^2 \cdot |\mathcal{M}|^2. \tag{4.20}$$

A simple representation of the coherence term $|\mathcal{M}|^2$ *(see equation 4.21)* as a function of qL/π shows that the coherence of the interaction is maximum when $qL \ll 1$ *(see figure 4.4)*:

$$|\mathcal{M}|^2 = \frac{2}{q^2L^2} \cdot [1-\cos qL] = \Big[\frac{2}{qL} \cdot |\sin\frac{qL}{2}|\Big]^2. \tag{4.21}$$

The coherent condition mentioned above affects the range of axions masses for which the conversion axion-to-photon occurs. The energy equations for the incident axion and the outcoming photon are

$$\begin{aligned} E_a^2 &= m_a^2c^2 + \mathcal{K}_a^2 \\ E_\gamma^2 &= \mathcal{K}_\gamma^2. \end{aligned} \tag{4.22}$$

Considering the momentum transfer q of an axion to the photon and energy conservation, we can express from the previous equations that

$$q = \mathcal{K}_\gamma - \mathcal{K}_a = E_\gamma - \sqrt{E_a^2 - m_a^2c^2} = E_a - E_a\sqrt{1-\frac{m_a^2c^2}{E_a^2}}. \tag{4.23}$$

From the fact that $m_a \ll E_a$, we can approximate the momentum transfer as $q \simeq m_a^2/2E_a$ and, therefore, the axion mass range for which the coherence of

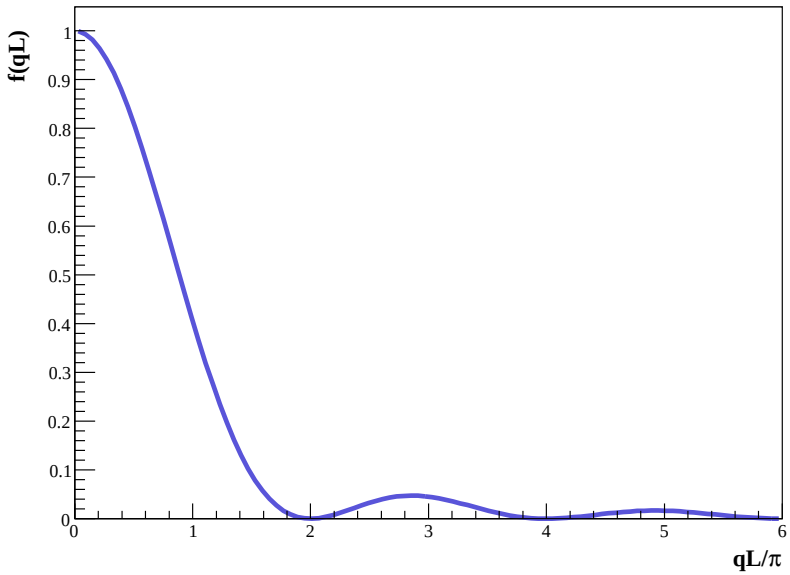

Figure 4.4: *Evolution of the coherence term respect the different values of qL. Observe that the value of the coherence term is maximum for small values of qL and vanishes really fast whenever the condition $qL \ll 1$ is not satisfied.*

the conversion is fulfilled satifies

$$m_a^2 \ll 2\frac{E_a}{L}. \tag{4.24}$$

From this relation, we can estimate the band of axion masses for which an experiment is coherent *(see equation 4.25)*. For the case of a magnet length of $\sim$ 10 m and $\sim$ 10 keV energy photons, the axion masses have to satisfy $m_a \lesssim 0.02\,\mathrm{eV}$ in order to fulfill the coherence condition $qL/\pi \ll 1$:

$$qL = \frac{\left(m_a^2/1\,\mathrm{keV}^2\right)\cdot(\mathrm{L}\cdot 1\,\mathrm{keV})}{2\left(E_a/1\,\mathrm{keV}\right)} = 2533.865621\times\frac{\left(m_a^2/\mathrm{eV}^2\right)\cdot\left(\mathrm{L/m}\right)}{\left(E_a/\mathrm{keV}\right)}. \tag{4.25}$$

Damping gas in the magnet An extension of the axion mass range for which a certain experiment is coherent while vacuum is in the conversion region can be achieved by filling the magnet cavity with a certain gas of electron density n_e.

As result, the arising photon from the conversion acquires an effective mass thanks to the existence of the damping gas:

$$m_\gamma c^2 = \sqrt{4\pi r_0}\hbar c \cdot \sqrt{n_e} = a \cdot \sqrt{n_e}. \tag{4.26}$$

Helium gas is a nice candidate for filling the magnet conversion region since the free path of X-ray photons in its presence is large. Assuming the use of Helium gas and knowing that at standard conditions a mol of any gas occupies $\simeq$ 22.4l, the number of Helium electrons in such conditions will be $n_e^*(He)$:

$$n_e^*(He) = 2 \times \frac{6.02214199 \times 10^{23}\,\mathrm{mol}^{-1}}{22.413996 \times 10^3\,\mathrm{cm}^3\,\mathrm{mol}^{-1}} = 5.373555 \times 10^{19}\,\mathrm{cm}^{-3}. \tag{4.27}$$

Real conditions of pressure and temperature in the magnet conversion region may differ from standard ones. But, since Helium gas satisfies the equation of the ideal gases, for a temperature T_{He}, the pressure of the Helium gas with n_e electrons follows

$$P_{He} = \left(\frac{n_e}{5.373555 \times 10^{19}}\right) \times \left(\frac{T_{He}[K]}{293.15}\right) \times \left(\frac{1}{V_{He}[\mathrm{cm}^3]}\right) \mathrm{atm} \tag{4.28}$$

and *equation 4.29* describes the number of electrons in the gas referred to the conditions of pressure and temperature of the magnet:

$$\sqrt{n_e} = 1.211522 \times 10^{11} \cdot \left(\frac{P_{He}[atm]}{T_{He}[K]}\right)^{1/2} \mathrm{cm}^{-3}. \tag{4.29}$$

Then, the effective mass of the photon in the Helium gas of the magnet can be

written as

$$m_\gamma = 4.498716\sqrt{\frac{P_{He}[\text{atm}]}{T_{He}[\text{K}]}}\,\text{eV}. \tag{4.30}$$

The momentum transfer to the photon has to take into account its effective mass in the medium *(equation 4.31)*, which means an alteration of the coherence condition calculated for the vacuum case:

$$q = \Big|\frac{m_a^2 - m_\gamma^2}{2E_a}\Big|. \tag{4.31}$$

For a magnet of length L that has Helium as damping gas, the actual coherence condition is

$$qL = 2533.865621 \times \frac{\Big[(m_a^2 - m_\gamma^2)/\text{eV}^2\Big] \cdot \Big[\text{L/m}\Big]}{\Big[E_a/\text{keV}\Big]}. \tag{4.32}$$

The above expression clearly shows that the coherence condition for the axion-to-photon coupling is fulfilled in the pressence of a damping gas whenever $m_a \simeq m_\gamma$.

This is equivalent to say that in order to restore the coherence of conversion for different axion masses, the pressure of the Helium gas in the magnetic region must be tunned. This adjustment is really sensitive, since variations of $\sim 0.1\,\text{mbar}$ would destroy the coherence of the specific axion mass.

4.3.2 Absorption of converted photons due to the damping gas

As it appears in *equation 4.18*, the probability of having a photon due to the Primakoff conversion of an axion with energy E_a in a magnet with length L depends on the momentum transfer to the photon and the effective damping Γ due to the existence of a certain gas in the magnet conversion region.

It has been mentioned in *Section 4.3.1* that the existence of a damping gas allows to extend the coherence of conversion for higher axion masses by tunning its pressure according to *equation 4.30*.

However, the existence of gas in the magnet affects the free path of a photon that has been converted in the magnet and therefore its detection after a length L. Photoelectric effect, together with the coherent and incoherent scattering of photons are the responsibles of such phenomenon. In terms of the different cross sections of each process we can say that the total absorption cross section in the dumping gas is

$$\sigma_A(E_a) = \sigma_{Photoelectric}(E_a) + \sigma_{Coherent}(E_a) + \sigma_{Incoherent}(E_a). \tag{4.33}$$

With those processes playing the rule of the photon absorption in a certain gas whose mass number is A, we will define the *mass attenuation coefficient* $\mu(E_a)$, a quantity that is used to describe the reduction of intensity of a certain energy beam as it passes through a specific material:

$$\mu(E_a) = \frac{N_{Avogadro}}{A} \cdot \sigma_A(E_a). \tag{4.34}$$

Having a gas in the magnet region, the damping factor can be expressed in terms of the density of the gas for the specific pressure and temperature of the magnet. In *Section 4.3.1*, Helium was already suggested as a candidate able to restore the coherence of the axion-to-photon conversion.

The probability of conversion *(equation 4.18)* takes already into account the possible loss of intensity from the presence of a certain media in the conversion region. Its effect is described by Γ, whose dependence with the energy of the photon generated in the conversion and the pressure in the magnet can be written as

$$\Gamma(P_{He}, E_a) = \rho_{STP}\Big[\frac{g}{\mathrm{cm}^3}\Big] \cdot \mu(E_a)\Big[\frac{\mathrm{m}^2}{\mathrm{gr}}\Big] \cdot \frac{T_{STP}}{P_{STP}} \cdot \frac{P_{He}}{T_{He}} \times 10^6\,\mathrm{m}^{-1}. \tag{4.35}$$

The attenuation of photons in the presence of Helium *(see equation 4.36)* is related to the density of gas in the magnet pipe and their energy. Therefore, it is important to parametrize as a function of the energy E_a and the pressure P_{He} the ratio between the total damping calculated from the data bases[3] and

[3]NIST Online Scientific Databases.

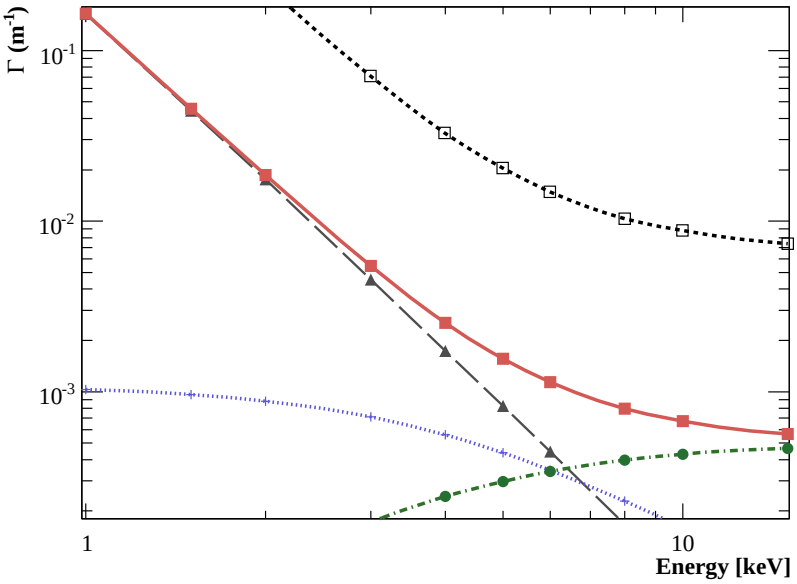

Figure 4.5: *Recreation of the damping function for 1 mbar of Helium at 1.8 Kelvin due to the different attenuation processes in Helium gas. In the low keV energy range, the most contributing effect to the total damping (red squares) is the photoelectric effect that appears in the graph in grey triangles. However, for energies above 4 keV, the highest contribution to the damping comes from the incoherent scattering of photons (green circles). The coherent scattering (blue crosses) it also contributes to the total damping. In black squares the total damping that photons suffer when the Helium gas is at 13 mbar in the magnet.*

the relative conditions of Helium in the magnet:

$$\log_{10}\Gamma_{P_{He},E_a} = -2.0282\cdot\log_{10}^5 E_a \;+\; 4.7254\cdot\log_{10}^4 E_a \;-\; 2.3282\cdot\log_{10}^3 E_a \;+$$
$$+\; 0.4296\cdot\log_{10}^2 E_a \;-\; 3.1864\cdot\log_{10} E_a \;-\; 0.7834 \;+\; log_{10}P_{He}. \tag{4.36}$$

Figure 4.6 shows how the parametrized function describes some of the total

attenuation of photons at different pressures.

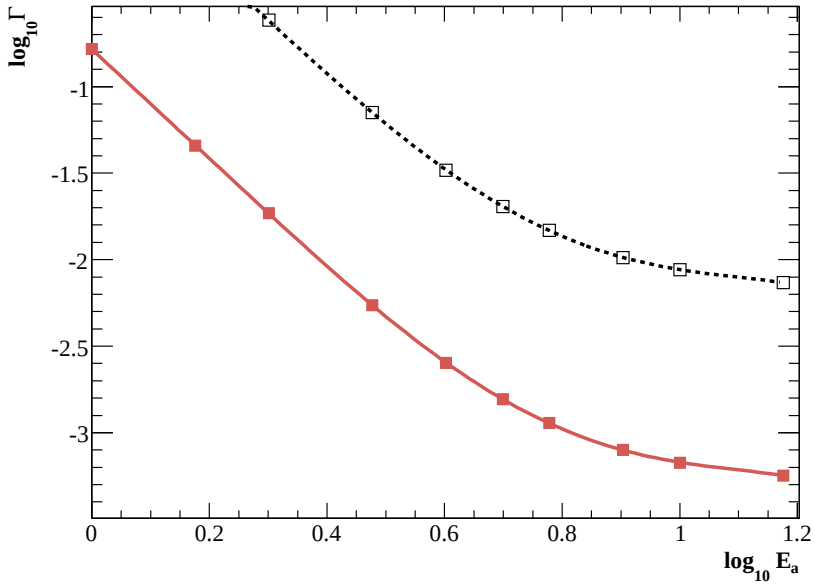

Figure 4.6: *Parametrized function of the total attenuation that photons suffer for the pressures of* 1 *(red) and* 13 *mbar (black) when the temperature of Helium is* 1.8 K. *The squares represent some of the experimental data points, while the lines are the result from the parametrization.*

4.4 Expected number of photons

Once we have described the phenomenology of the axion-to-photon conversion in the presence of a magnetic field, time has come to think of how to detect the outcoming X-ray photons.

The use of X-ray detectors placed at the exit of the magnet cavity will make

possible the detection of the outcoming photons. But, how many photons do we expect?

The total number of photons $\mathcal{N}_\gamma$ is a dimensionless number that arises from the consideration of several factors that intervine on the axion-to-photon conversion and the detection of the generated photons. Two are the most important factors contributing to the expectation of photons:

- The differential axion flux on Earth: given by *equation 4.13*.
- The conversion probability: studied deep into detail in *section 4.3*.

While the probability of conversion is dimensionless, the differential axion flux on Earth needs the input of two quantities in order to provide the number of axions expected on Earth for the different energies of the spectrum: the exposure time t and the effective area S in which is possible to have a conversion.

With all this information, we could obtain the total number of photons expected from the conversion as

$$\mathcal{N}_\gamma = \int_{E_o}^{E_f} \frac{d\phi_a}{dE_a}(E_a) \cdot \mathcal{P}_{a\to\gamma}(E_a) \cdot S \cdot t \cdot dE_a. \tag{4.37}$$

However, there are no perfect systems. Losses of photons due to obstacles, quantum efficiency of each detector and efficiency of the analysis used in order to reconstruct the events observed in the detectors must be also taken into account. Comprehending all this effects, we will introduce to the *equation 4.37* a new energy dependent factor to which we will refer as detector efficiency $\varepsilon(E_a)$.

Equation 4.38 takes into account the influence of this extra consideration to the total number of X-ray photons $\mathcal{N}_\gamma$ to be observed in a certain detector:

$$\mathcal{N}_\gamma = \int_{E_o}^{E_f} \frac{d\phi_a}{dE_a}(E_a) \cdot \mathcal{P}_{a\to\gamma}(E_a) \cdot S \cdot t \cdot \varepsilon(E_a) \cdot dE_a. \tag{4.38}$$

Part II

The CAST experiment

Chapter 5

The CAST experiment

The CERN Axion Solar Telescope (CAST), situated at the LHC Point 8 of CERN (Conseil Européen por la Recherche Nucléaire) is an axion telescope that aligns a transverse magnetic field with the solar core to allow axion-to-photon conversion via the Primakoff effect.

CAST makes use of a decommisioned LHC superconducting magnet installed on top of a moving platform in order to detect the possible arrival of axions to Earth. As already explained in *Chapter 4*, the axion-to-photon conversion due to the Primakoff effect could make possible their detection.

Figure 5.1: *The CAST experiment.*

CAST, with its moving platform, is able to track the solar core twice per day. In the sunrises, as well as in the sunsets, CAST looks for axions coming from the solar core during one hour and a half.

Different X-ray detectors are installed at the end of the magnet bores of the CAST experiment so that the conversion of axions due to the presence of a transverse magnetic field into X-ray can be detected.

In the following lines we will proceed to describe the magnet of CAST and its tracking system *(Sections 5.1 and 5.2)*. The Helium system that allows the tunning of the axion masses is also presented in *Section 5.3* and the different detectors used during the ^{4}He data taking period of CAST are shown in *Section 5.4*.

5.1 Magnet characteristics

A decommissioned LHC superconducting test magnet forms the basis of the experiment. The first generation of bending magnets have two straight bores. Each bore of the twin aperture magnet has a cross-sectional area $A = 14.5\,\mathrm{cm}^2$ and the provided nominal field is 9 T over a length of 9.26 m.

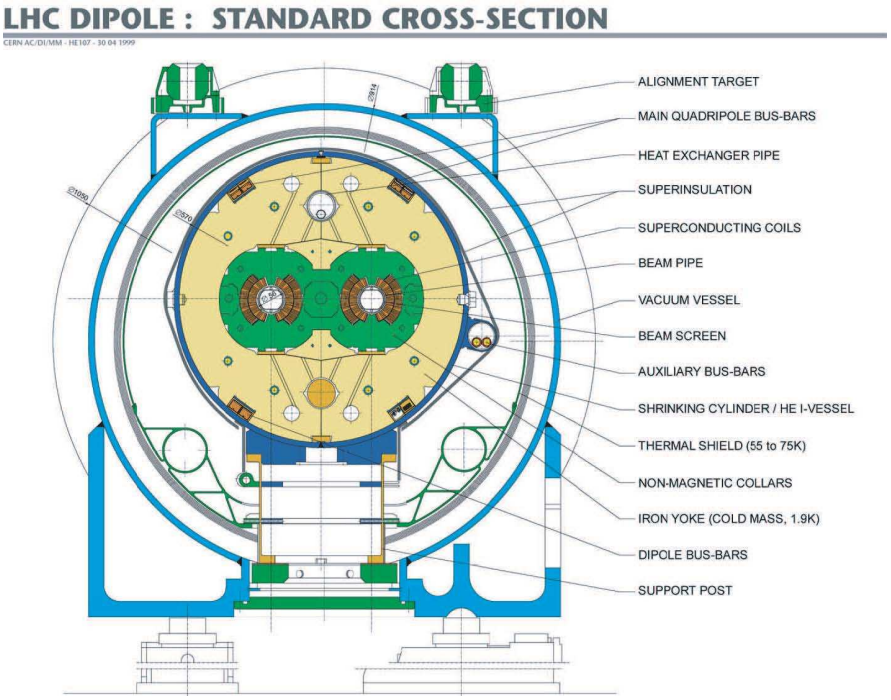

Figure 5.2: *View of the CAST dipole cross section.*

The CAST dipole magnet is built with materials that become superconducting for temperatures below 4.5 K allowing it to stand currents above 13 kA. Thus,

a complete cryogenic setup is needed in order to cool down the dipole magnet and keep it superconducting.

In CAST, as with the rest of the LHC magnets, the use of superfluid Helium is a technique that allows not only to cool down the magnet but also to stabilish its temperature at 1.8 K.

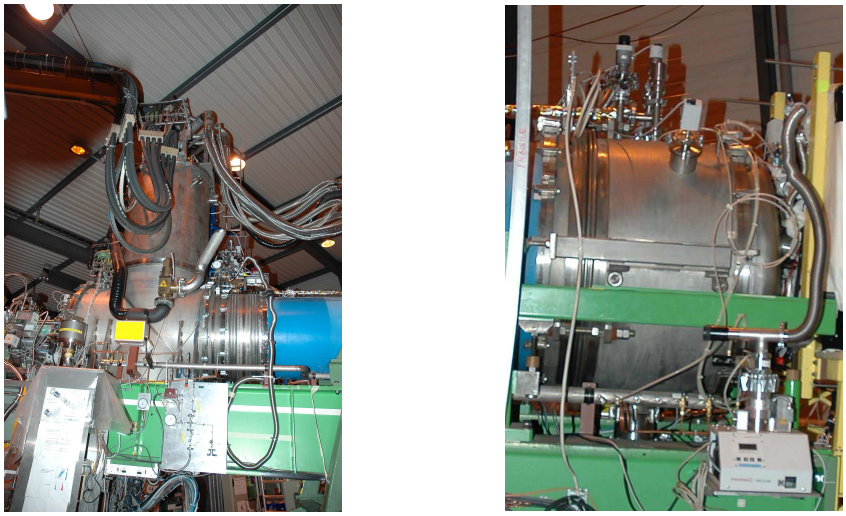

Figure 5.3: *Image of the CAST's Magnet Feed Box (left) and of the CAST's Magnet Return Box (right).*

The LHC magnets are able to reach superconductivity for temperatures of ~ 4.5 K. However, for technical issues, the LHC magnets make use of the fact that Helium reaches superfluidity at 2.17 K. Superfluid Helium is able to cool down the LHC magnets and it also allows to tilt the LHC magnets $\pm 8^o$, fact that CAST uses in order to track the Sun.

The Magnet Feed Box (MFB [82]) is fixed on top of the magnet towards its sunset end *(see figure 5.3)*, while the other end is closed by the Magnet Return Box (MRB). Flexible transfer lines for the Helium and the quench recovering system allow movement of the whole structure. The "Potence", a movable gibbet, fulfills the same purpose for the power supply lines.

Figure 5.4: *Potence gibbet for the power supply lines of the CAST magnet.*

A quench is an interesting phenomenom connected with superconducting magnets. The sudden change from the superconductive to the normal-conductive state of the material due to the presence of impurities generates an electric resistivity that provokes a violent warming of an specific magnet region due to the Joule effect.

The heat, generated by the Joule effect, is dissipated thanks to the presence of cold Helium in the magnet cryostat. In a quench, Helium gasifies and generates an overpressure of gas in the cryostat that must be released in order to preserve the integrity of the system *(see figure 5.5)*.

Figure 5.5: *Image of a QUENCH in the CAST experiment.*

5.2 Tracking system

CAST, as an axion helioscope, has to be able to follow the Sun. The tracking system allows to move the whole experiment over 40 tons within a precission of 0.01^o. In order to track the Sun, a reliable software determines where to put the magnet and actually direct it to go to the required positions. In order to performe a tracking, CAST makes use of the ephemeris of the Sun.

5.2.1 Ephemeris of the Sun

An ephemeris is a look-up table that provides the positions of the Sun or planets at a given time. Modern ephemeris includes a software that calculates position of celestial bodies, such as stars, planets, comets or satellites for vir-

tually any desired time.

In order to calculate the Sun's ecliptic[1] several commercial and non-comercial software routines are available. The most widely used and generally accepted is NOVAS[2] provided by the U.S. Naval Observatory [79]. NASA offers an online Ephemeris Computation Service, known as JPL's[3] HORIZONS System [80].

To actually calculate the ephemerides is a problem that needs to solve a multi-body system: Other planets influence the Earth's path around the Sun, and therefore its orbit is not exactly elliptical [81]. The usage of different coordinate and time systems allow the calculations.

- **Horizontal Cordinate System**
  Ofently used for the calculation of the sunrises and sunsets, but hardly ever to determine ephemerides.
- **Equatorial Cordinate System**
- **Ecliptic Cordinate System**
- **Galactic Cordinate System**
  This system uses the so-called galactic plane as the reference plane, i.e. the planar region, where most of the visible mass can be found. The directions perpendicular to the plane point towards the galactic poles, and thus create a spherical coordinate system. Its coordinates are galactic latitude and galactic longitude.
- **Supergalactic Cordinate System**

Transformations between the given coordinate systems exist, but the formulas for this can be rather complicated. Since not only space, but also time matters in ephemeris calculation, there exist several time systems used in celestial

[1] The geometric plane which contains the orbit of the Earth is called ecliptic. Most planet's orbits in the Solar System are close to this plane.
[2] Naval Observatory Vector Astrometry Subroutines
[3] Jet Propulsion Laboratory

calculations:

- **Julian Date**
- **International Atomic Time (TAI)**
- **Ephemeris Time (ET)**
- **Universal Time (UT)**
  Is a timescale based on the rotation of Earth, can be seen as a continuation of Greenwich Mean Time (GMT), which is the mean solar time on the meridian of Greenwich, England.
- **Coordinated Universal Time (UTC)**
- **Sideral Time**

Ephemeris calculations are quite complex. Phenomena like the analemma, provoked by the Earth's tilt on its axis and its elliptic orbit arround the Sun is one of the examples. Also, the aberration caused for the situation of the observer in a moving planet, or changes through runtime of the light for long distances are effects to be considered.

For this reasons, tracking the Sun precisely is a challenging task. The CERN Axion Solar Telescope tracking system is based on NOVAS. The galactic coordinate system as well as the horizontal coordinate system are used.

5.2.2 Hardware

Mechanical setup The magnet, described in *Section 5.1*, is mounted in a platform composed of two strong metallic supports *(see figure 5.6)*.

In order to be able to track any object of the sky with the CAST magnet, the whole structure must be able to move in horizontal as well as vertical directions. The knowdlege of the magnet axis in the galactic coordinates allows

the alignment of CAST with sky objects like the Sun.

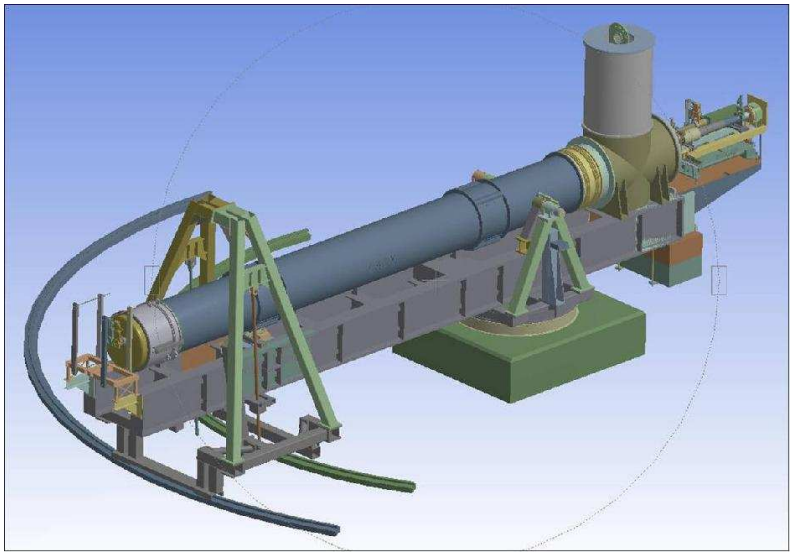

Figure 5.6: *Design of the CAST moving system.*

On the *figure 5.6*, the first part of the support for the magnet platform moves the magnet along the circular rails on the floor for an angle of about 80^o in azimuthal direction. This triangle-like structure on the left side of the *figure 5.6* has two calibrated screws attached to its support, such that it allows the vertical movement of the magnet platform.

On the center of mass of the CAST magnet, a turntable forms the second support of the magnet platform allowing it to rotate horizontally and vertically . The mechanical setup of the CAST experiment, allows a total range of movement of $\pm 40^o$ in horizontal and $\pm 8^o$ in vertical direction. We must remember that the magnet cryogenics constrains its vertical movement to $\pm 8^o$ and that the feeding lines of cryogenics and electricity have to be decoupled from the magnet movement.

Consequently, the magnet can be aligned with the solar core for aproximately an hour and a half during sunrise and for the same period of time during sunset every day. In the course of a year, this results in a total alignment time of more or less 50 days, if the horizontal range of movement is considered as well.

Motors and encoders The magnet platform is moved by two electric motors. One for horizontal and the other for vertical movement. Each motor is connected to an encoder so that the different positions of the magnet along the experimental area of CAST are differenciated within the proper accuracy.

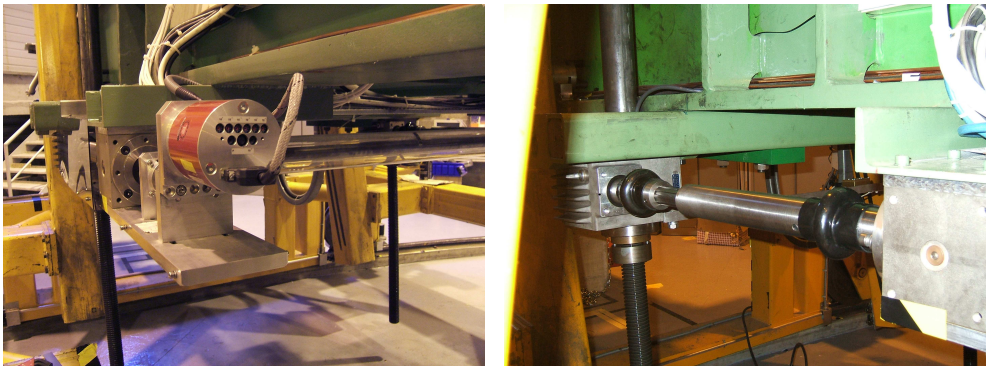

Figure 5.7: *Image of the Vertical movement system of the CAST magnet (left) and its encoder (right).*

The movement system has also several emergency stops for all the directions of movement in order to prevent the experimental setup from damage. These emergency stops are hardware switches as well as software limits, both mean to protect the magnet from tilting too much or derailing while moving.

5.2.3 Software

Tracking software and logging of data The tracking software guides the magnet's movement and, it writes relevant information to logfiles that are used

Figure 5.8: *Image of the Horizontal movement system of the CAST magnet (left) and the encoder readers for both, vertical and horizontal movement (right).*

for data analysis later on.

The software is written in Labview and based on NOVAS. These subroutines, read in the UT Time as well as the coordinates of the experiment[4] at CERN in order to calculate the azimuthal angles (AZ) and the zenith distances (ZD) of the Sun for the minute to come.

After calculating the azimuth and zenith values of the Sun, the software transforms these values to the corresponding encoder numbers $V_x(AZ, ZD)$ and $V_y(AZ, ZD)$. It also transfers the coordinates to the motors, that are then guided to move the magnet to this position.

In order to achieve an accurate tracking, the UT time is obtained by the time syncronication of the host PC's clock with two CERN time servers every milisecond. Also, the help from the EST[5] division at CERN was crucial to

[4] 46^o N $15''$ E, 330 m above sea level
[5] Engineering Support and Technology

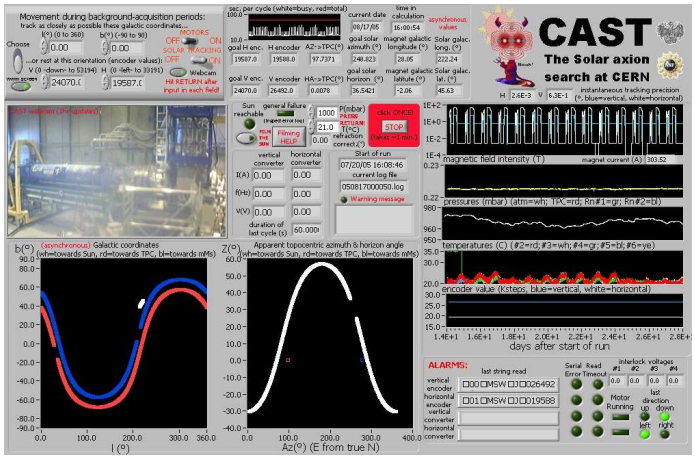

Figure 5.9: *Image of the tracking PC of the CAST experiment.*

apply the correct coordinate translation at any point of the experiment *(see Table 5.1 for a summary of possible errors)*.

Source of Error	Typical Value	Maximal Value
Astronomical Calculations	0.002^o	0.006^o
Uncertainty of Coordinates (CERN)	$\sim 0.001^o$	
Clock Time	$\sim 0^o$	
Grid Measurements (0.02 mm precision)	0.001^o	
Interpolation os Grid Measurements	0.002^o	$< 0.01^o$
Horizontal Encoder precision	$\sim 0.0014^o$	
Vertical Encoder precision	$\sim 0.0003^o$	
Linearity of Motor Speeds	$< 0.002^o$	
TOTAL	$< 0.01^o$	

Table 5.1: *Summary of possible error sources of the solar tracking precision.*

The slow control Is an independent LabView program that monitorizes and record most of the experimental parameters that are necessary for controlling the stability of the CAST experiment and also for the proper analysis of the data, since it is a useful tool to avoid any source of systematic errors in the data. Information, such as the status of the valves, the load on each of the screws and the position of the magnet in encoder values, are recorded. Also, an alarm system is established in order to keep the experiment under surveillaince and, if necessary alert people in charge.

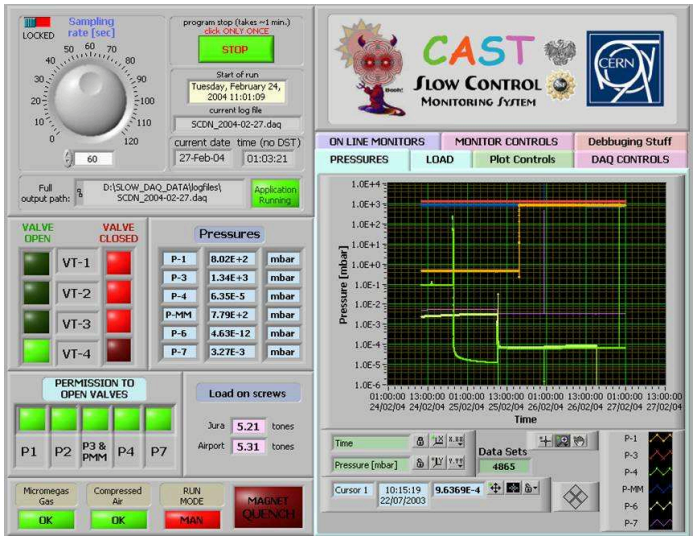

Figure 5.10: *Image of the Slow Control PC of the CAST experiment.*

5.2.4 Filming of the Sun

It is an independent crosscheck of the tracking accuracy of the CAST experiment. A CCD camera aligned with the axis of the magnet is able to directly film the Sun while tracking.

The Sun filming can be done twice a year, during the months of March and September, and it is able to provide enough information as to compare it with the GRIDS that the EST division at CERN used to calibrate the movement of the CAST magnet.

Refraction of light in the atmosphere is the most important effect to be considered while the Sun filming is performed.

Atmospheric refraction Earth atmosphere is able to change the direction of the incoming light rays. This phenomenon is called atmospheric refraction and may fake the apparent coordinates of a given point on the celestial sphere.

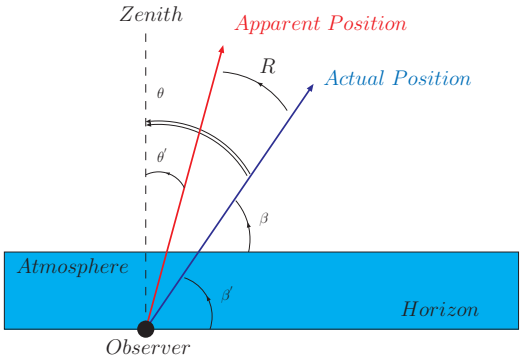

Figure 5.11: *Atmospheric refraction. $\beta^{'}$ represents the apparent altitude, while β stands for the true height above the horizont. $\theta^{'}$ and θ are the apparent and true zenit distance respectively.*

Being θ the true zenit distance, and $\theta^{'}$ the apparent one, we can define refraction R as

$$R \equiv \theta - \theta^{'}. \tag{5.1}$$

Equivalently, we could also consider the true and the apparent altitude above the horizont, β and $\beta^{'}$ respectively in order to determine the refraction:

$$R \equiv \beta - \beta^{'}. \tag{5.2}$$

Since $\theta^{'} = 90^{o} - \beta^{'}$ and $\theta = 90^{o} - \beta$, equations *5.1* and *5.2* are equivalent. Earth's atmosphere density decreases with altitude, which makes an incoming ray to be bent towards the surface *(see figure 5.11)*.

The filming software The version of the tracking software for the filming mode of the CAST experiment can be accessed via the normal user interface of the tracking PC. The refraction in the atmosphere is taken into account in real-time [84,85].

The filming setup At present, a CCD camera borrowed from the MPE[6] with appropiate optics and polarized filters suits the purposes of CAST's Sun filmings [86].

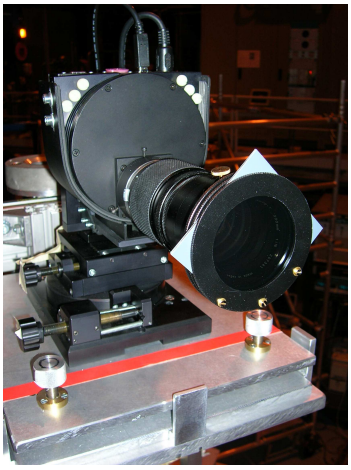

Figure 5.12: *Picture of the CCD ST-7 camera used for the Sun filming.*

[6]Max Planck Institute for Extraterrestrial Physics in Munich

The camera is installed in a platform able to simplify the alignment of the camera's optical axis with the magnet axis that points to the solar core. Two targets and a laser allow to setup the magnet axis:

- **Cross-wire:** Taylor-Hobson sphere with two 3 mm diameter crossing copper wires in its center that is placed in the optical axis at 5.02 m from the camera.
- **Pointer:** Diaphragm with two aluminum pointers placed in the optical axis at 7.59 m from the camera.
- **Laser:** Beam parallel to the theoretical magnet axis at the level of the camera $ST-7$.

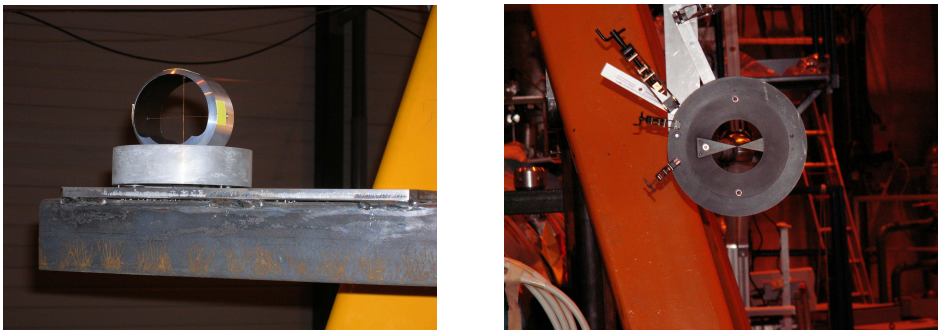

Figure 5.13: *Image of the Crosswires (left) and pointer used for the Sun filming (right).*

The laser spot provides the theoretical center of the Sun and allows to obtain the offset of CAST while the Sun tracking is taking place.

5.3 The Helium System

During the second phase of the CAST experiment the Helium gas has been the one chosen to fulfill the coherence requirement of the conversion probabil-

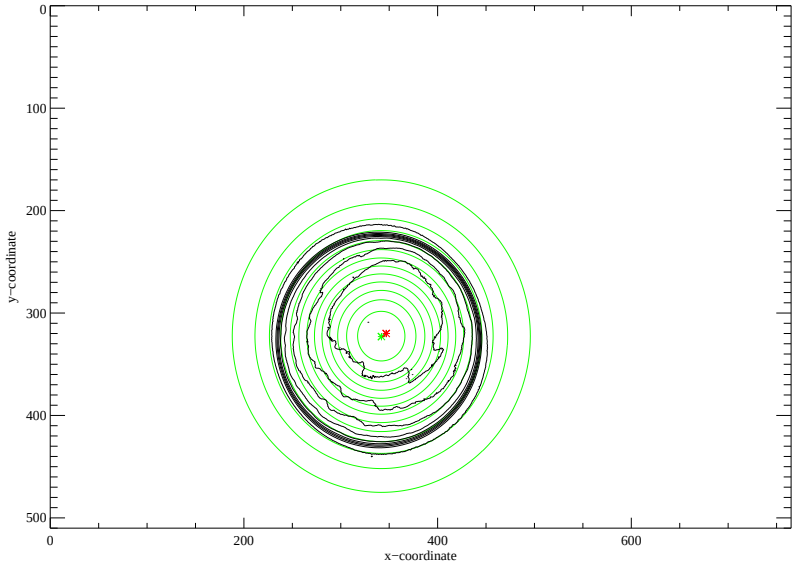

Figure 5.14: *Best fit to a three dimensional gaussian for the image of the Sun in the CCD chip of the ST − 7 camera. In green the contour plot of the best fit. The red star is the theoretical magnet axis and the green cross the center of the best fit function* (figure taken from [59]).

ity *(see Section 4.3)*.

In the first setup of the second phase, the ^{4}He has been used to restore the coherence for axion masses up to 0.39 eV. The vapour pressure of ^{4}He, 16.4 mbar at the temperature of operation of the CAST magnet, restricts the axion mass range for which CAST is sensitive. Once the ^{4}He reaches its vapour pressure, it starts liquifying, fact that constraints the achievable pressure with ^{4}He in the magnet bores.

CAST will make use as well of ^{3}He gas in order to extend the sensitivity to axion masses up to 1.2 eV. As in the case of ^{4}He, the vapour pressure of ^{3}He (135.6 mbar) will limit the range of operation. Moreover, latest cosmological results from the cosmological microwave background suggest an upper

limit for the axion mass at around 1 eV.

5.3.1 Gas confinement. The X-ray windows

To confine the gas in the magnet, four cold windows were developed at the CERN cryolab. The requirements for the gas confinement system were the following:

- *High X-ray transmission*
- *Robustness*
- *Tightness*
- *Pressure Proof*

To accomplish the above requirements, the windows were constructed with an stainless steel strongback that gives robustness to the system and, on top of it, a foil of 15 μm polypropylene is deposited.

Figure 5.15: *View of one of the four cold windows before its installation inside the CAST cryostat.*

These windows are able to keep the Helium gas separated from the vacuum side of the magnet and the detectors.

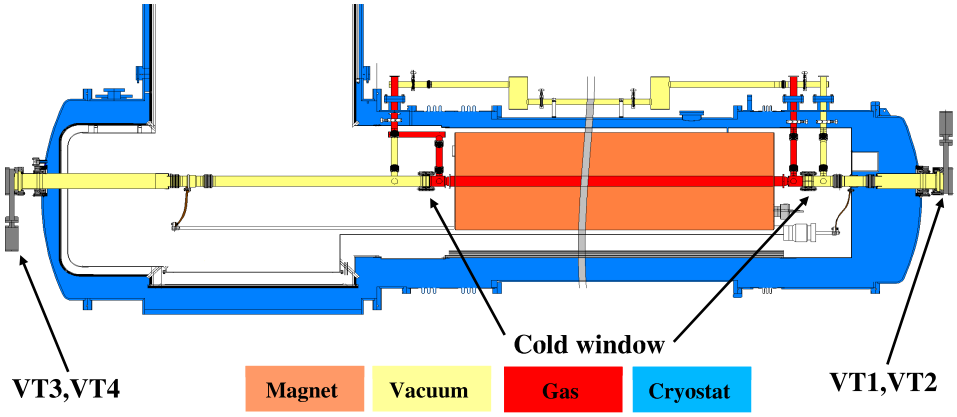

Figure 5.16: *View of the vacuum and Helium system scheme of the CAST experiment. The cryostat of CAST offers four ports (VT1, VT2, VT3 and VT4) for the installation of the X-ray detectors. The cold windows are placed such that are able to keep the Helium gas (red) within the magnet region of the cryostat (orange). Note that between the windows and the ports to which the detectors are connected there is vacuum (yellow).*

The axion-to-photon conversion takes place inside the magnet bore, where X-ray can be produced. The use of the $15\,\mu$m polypropylene allows the X-ray transmission, being around 95 % at 4.2 keV.

The leak tightness of the system is fundamental. Any loss of gas would imply a change to the coherence condition. For that pourpose, several vacuum cycling test were performed to the cold windows and the overall leak was found to be less than $1 \times 10^{-7}\,\mathrm{mbar\,l\,s^{-1}}$ of Helium.

Also, the resistance of the windows to the sudden change of pressure had to be ensured, since a possible quench of the magnet would produce a fast increase of the pressure for the Helium present in the cold bore. For that pourpose, the

cold window prototype was cycled up to 3.5 bar without loosing its propierties of tightness and robustness. Neither the rest of the windows showed any weakness while cycling them up to 1 bar.

5.3.2 Gas injection

The injection of Helium gas into CAST's magnet bores needs of a metrological pressure measurement with the following capabilities:

- *Accuracy*
- *Reproducibility*
- *Stability*

The whole system is focused to the reproducibility of a given pressure setting within an error of 0.01 mbar. This feature allows CAST to visit at any time previously measured settings.

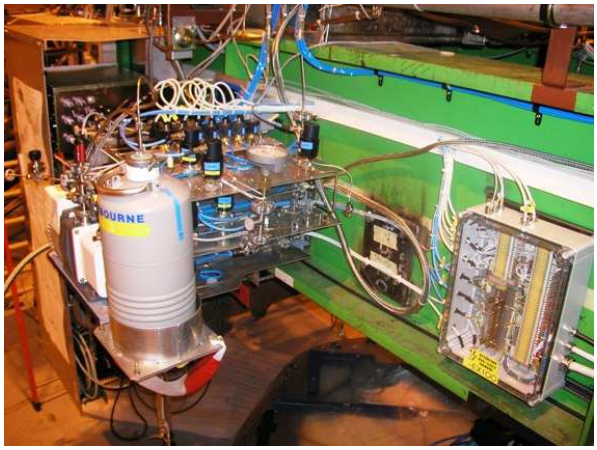

Figure 5.17: *Gas metering system. The metering volume is inmersed in a controled thermal bath of water.*

To keep the absolute control of the system, all the volumes have to be properly calibrated and thermally monitorized so that the gas to be used in order to restore the coherence condition of the axion-to-photon probability suffers a controled transit to the magnet bores.

Prior to injection of the Helium gas to the magnet bores, CAST makes use of a metering stage composed of a calibrated volume of 21 inmersed in a thermal bath of water which keeps the gas in stable conditions. The use of such technique allows the accuracy of the gas injection to be better than 60 ppm. Its implementation for the CAST experiment can be seen in *figure 5.17*.

The transfer of the Helium gas from the metering volume to the CAST magnet bores is done by means of a flowmeter valve that is able to establish a constat flow so that the gas dynamics is fully controlled during the operation. For the ^{4}He phase of the CAST experiment, the filling of the magnet bores was done when the magnet was not taking data, so that the Helium gas had enough time to thermalize with the stainless steel surface of the magnet bore.

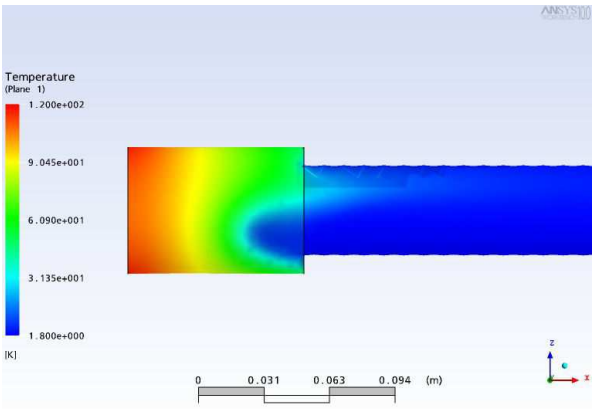

Figure 5.18: *Simulation for the temperature profile of the Helium gas of the coldbore* (figure taken from [60]).

The behaviour of the Helium gas of the cold bores was also simulated by means

of computational fluid dynamics modeling. The experimental measurements performed in the CAST experiment agree with the simulations and are the proof of having an homogenous temperature for the Helium gas of the cold-bore in the regions for which the magnetic field is present *(see figure 5.18)*.

5.3.3 Gas recovery and purification

In the case of a magnet quench, the temperature of the CAST magnet will suddenly increase and, therefore, the pressure of the Helium gas inside the cold bore will rise up to $\sim 2.7\,\text{bar}$. This effect forces the CAST experiment to design a recovery system for the Helium gas such that the increase of pressure in the magnet pipes does not damage the coating of the cold windows.

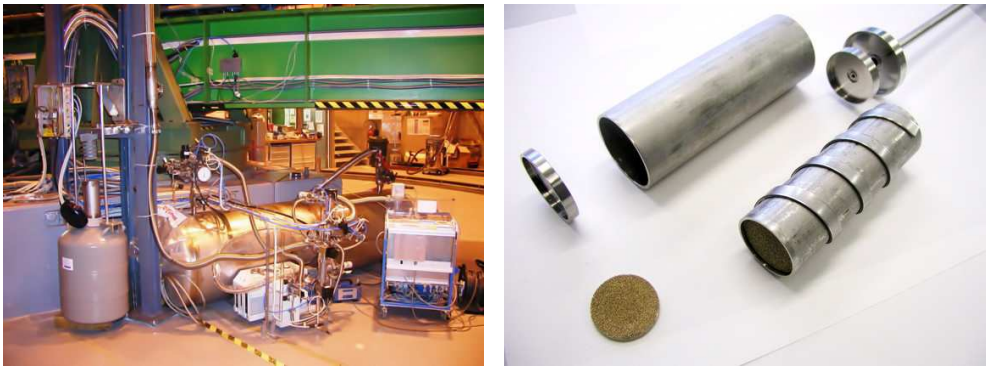

Figure 5.19: *On the left the recovery system of the CAST experiment. The right picture corresponds to a detailed picture of the trap used for the gas purification.*

The recovery of the Helium gas is done by connecting the cold bore to an expansion volume that reduces the pressure of the Helium gas. For the hypothetical vacuum leaks, a purification stage consisting of a cold trap has been also implemented. This whole mechanism allows CAST to keep the purity of the Helium gas that is used in order to restore the coherence of the axion-to-photon probability.

5.3.4 Reliability

The CAST Helium gas system has proven to be reliable and its daily opertation is a establish proccedure for the CAST shifters.

Regarding the Helium gas system, the stability of the pressure in the cold bore is the main worry, since espontaneous acoustic oscillations of gas columns could be generated in a tube with step temperature gradients.

The study of possible thermoacoustic oscillations in the cold bore of CAST has shown agreement with literature.

During ^{4}He Phase of the CAST experiment, the use of pressure transducers inside the cold bore together with home made dampers blocked the flow of gas to warmer regions and stoped the oscillations.

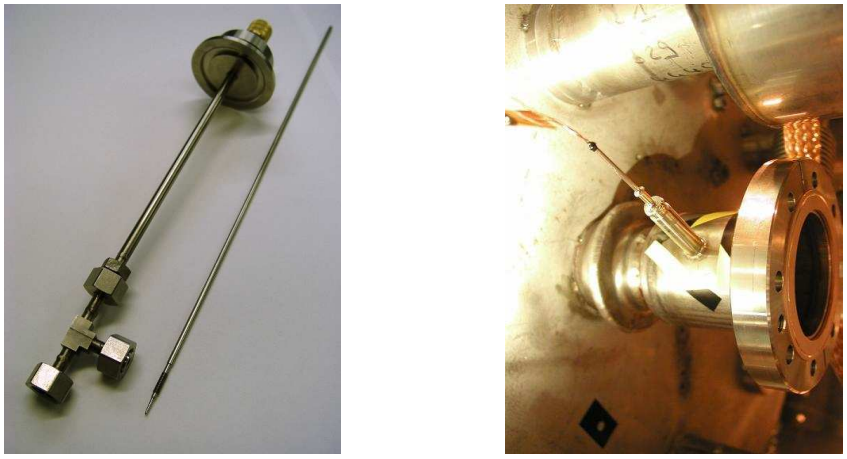

Figure 5.20: *Image of the cryogenic needle valve used in CAST (left) and its implementation in the cold bore of the magnet (right).*

However, during the ^{3}He Phase, due to the high pressures that are needed to

restore the coherence, the dampers are no longer effective blocking the thermoacoustic oscillations. Cryogenics needle valves are needed in order to block the flow of Helium gas towards warmer regions of the magnet.

The absence of thermoacoustic oscillations gives to CAST a completely homogenous gas density within the magnetic region and establish CAST as the most sensitive helioscope for axion masses up to 1.2 eV.

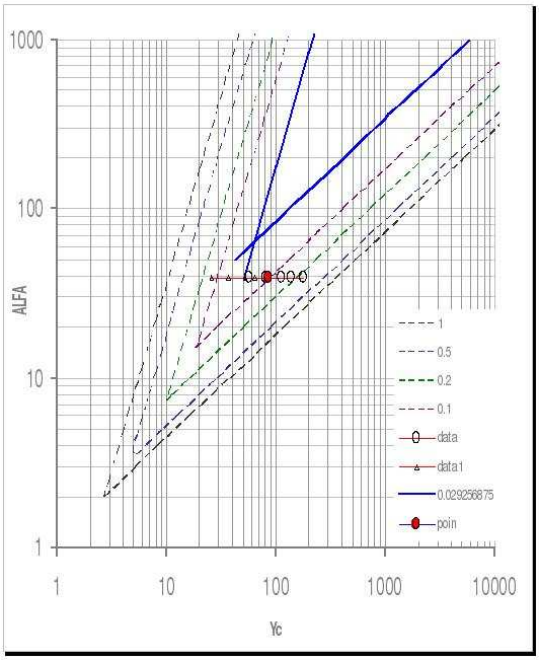

Figure 5.21: *Plot for the region of thermoacoustic oscillation in CAST (blue lines forming a triangle) and the different pressure settings that are used in CAST (dots). The vertical axis represents the temperature ratio between the magnet bore and the temperature of the metering volume, while the horizontal axis is the ratio between the diameter of the tubes* (figure taken from [60]).

Figure 5.21 shows how the pressure settings at the temperature of the CAST magnet avoid the region for which the thermoacoustic oscillations occur.

5.4 Detectors

In order to detect the X-ray photons originated from the axion-to-photon conversion in the magnetic field, several low-background detectors are used. Their sensitivity range, between 1 and 15 keV cover perfectly the differential axion flux spectra that can be seen in *(figure 4.2)*. A TPC (Time Projection Chamber) was located at one end of the magnet and covered both magnet bores looking for sunset axions.

The other side of the magnet looks for sunrise axions. CAST has two detectors mounted on this side. One bore is covered by a MICROMEGAS (MICROMEsh GAseous Structure) detector, while at the other a CCD (Charge Coupled Device) detector is looking for photons from axions. A special feature of the latter device is an X-ray mirror telescope added in between the magnet and the detector to focus the incoming photons on the sensitive chip.

All detectors take data during about one hour and a half per day, either in the morning or in the evening, depending on the side they are mounted on. During the remaining time, background measurements are performed and thus, the background for the individual detectors is measured with an exposure time that is approximately 10 times higher than the one for data taking.

5.4.1 The Time Projection Chamber

The TPC used at CAST, which took data during the sunset runs of the First and the ^{4}He Phase, is a conventional type of this kind of three-dimensional tracking detectors, often also referred to as electronic bubble chamber. The TPC principle of detection mechanism combines ideas from both Multiwire Proportional Chambers (MWPC) and drift chambers. The central part is a gas-filled volume, where incoming particles interact and thus produce free electrons. These drift towards a net of anode wires and produce an avalanche due to the strong field that increases the density of electrons and, therefore, the strength of the signal. The first coordinate is obtained from the firing anode wire, the second from the signal induced on the cathode wires, while the third is derived from the drift time. *Chapter 6* explains more into detail the characteristics of the TPC detector.

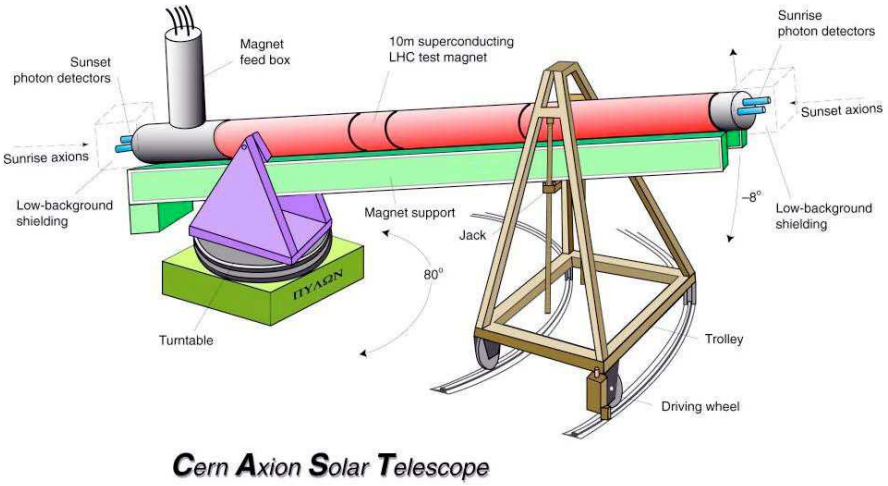

Figure 5.22: *Schematics of the CAST experiment. The Sunset and Sunrise sides of the CAST experiment determines the period of the day for which each side is able to look for axions coming from the Sun.*

Technical details TPC's conversion region has a volume of $10 \times 15 \times 30\,\mathrm{cm}^3$. The drift region of 10 cm parallel to the magnet axis is filled with a mixture of 95 % Argon (Ar) and 5 % Methan (CH_4) at atmospheric pressure. Total conversion ($\gtrsim 99\,\%$) of X-ray photons[7] up to 6 keV is allowed *(see Chapter 6)*. In more detail, the basic setup of the detector is described in *figure 5.24* and consists of a drift electrode made of aluminum close to the magnet as well as an arrangement of 3 planes:

- The anode plane at +1.85 kV with 48 wires (having a diameter of 20 μm each)
- The grounded cathode planes with 48 wires (having a diameter of 100 μm each)

[7] For higher photon energies, the conversion efficiency decreases reaching 50 % for 11.5 keV

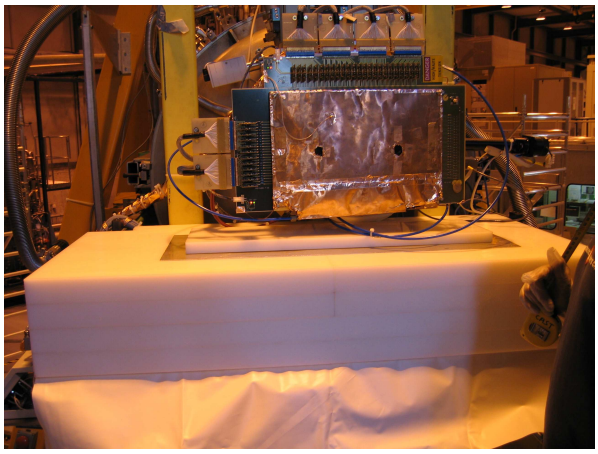

Figure 5.23: *TPC detector of the CAST experiment.*

The distance between two adjacent wires of the same plane is 3 mm, the gap between the cathode and the anode plane is 3 mm, while the distance between the cathode planes is 6 mm.

The predominant material used for the chamber is plexiglass (low natural radioactivity), some metallic parts and pices of other materials, such as the wires that are holded by the PCB[8].

Windows and differential pumping The TPC was connected to each magnet bore through a thin window (3 μm of aluminized mylar on a metallic strongback). This is necessary, since there exist 1 atm pressure difference between the gas in the detector volume and the vacuum inside the magnet *(For further details see 6.2.2)*.

Passive shielding A passive shielding was added to the experimental setup in order to reduce the background of the detector. From inside to outside,

[8]Printed Circuit Board

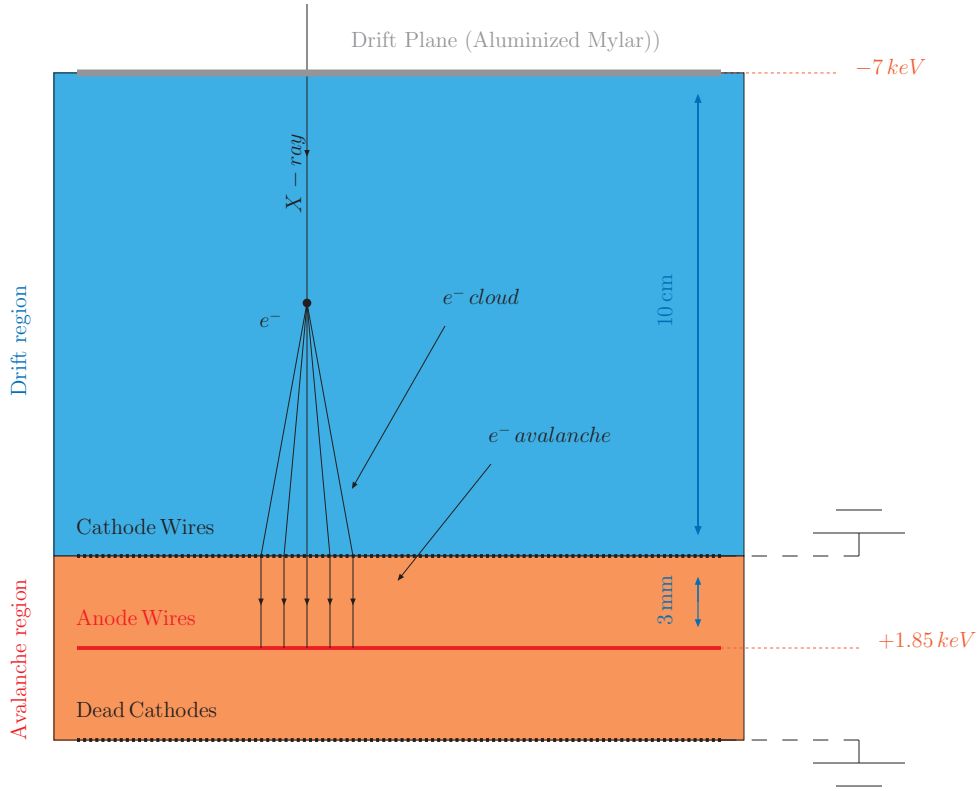

Figure 5.24: *Schematics of an X-ray event for the TPC. Anode and cathode planes of the TPC detector.*

it consisted of several layers: copper (5 mm), lead (2.5 cm), cadmium (1 mm), polyethylene (22.5 cm) and a plastic covering to flush the interior with pure N_2 gas *(for further details see Section 6.5)*.

Calibration and data taking Four times a day, the TPC detector was automatically calibrated using an ^{55}Fe source. Performance stability due to its robust conventional design as well as its low background due to the shielding implementation were the main advantages of the TPC used at CAST.

5.4.2 The MICROMEGAS detector

The other gaseous chamber used at CAST is smaller than the TPC and has a MICROMEGAS readout [64]. It is attached to one of the two magnet bores that faces the sunrise and, unlike the TPC, the MICROMEGAS does not make use of wire planes but a micromesh to separate the drift from the avalanche region. The principle of operation that such a detector uses is shown in *figure 5.25*.

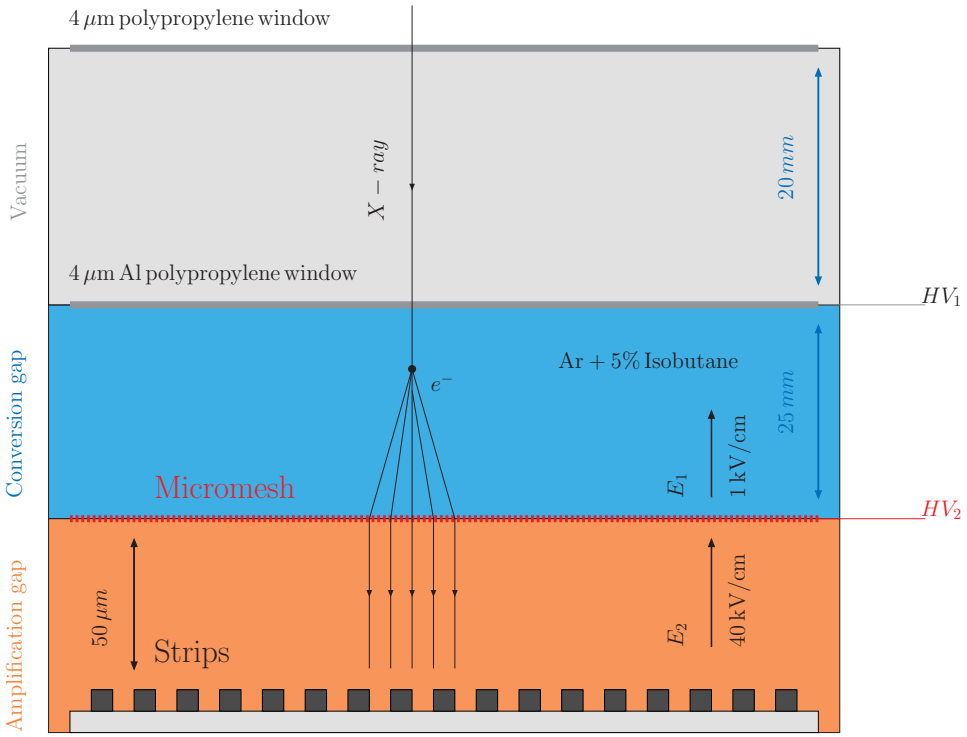

Figure 5.25: *Schematic view of the MICROMEGAS detector used at CAST. The conversion gap of 25 mm is divided from the amplification region (about 100 μm) by a micromesh. For the signal readout X-Y strips are used (bottom)*

After passing the drift electrode, an incident particle will produce ion-electron

pairs within the conversion region. A drift voltage of $\sim$ 1100 V is able to displace the generated electrons to the amplification gap that is separated from the drift region by a grid: the micromesh. In order to reach a high electron transmission to the amplification region, a voltage of up to $\sim$ 400 V is applied. An avalanche process will occur after the electrons go through the mesh and the grid will keep the ions produced in the avalanche from re-entering the conversion region. The mesh collects the ions and is able to provide a trigger with the help of a Flash ADC. While ions are captured by the mesh, the electrons continue their way to the anode, where they are readout on a X-Y strips structure.

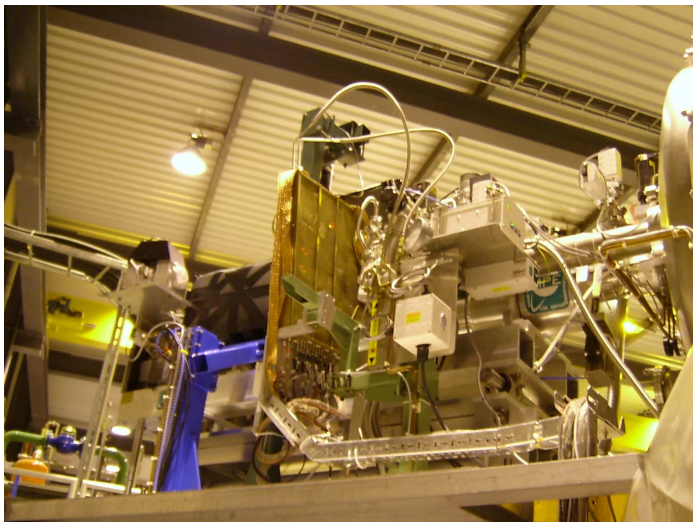

Figure 5.26: *Picture of the CAST micromegas.*

Technical details The frame of the detector is made of plexiglass and has a conversion region of 25 mm thickness with an amplification gap of 100 μm. The mesh consist of 5 μm copper with circular holes of 25 μm diameter and a separation distance of 50 μm. For the readout, there are 192 X-strips and the

same ammount for the Y-direction. The pitch is 350 μm and the gas used is a mixture of Argon with 5 % of isobutan.

Windows and differential pumping Being a gaseous detector, in order to fulfill the vacuum requirements of the CAST experiment, the MICROMEGAS makes use of a differential pumpping. The drift window of the MICROMEGAS is made of aluminized polypropylene whose thickness is 4 μm. For the differential window a 4 μm polypropylene is used.

Calibration and data taking In addition to the daily data taking, calibration and pedestal[9] runs were performed by shifters on morning shift. The high stability of the detector and its wonderful energy and spatial resolution allowed the MICROMEGAS group to achieve nice levels of background even though during the First and ^{4}He Phase the MICROMEGAS did not have a dedicated shielding.

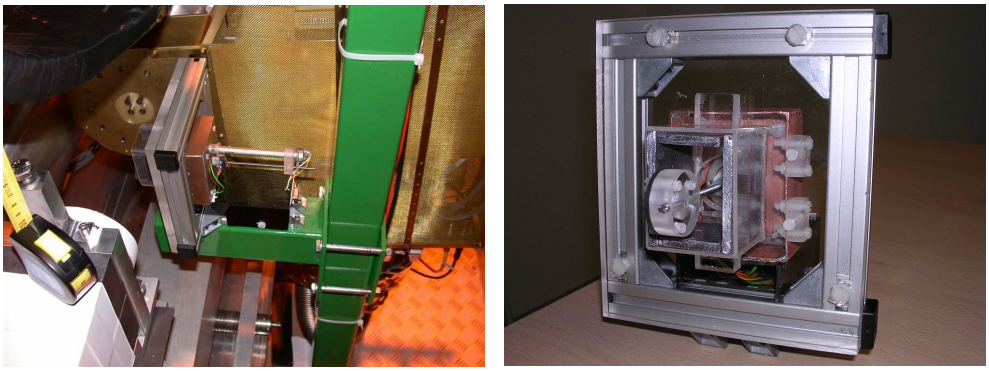

Figure 5.27: *Front view of the calibrator for the CAST micromegas (left) and rear view after its installation on place (right).*

[9]Pedestal runs are equivalent to the mean value of the charge measured by the strips without real triggers given.

5.4.3 The X-ray telescope and the pn-CCD detector

Consists of a focusing X-ray mirror telescope and a Charge Coupled Device (CCD). Its setup can be seen in *figure 5.28*.

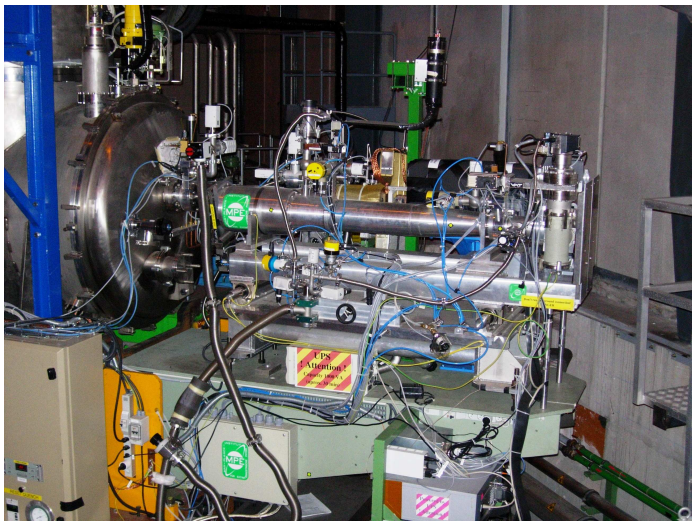

Figure 5.28: *pn-CCD detector and X-ray telescope setup in the CAST experiment.*

It is installed at the remainig fourth end of the two magnet bores. Originally, both parts were designed as prototypes for X-ray astronomy [76, 77]. The use of an X-ray telescope, allows CAST's setup to focus the incoming photons from axion conversion to a spot of approximately $9\,\mathrm{mm}^2$ on the CCD chip. Interaction of the X-ray with the silicon atoms of the pn-CCD generate electrons and holes. The electrons are captured in small potential cells below the surface and tranferred to the readout chip by being shifted from one cell to the next, conserving the charge distribution pattern achieved in the ionization process [63].

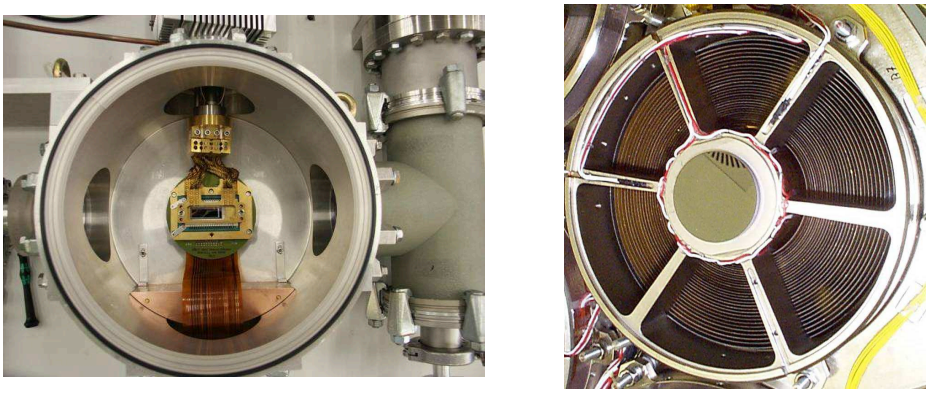

Figure 5.29: *Detailed view of the pn-CCD detector (left) and the X-ray telescope (right) used in the CAST experiment.*

The X-ray telescope The focusing device used at CAST is a Wolter I type X-ray mirror telescope, which was a prototype of the German X-ray satellite mission ABRIXAS[10]. It consists of an arrangement of 27 nested parabolic and hyperebolic mirror shells made of gold coated nickel. The diameter of the shells varies from 76 mm to 163 mm from the innermost to the outmost shell, respectively. A cobweb-like structure supports the shells *see figure 5.29*. Only one of the six sections is used at CAST, since the magnet bore has a diameter of 43 mm. The focal length of the telescope is 160 cm and it is operated under vacuum conditions at a pressures around 10^{-6} mbar to prevent the mirror shells from contamination.

The pn-CCD The pn-CCD detector, located in the focal plane of the X-ray telescope, is a prototype developed for the XMM-Newton[11] mission of ESA[12] [78]. The performance of the detector was optimized to fulfill the demands of low background application by adding a passive shielding made of copper and lead. The software background rejection has also been optimized

[10] A BRoad band Imaging X-ray All-sky Survey

[11] This name derives from the X-ray Multi-Mirror design used and is meant to honor Sir Isaac Newton.

[12] European Space Agency

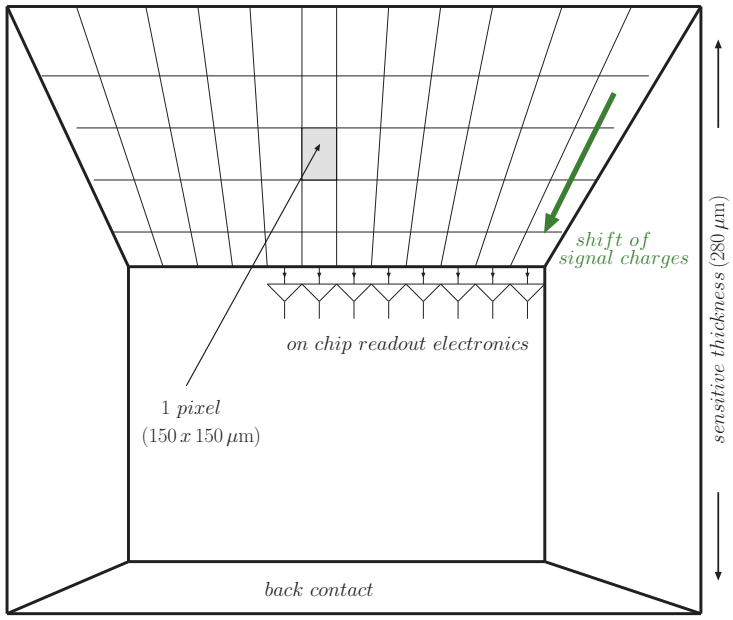

Figure 5.30: *Schematics for the charge collection of the pn-CCD detector.*

with the help of a pattern recognition algorithm.

The chip, with a sensitive area of $2.88\,\mathrm{cm}^2$ is larger than the expected image of the solar core that the X-ray telescope generates. Sun's core, $\sim 0.2\,R_\odot$, corresponds to approximately 19 pixels diameter. The focalization of the magnet bore area to the CCD chip allows to measure simultaneously the potential signal from axion to photon conversion and the background of the detector.

Calibration and data taking Every morning, before the solar tracking, a calibration with a ^{55}Fe source is performed. The most important characteristic of the X-ray telescope is the improvement of the signal to background ratio by a factor of about 200 due to focusing with an X-ray telescope. Also, the very good spatial and energy resolution.

5.5 The CAST Physics Program

At the moment, CAST is the most powerful helioscope. CAST's goal is to scan for axions in all the reachable axion masses for which the coherence of the axion-to-photon conversion is fullfiled.

The first phase of CAST took place during 2003 and 2004 and the magnet remained under vacuum operation, which gave CAST the possibility to look for axion masses up to 0.02 eV. The result of the first phase of CAST did not show any candidate, but allowed to restric the coupling of axions to photons in the parameter space [68].

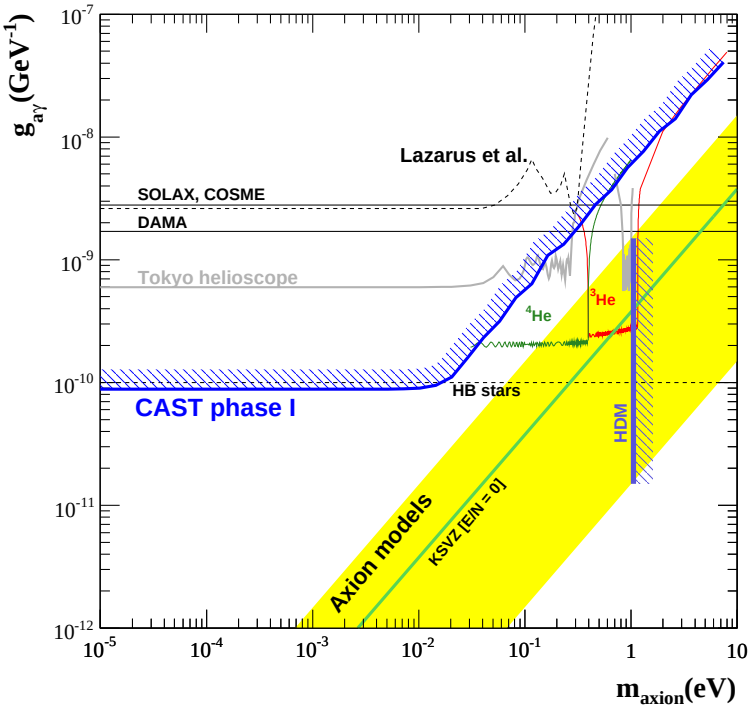

Figure 5.31: *Exclusion plot for the axion-to-photon coupling relative to its mass during the first phase of the CAST experiment.*

The combined result of CAST during its first phase is

$$g_{a\gamma\gamma} \lesssim 8.8 \times 10^{-11}\,\mathrm{GeV}^{-1}\,(95\,\%\,\mathrm{C.L})\ \text{ for }\ \mathrm{m_a} \lesssim 0.02\,\mathrm{eV}, \tag{5.3}$$

that is with difference the best result ever achieved in the direct solar axion searches by a helioscope.

In order to extend the coherence of the axion-to-photon conversion, an experiment like CAST could either play with the length of the magnet or insert a gas into the magnetic region so that the photon arising from the conversion acquires an effective mass. This two mechanism come from the fact that the coherence of the axion-to-photon conversion goes as $qL \ll 1$ as it has been explained in *Section 4.3.1*.

CAST strategy consits of using a damping gas in the magnetic field:

- ^{4}He run: Completed during 2005 and 2006
- ^{3}He run: Started in 2007

The use of ^{4}He has allowed CAST to scan for axions whose masses are below 0.39 eV. At present, with the help of ^{3}He, CAST is searching for axions whose $m_a \lesssim 1.20\,\mathrm{eV}$.

5.5.1 Description of the ^{4}He data taking

Every day CAST measured during the sunset and sunrise with an specific pressure in the cold bore.

The pressure of the cold bore was changed daily so that in little steps of 0.085 mbar CAST tunned 160 pressure settings that went from 0 to 13.4 mbar.

Each pressure setting restores the coherence for a certain axion mass and the step of pressure between pressure settings was chosen to overlap neighbouring steps. This overlaping strategy allows to have an almost constant discovery potential along the axion masses for which CAST is sensitive.

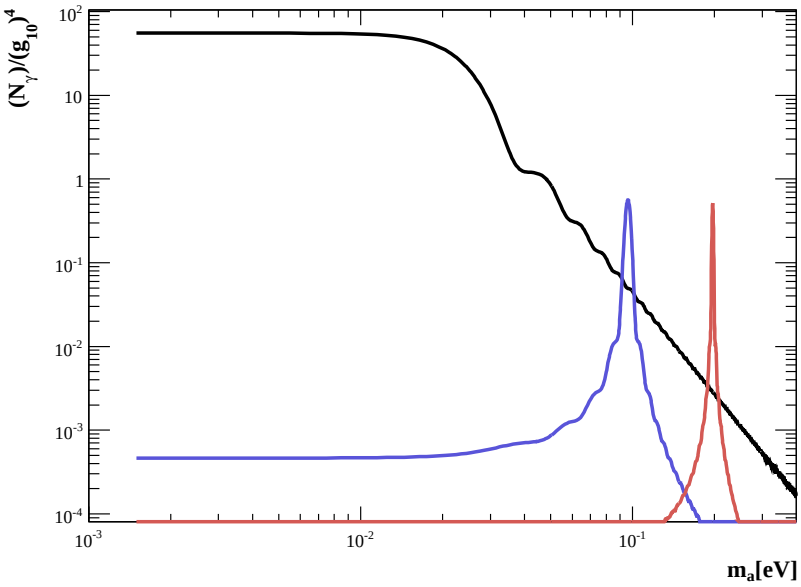

Figure 5.32: *Comparison between the expected photons from the axion-to-photon conversion due to Primakoff effect during the First phase of the CAST experiment (black) and the expectation for two different pressure settings during the ^4He Phase (red and blue). It can be appreciated how for axion masses above 0.02 eV the loss of coherence is restored in CAST by the use of ^4He as a damping gas. We can observe as well how the long exposure time of CAST First Phase makes the expectation of photons higher than for the single pressure settings of the Second Phase.*

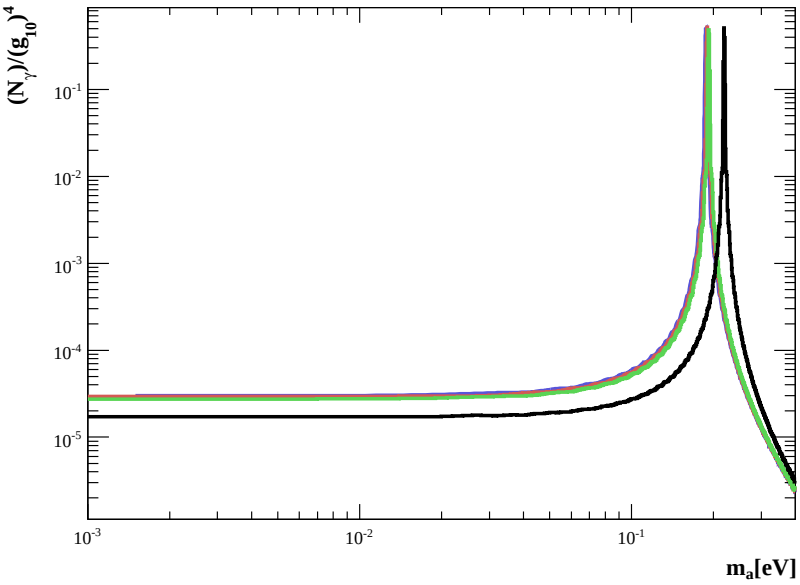

Figure 5.33: *Example of the expected photons from the axion-to-photon conversion for three consequtive pressure settings (blue, red and green) of the CAST experiment. In black the expected photons of a pressure setting twelve steps distant from the consequtive ones.*

Chapter 6

The TPC detector of the CAST experiment

Sunset solar axions traversing the intense magnetic field of the CERN Axion Solar Telescope experiment may be detected in a Time Projection Chamber detector, as point-like X-ray signals. The TPC, with a multi-wire proportional counter as a readout structure has been designed to provide high sensitivity to the detection of the low intensity X-ray signal expected in the CAST experiment. A low hardware threshold of 0.8 keV is set to a safe level during normal data taking periods, and the overall efficiency for the detection of photons coming from conversion of solar axions is 62 %. Shielding has been installed around the detector, lowering the background level to 4.10×10^{-5} counts keV^{-1}cm^{-2}s^{-1} between 1 and 10 keV.

The TPC detector is attached to the eastern end of the CAST magnet, covering both magnet bores and being therefore exposed to the converted photons from "sunset" axions during evening solar tracking.

The detector follows the well-known TPC concept, i.e., a large gaseous volume where primary interactions take place, producing ionization electrons which drift towards a plane of wires. Here, as in a Multi Wire Proportional Chamber, the avalanche process that amplifies the signal is developed, allowing a position sensitive readout of the original event.

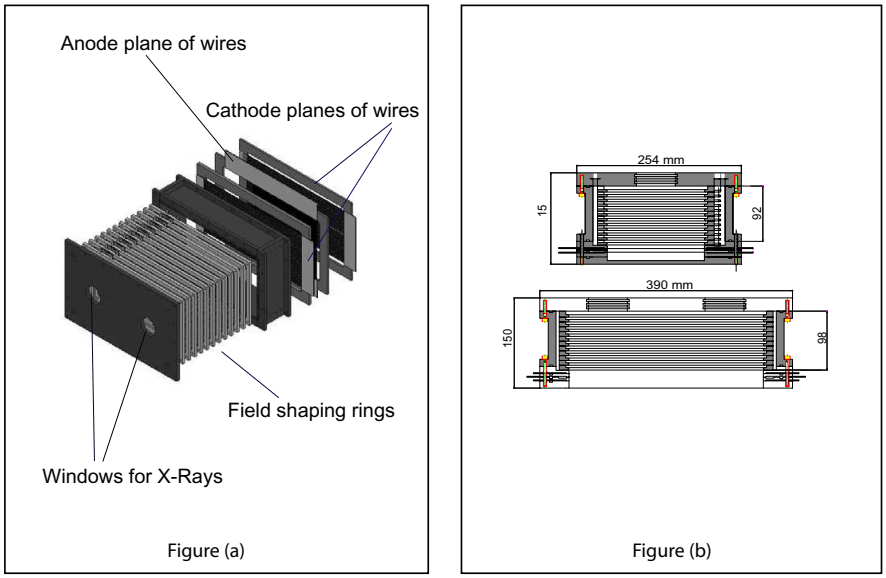

Figure 6.1: *Left: Exploded view of the TPC. The pieces holding the anode and cathode wire planes and the field shaping conductive frames are clearly seen. The holes to hold the circular windows for the X-rays coming out from the magnet bores are present in the front piece. Right: Both side views of the TPC showing the general dimensions in millimeters.*

An optimum performance for the CAST TPC detector would include: low threshold, a relatively high gain, position sensitivity, good efficiency for the energies of interest, low background at low energies, and last but not least, robust and stable operation over the long data taking periods needed to accumulate enough statistics.

6.1 Chamber Description

The CAST TPC, as it appears in *figure 6.1*, has a conversion volume of $10 \times 15 \times 30\,\mathrm{cm}^3$. The 10 cm drift direction is parallel to the magnet beam pipes, and the section of $15 \times 30\,\mathrm{cm}^2$ is perpendicular to that direction. The conversion volume above mentioned, uses Ar(95%)-CH_4(5%) gas at atmospheric pressure in order to produce conversion of photons crossing the chamber.

Covering both magnet bores, the drift electrode, distant 10 cm from the sense wires, is a continuous aluminum layer located on the inner side of the chamber wall closer to the magnet. Except for the electrodes, the screws, the Printed Circuit Board (PCB) and the windows, the entire chamber is made of 17 mm thick low radioactivity plexiglass.

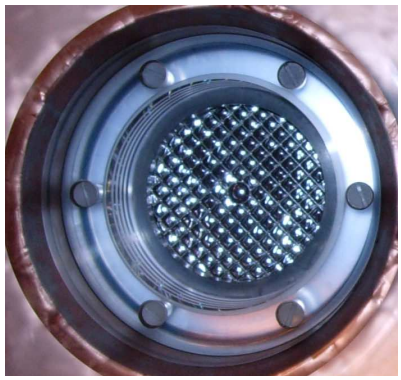

Figure 6.2: *Aluminized mylar window used by the TPC.*

Facing the magnet, the TPC has two 6 cm radius circular holes for the thin windows that must be as transparent as possible to the X-ray coming through the magnet bores, while being able to hold the large pressure difference of 1 atm between the chamber and the magnet pipes that are under vacuum. These windows are thin mylar-Aluminum foils of 3 or 5 μm stretched, then glued to a metallic grid called strongback on the vacuum side of the foil. This technique allows the thin foil to withstand the large pressure difference.

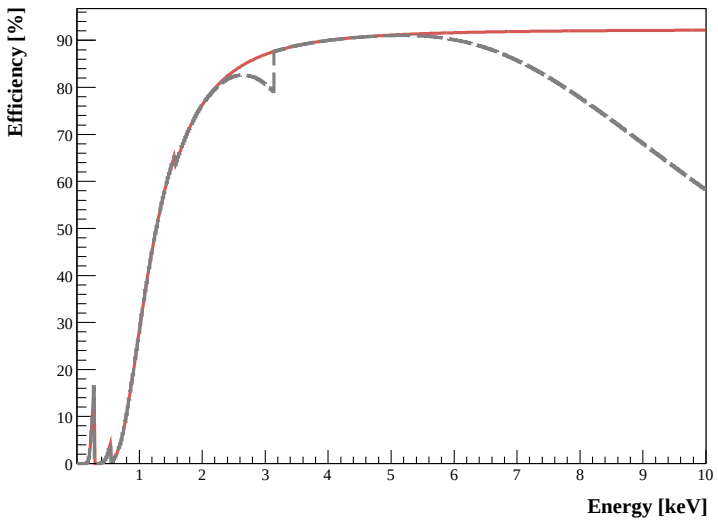

Figure 6.3: *Efficiency for the TPC detector. The red solid line represents the percentage of photons that after going through the windows enter the drift region. The grey dashed line apply the absorption of photons in the Argon-CH_4 gas to calculate the percentage of photons that are deposited in the drift region. The conversion efficiency decreases for higher energies, becoming 50% for photons of 11.5 keV.*

The geometrical opacity of the strongback is about 8% while the mylar foil is practically transparent for X-rays down to the keV energies [72]. The inner side of the mylar foil is aluminized (40 nm) since it serves as part of the drift electrode.

On the other hand, the Argon-CH_4 gas of the TPC is being continuously renewed at a flow rate of $2\,l\,h^{-1}$, in order to prevent any contamination from atmospheric impurities, such as N_2 or O_2.

6.2 Experimental Setup

6.2.1 Data Acquisition Hardware and Software

The first stage of wire signal amplification and shaping is performed by 36 (12 for the anodes and 24 for the cathodes) ALCATEL SMB302 4-channel preamplifier chips, located on the same printed circuit board on which the wires are supported.

Figure 6.4: *Array of 24 ALCATEL SMB302 4-channel preamplifier chips used for the cathode signals of the TPC.*

The output from these preamplifiers is sampled by three 48-channel 10-bit VME flash-ADCs operating at a sampling rate of 10 MHz. These modules are based on the ALTRO (ALICE TPC Read-Out) chip, developed at CERN for the ALICE experiment [73]. The same modules have been used in the HARP and CERES (NA45) experiments at CERN.

The trigger is built from the OR of all the anode signals. The hardware trig-

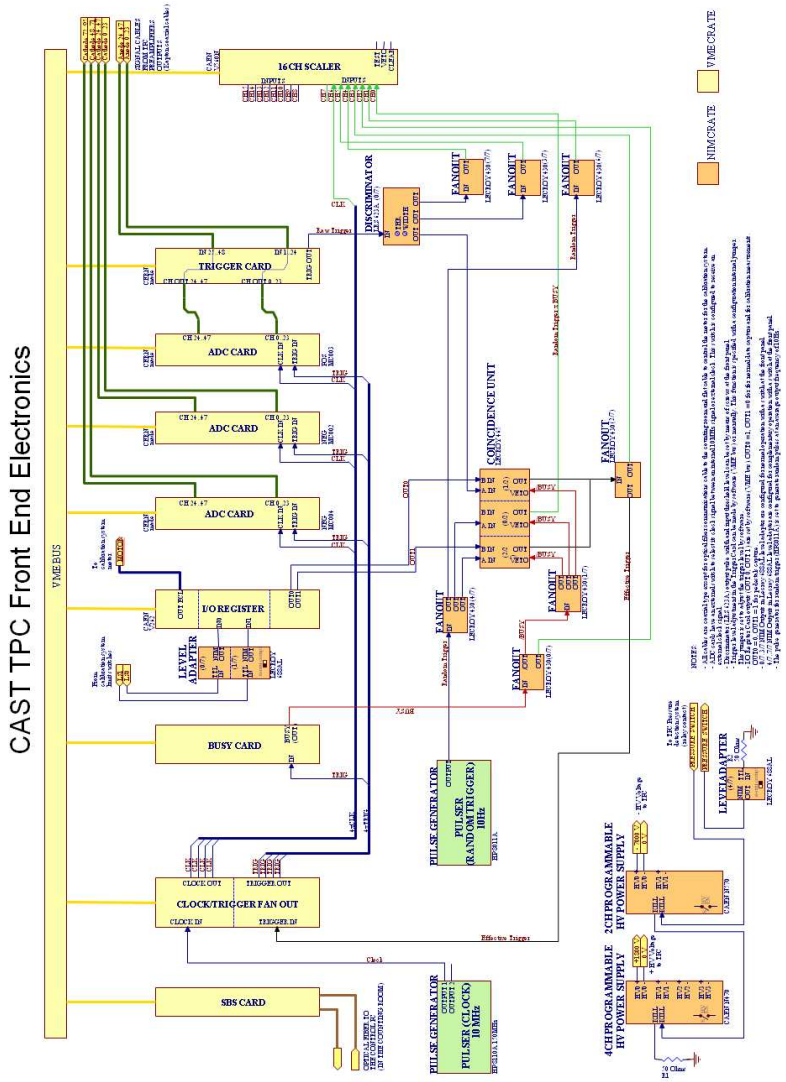

Figure 6.5: *Front End Electronics Scheme for the TPC detector of the CAST experiment.*

ger threshold during normal CAST data-taking operation is set to a safe level that avoids being triggered by electronic noise, and corresponds to energy depositions of about 800 eV in the gas conversion region. The time window for the sampling is about 7 μs, which is long enough to encompass the maximum drift time of the chamber. The flash-ADCs are configured, controlled and read through a VME bus controlled by a dual processor PC running under Linux, which uses a SBS Bit-3 1003 adapter on a fiber-optic link.

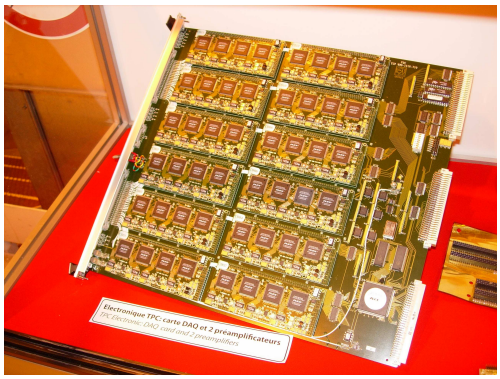

Figure 6.6: *Image of one of the ALTRO cards used by the TPC detector of the CAST experiment.*

The time spent by the system after the trigger arrival in hardware-processing the data, transferring them to the PC and writing them to the disk is, on average, about 1.5 ms, during which it is "blind" to new triggers. This means that for the typical chamber trigger rate of 10 to 25 Hz –depending of data taking conditions– the average dead time can vary from 1.75% to 2.5%. The dead time is continuously monitored by measuring the time the system spends in the "BUSY" state, defined by a hardware register which is set by the trigger and reset to zero by the PC once the event processing is finished. The BUSY logic is handled by a CORBO VME module. The dead time is therefore calculated on-line by using a scaler to count clock pulses both with and without a veto from the BUSY signal provided by the CORBO module.

The acquisition software is a low level C-code which configures, initializes and

controls the electronics modules through the VME bus. Once a trigger is detected, its task is basically to dump the contents of the flash-ADC memories onto the disk, without any further data treatment, so as not to add any dead time. A different, high level C-code for passive monitoring of the detector performance is running continuously in the second processor, without interfering with the acquisition (and therefore without adding noticeable dead time). This software, based on the ROOT toolkit developed for data analysis at CERN [74], monitors online multiple experimental parameters, and therefore allows fast diagnosis of problems and helps in assessing the quality of the data as they are being acquired.

The acquisition of the data follows a fully automatic protocol, and data belonging to Sun-tracking measurements or to background measurements are identified and separated during the off-line analysis.

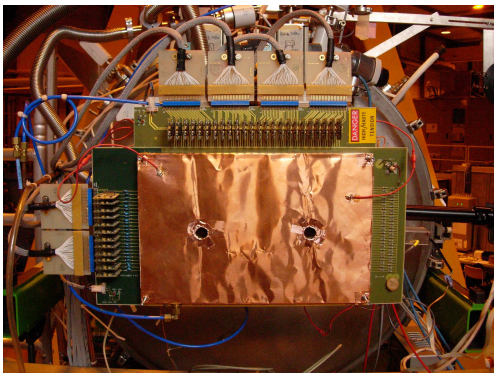

Figure 6.7: *Image of the TPC detector mounted on the CAST magnet.*

The gain of the TPC is measured by using a ^{55}Fe source *(see figure 6.9)* and the pedestal levels and the variation of the flash-ADCs channels are measured using artificial trigger signals in the absence of real events.

As a primary acquisition protocol, the acquisition is automatically stopped

every 5 hours to take a pedestal run and two calibration runs, one through each back window.

The movement of the calibration source from the "shielded" parking position to the corresponding window is performed by a stepping motor, which is fully controllable via ECL or TTL signals. These signals are provided by an input/output register VME module controlled by the acquisition software, so the whole acquisition sequence is fully automated.

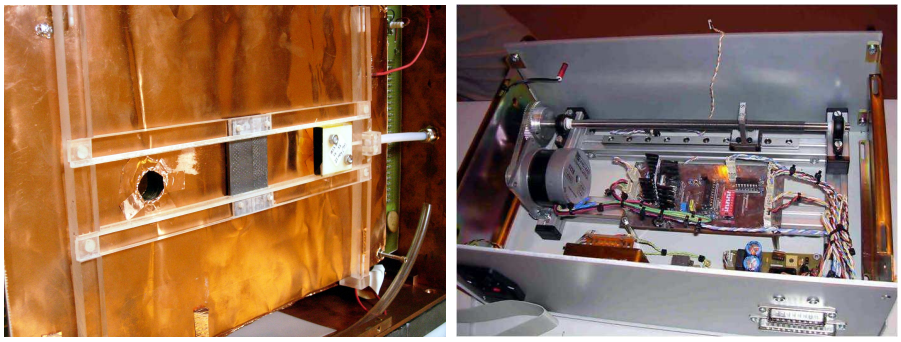

Figure 6.8: *Calibrator of the TPC detector.*

Gain variations of the gas in the chamber are characterized by calibration runs with the ^{55}Fe source every 5 hours as it appears in *figure 6.10*. Therefore, measurements of the gas gain for each window were performed and used to calibrate the flash-ADCs. *Figure 6.11* shows the evolution of the measured gain during the ^{4}He data taking period.

A difference of the gain values for the two windows was observed and this has been taken into account for the data analysis. This difference results from geometrical imperfections in the wire arrangement that produce a gain drift along the anodes. Slight wire-to-wire variations due to mechanical imperfections or adjustments of the preamplifiers were also observed and further corrected by

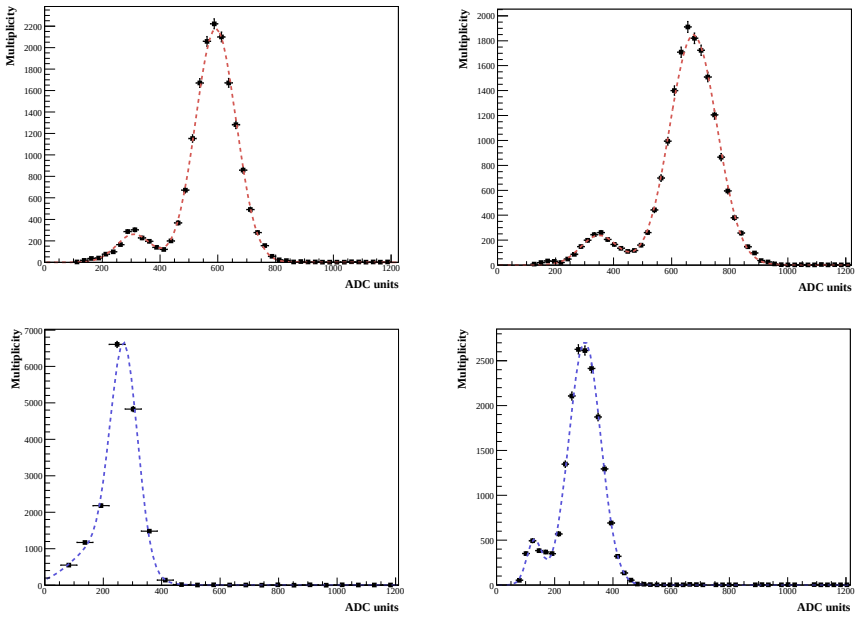

Figure 6.9: *On the left, spectra in ADC units for the collection of charge by the anodes (up) and cathodes (down) on the left window of the TPC detector during the* ^{55}*Fe calibration run number* 11225. *On the right, ADC spectra for the anodes (up) and cathods (down) collection of charge on the right window while the calibration run number* 11226 *with* ^{55}*Fe is taking place.*

maping the gain of every wire independently. The energy spectrum of the events that have passed all cuts is then computed for two distinct classes: the first for all X-ray events collected during the axion-sensitive periods (when the magnet is pointing towards the Sun) and the second for the background spectrum.

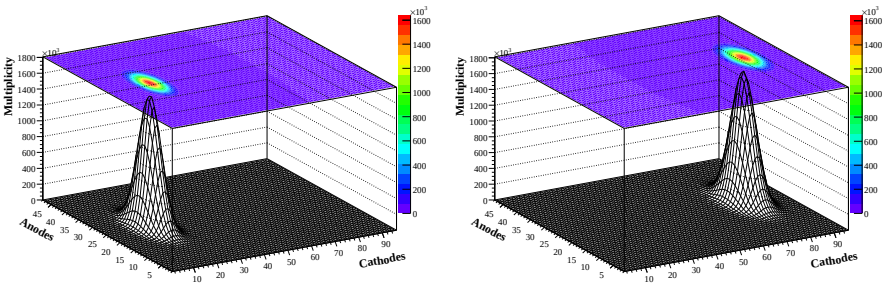

Figure 6.10: *Charge collection and XY positioning for the consequtive calibration runs* 11225 *and* 11226 *with a* ^{55}Fe *source. The calibrations take place in the area of the TPC that is exposed to the magnet bores of the CAST experiment. The center of the circle coincides with the* 25^{th} *anode and for cathodes* 20^{th} *and* 80^{th} *respectively.*

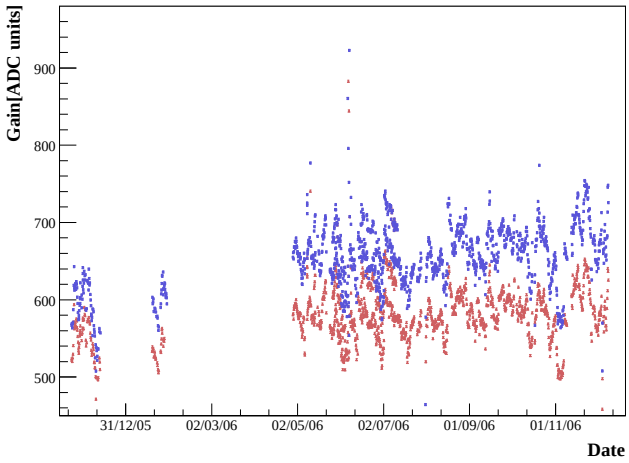

Figure 6.11: *Gain evolution in ADC units for the position of the Mn-K*α *line of an* ^{55}Fe *calibration source placed in the micromega (blue) and CCD (red) windows of the TPC detector.*

6.2.2 The differential pumping

To minimize the effect of the chamber gas leaks towards the magnet, and therefore to cope with the stringent requirements of the magnet vacuum system, a differential pumping system was installed. This system creates an intermediate volume between the TPC and the magnet which is continuously being pumped with a clean pump.

Figure 6.12: *On the left, one holder of the polypropylene window used by the differential pumping system of the TPC detector. The brass pipe is used to connect a vacuum pump to the region between the TPC windows and the differential ones. On the right, the vacuum pump used by the TPC detector in order to generate the differential vacuum.*

This volume is kept at a relatively poor vacuum $\sim 10^{-5}$ mbar, compared with $\sim 10^{-7}$ mbar in the magnet. A second 4 μm thin polypropylene window separates this intermediate volume from the magnet vacuum.

Due to the small pressure difference, the effective leak through this window is extremely small $2.9 \times 10^{-8}\,\mathrm{mbar\,l\,s^{-1}}$ of Argon and $1.3 \times 10^{-9}\,\mathrm{mbar\,l\,s^{-1}}$ of CH_4. Which translates in a factor 690 and 700 respectively to the leaks of the TPC windows $2.0 \times 10^{-5}\,\mathrm{mbar\,l\,s^{-1}}$ of Argon and $9.1 \times 10^{-7}\,\mathrm{mbar\,l\,s^{-1}}$ of CH_4.

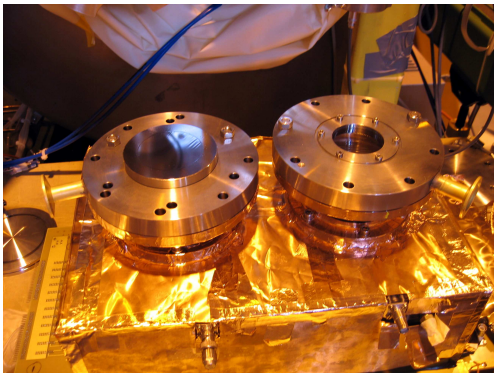

Figure 6.13: *View of the 4 μm polypropylene differential windows installed on top of TPC chimneys.*

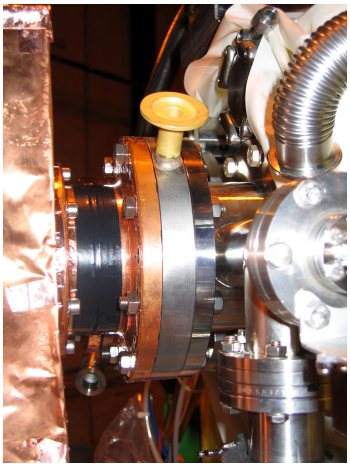

Figure 6.14: *Detailed view of the coupling between the TPC detector and the magnet. One of the differential holder containing a differential window of 4 μm can be seen in the middle of the picture. The brass pipe is the one used for the connection to the vacuum pump.*

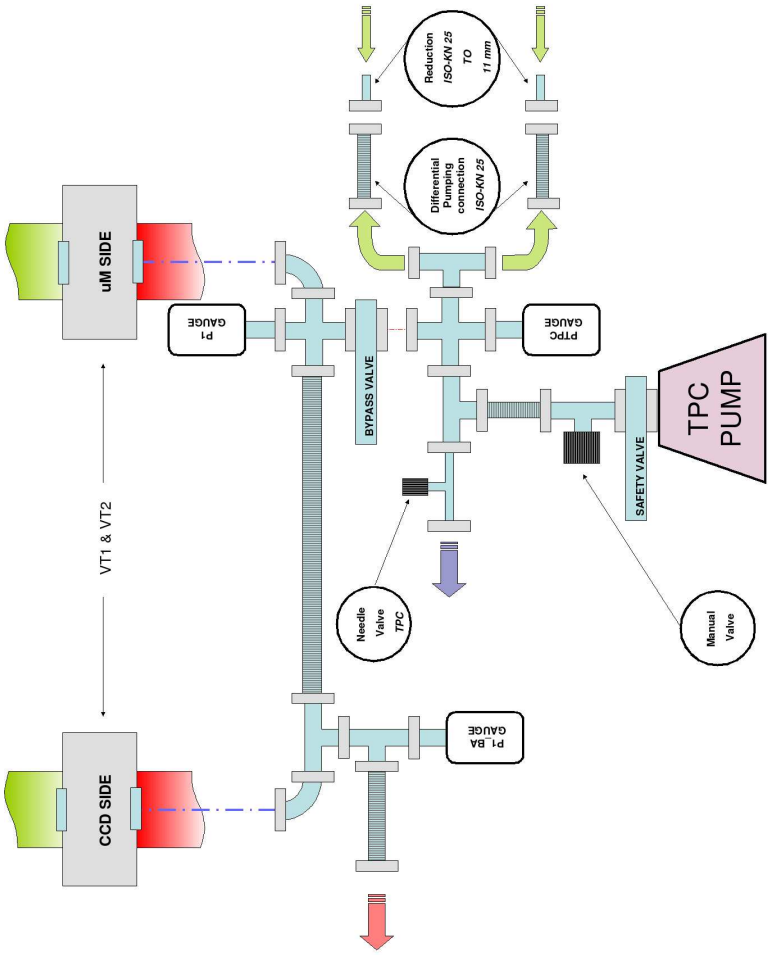

Figure 6.15: *Schematics for the TPC differential pumping system.*

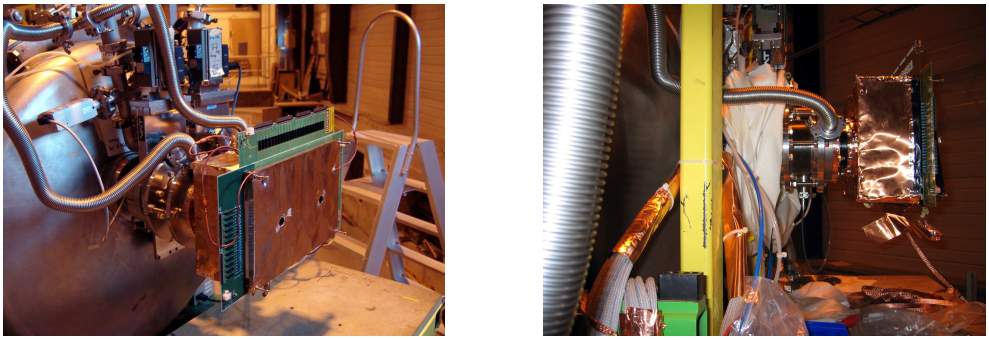

Figure 6.16: *Different views of the TPC detector installed on the CAST magnet. The connections to the pump of the vacuum bellows coming from the differential windows holders can also be seen.*

This strategy allows us to be reasonably tolerant of small leaks on the TPC windows, improving the robustness of the whole system.

6.3 Characterization of the TPC

Properties such efficiency, linearity gain and resolution of the TPC, were measured at the PANTER facility of the Max-Planck-Institut für extraterrestrische Physik (MPE) in Munich in 2002 [75].

The data obtained in this facility have been used to determine the detector response over the whole energy range of interest. The position of the main peak versus energy for each measured PANTER energy point is plotted in *figure 6.17 (left)*, which verifies the linearity of the detector gain. The TPC energy resolution can be also extracted from these data. *Figure 6.17 (right)* shows the resolution in terms of Full Width at Half Maximum (FWHM) versus energy.

These calibration data have been used to determine the efficiency loss in the off-line analysis of the data, in particular the energy dependence of the off-line cuts which are applied to reduce the background.

The illustrated efficiency curve of the detector in *figure 6.18* has been ob-

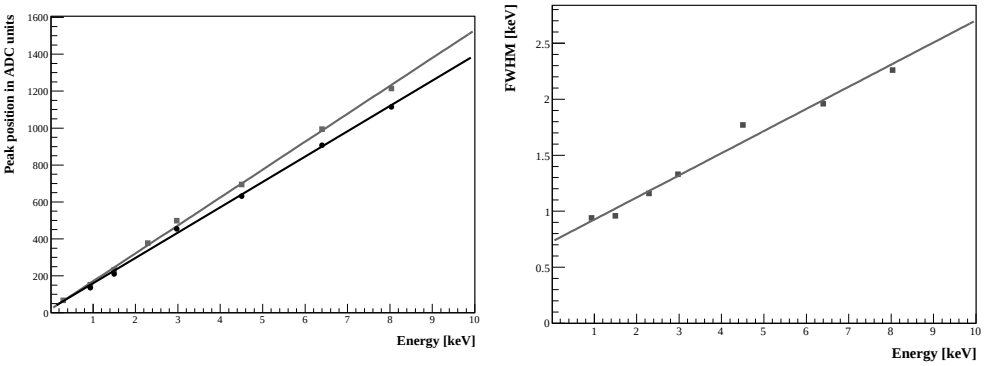

Figure 6.17: *Left: Peak position in arbitrary ADC units versus incident photon energy. The black points and the grey points were taken from two different data sets, showing the variation of the detector gain due to different atmospheric conditions. Right: Measurements of the energy resolution of the TPC detector in terms of full width at half maximum (FWHM) of the photo-peak.*

tained by comparing the counts detected in each corresponding run with the expected rate deduced from the calibrated PANTER detector [62].

The black points of *figure 6.18* correspond to the final off-line analysis, that produces an additional loss of efficiency of about 5 to 10 % depending on the energy of the event.

The green dashed-dotted line is an analytical function used to interpolate the measured efficiencies together with the conditions of data taking that took place during the first phase of the CAST experiment. However, different conditions for data taking during the second phase of the CAST experiment, such the existence of cold windows in the magnet, arise into a loss of efficiency that is represented by the solid blue line in *figure 6.18*.

The main implication of efficiency losses is the non observation of axions arriving the Earth. By multiplying the obtained efficiency of the CAST TPC detector during phase one with the expected solaraxion spectrum, we obtain

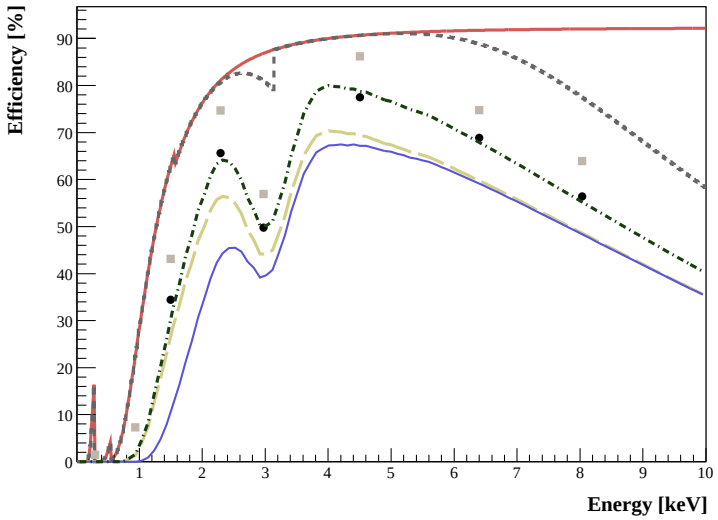

Figure 6.18: *Experimental measurements of the TPC effciency, before (grey squares) and after (black points) the off-line analysis cuts are applied to the data. The upper red line represents the theoretical computation of the TPC window transmission, while the dark grey dashed line includes also the opacity of the gas in the chamber. The green dashed-dotted line is the analytical function used to interpolate the experimental points in the final analysis of the phase one of the CAST experiment, while the solid blue line is used for the analysis of the second phase of CAST. The yellow dashed line is the effect that the strongback of the cold windows has on the efficiency used during the first phase.*

an overall detection efficiency of 62 % for photons coming from conversion of solar axions, while if we do the same for the second phase of the CAST experiment, the overall efficiency becomes a 48 %.

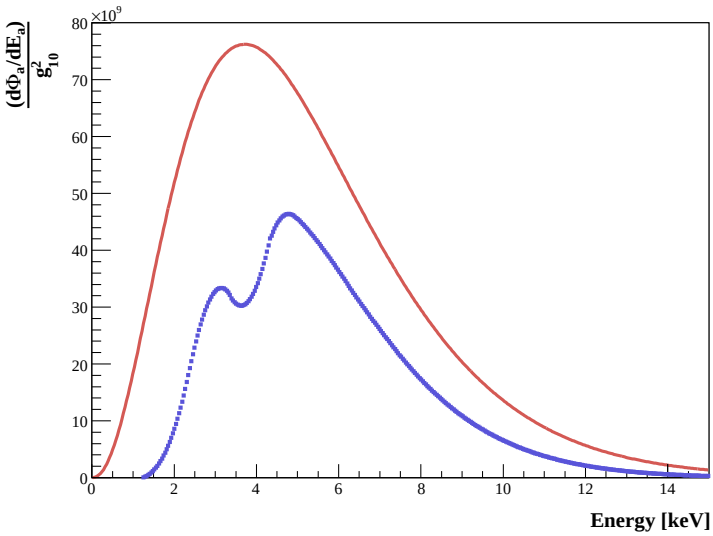

Figure 6.19: *Axion flux on Earth (red line) and its convolution with the efficiency of the TPC during the Second Phase of the CAST experiment (blue dots) .*

6.4 Off-line analysis

The first level data treatment of the CAST TPC is focused on the identification of the almost point-like energy depositions produced by the low energy X-ray in the conversion volume of the chamber. The very characteristic profile of a X-ray event provides the framework for a selective analysis.

A first characterization of these raw data generated by the flash-ADCs is performed depending on the spread of the signal. X-ray of the energies of interest in our chamber normally produce a single-cluster[1] event firing between 1 and 3 anode wires and between 2 and 8 cathode wires with a time difference between

[1] A "cluster" is a set of charge pulses or hits gathered on several contiguous anode wires as well as on several contiguous cathode wires. For analysis purposes we distinguish clusters of anode hits and clusters of cathode hits separately. Obviously, events containing one single physical cluster must contain one anode cluster and one cathode cluster.

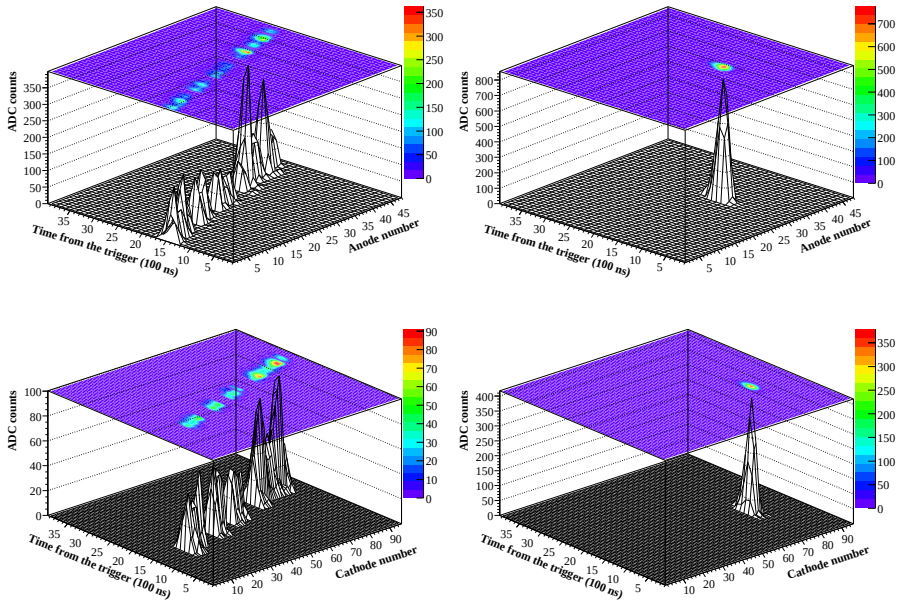

Figure 6.20: *Time evolution of the charge pulse generated in each wire as recorded by the flash-ADCs. Top (bottom) plots correspond to what is collected in the anode (cathode) wires. On the left a background event is plotted, while on the right a X-ray like event is shown.*

contiguous hits less than 50 ns *(see figure 6.20)*.

The spread of the anode signal is mainly due to the diffusion of the electron cloud along the drift distance and higher energy desposits give larger initial ionization clouds. The CAST TPC drift is set to an effective voltage of $0.7\,\mathrm{kV\,cm^{-1}}$, voltage that is applied between the drift electrode that hold the TPC windows towards the magnet and the anode plane that is grounded. The avalanche region is forced to happen between the cathode wires that is located at 3 mm distance from the anode plane and the effective voltage applied is $6.1\,\mathrm{kV\,cm^{-1}}$. The larger spread that the cathode wires sense is due to the development of the avalanche process along the anode wires.

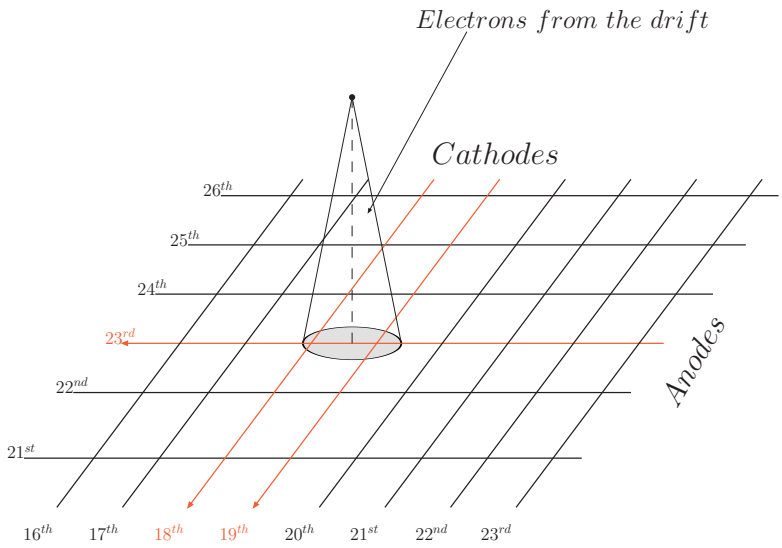

Figure 6.21: *Representation of a cluster event for the anode* 23^{rd} *and cathodes* 18^{th} *and* 19^{th}*. The energy deposit in the anodes is the charge collected by anode* 23^{rd}*, while for the cathodes, the enregy will be the adition of charges collected by the cathodes* 18^{th} *and* 19^{th}*. The position of the event is determinated in the plane* $XY \equiv \text{Anode} - \text{Cathode}$ *by weighting the charge collected in each of one of the wires (hits) with the total charge of the cluster.*

In addition, to be considered as a cluster, the total charge must exceed a minimum charge threshold. This is done to avoid the improbable effect of correlated noise in contiguous wires producing spurious clusters that would affect the efficiency. Therefore, the entire information for one raw data event can now be reduced to a small set of numerical parameters, including:

- Number of clusters in the event and whether they are in the anode or cathode wire plane. This number provides information on the signal spread.
- Multiplicity of every cluster, i.e., number of hits comprising the cluster.

- Total cluster charge calculated by adding up the charge of every hit comprising the cluster.
- Cluster position calculated by the charge-weighted mean of the position (wire number) of every hit comprising the cluster.
- Cluster time (related to the trigger) calculated by the charge-weighted mean of the times of every hit composing the cluster.

Next, a set of software cuts are applied to reject events that are clearly not produced by X-ray interactions. The first and most important one is the requirement that there is one single anode cluster and one single cathode cluster. It is then straightforward to match both of them to get the 2-dimensional position of the point-like event.

A detailed list of further conditions required on the cluster properties is given in *table 6.1*.

cut	**condition**
anode multiplicity	number of anode hits between 1 and 3 (both inclusive)
cathode multiplicity	number of cathode hits between 2 and 8 (both inclusive)
anode–cathode time difference	time between anode and cathode cluster in the range -0.15 to $0.02\,\mu$s
no saturation	no hit reaching the upper part of the flash-ADC dynamical range
anode–cathode charge ratio	around 1.85, but slightly energy dependent
fiducial cut	only events whose 2-D coordinates are inside the windows facing the magnet bores

Table 6.1: *List of software cuts applied to the CAST TPC data.*

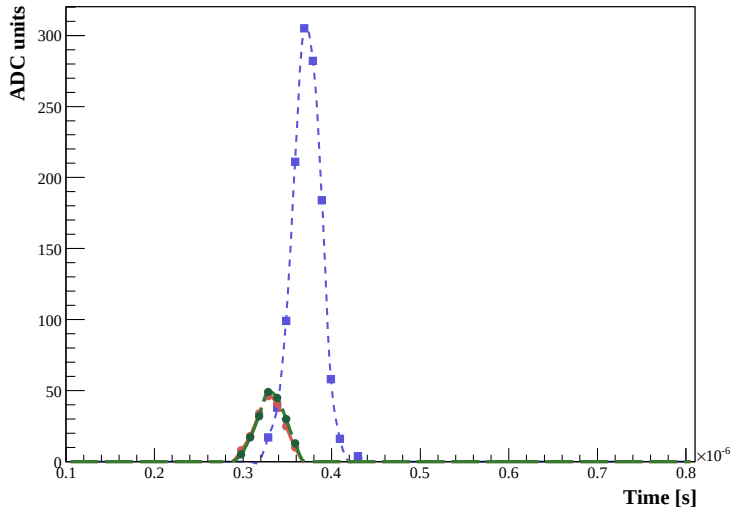

Figure 6.22: *Example of a cluster produced by an X-ray of* 3 keV *in the TPC detector. The dashed blue dots are the samples for the* 23^{rd} *anode, while in red and green the samples for the cathodes* 18^{th} *and* 19^{th} *respectively. All the signals together allow the positioning of the event in the XY plane of the detector and the energy of the event is proportional to the height of the pulses.*

This set of cuts is a minimal choice designed to reject a large portion of background events while minimally reducing the efficiency of the detector. Typically its application reduces the background by approximately two orders of magnitude with respect to the raw trigger rate. The loss of efficiency generated by the software cuts has been carefully measured using the PANTER data as described above, in particular regarding the loss of X-rays events with split energy deposition (2 or more cluster events) due to the argon escape peak.

The cluster energy is obtained by adding up the calibrated flash-ADC output for every constituent hit *(see figure 6.22)*.

6.5 Background sources

The X-ray signal produced by the axions inside the magnet has a maximum expectation value at 4 keV and vanishes at around 10 keV. However, these signals could be masked by the inhomogeneous background of materials in the experimental site.

The main source of background is expected to be gamma rays produced predominantly in the radioactive chains of ^{238}U, ^{232}Th and in the ^{40}K isotope decays. Their interactions with the materials near the detector can generate low energy photons via the Compton effect and also X-ray. Neutrons produced by fission and (α,n) processes as well as those induced by muons and cosmic rays are also sources of background for the TPC detector [61, 65].

6.5.1 Experimental site and background

The CAST experiment is located at one of the buildings of the SR8 experimental area at CERN.

The floor and lower part of the walls around are made of concrete, while the materials for the upper part of the walls can be quite different. Thin metal plates in the upper North wall and concrete for East and South walls with 11 cm thick metal pillars distributed every approximately 2.5 m all around the area form the building 2875 in which CAST is located *(see figure 6.23)*.

The inhomogeneity of the building materials led us to undertake a careful study of the radioactive background and a detailed analysis of the measured TPC background data.

Gamma background The experimental site contributes to an important, and non-uniform, gamma background owing to radioactive contamination. Gamma spectrometry measurements performed with an hyper pure germanium gamma spectrometer in a range from 50 keV to 3 MeV confirmed the radioactive chains and potassium as the main sources for background *(see Table 6.2)*.

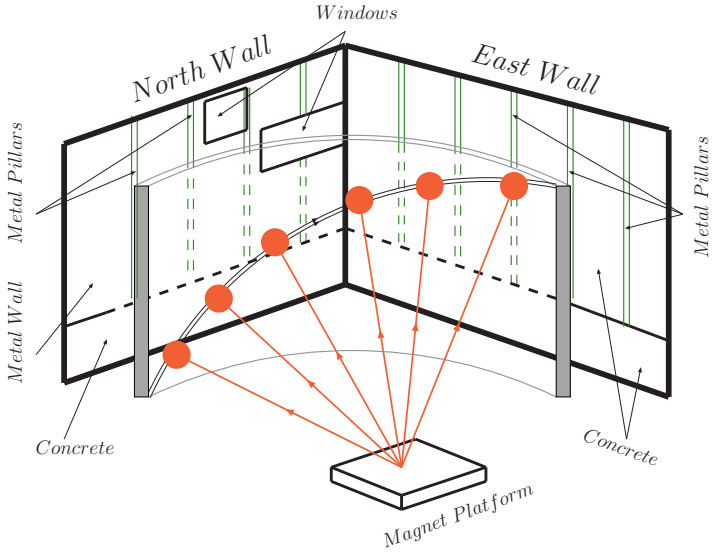

Figure 6.23: *Schematic of the TPC detector environment and its path facing the North and East walls while tracking.*

The background disparity between the different walls of the CAST experiment leads to differences in the emanation rates that can go from 10 to 100 counts $\mathrm{cm}^{-2}\,\mathrm{s}^{-1}$ depending on the wall *(see Table 6.2)*.

These data pointed also to a radon emanation for the east and south walls.

Materials like steel, plastics and metals (i.e. Fe, C, H, Cu, ...) used for the construction of the CAST telescope may be also considered within this category. Its presence in the magnet girder and surroundings may contribute to the gamma contamination detected by the TPC.

Neutrons and protons coming from cosmic rays can also induce radioisotopes in the detector gas and materials. From them, mainly the isotopes $^{14}\mathrm{C}$ and $^{3}\mathrm{H}$, whose contribution can be neglected owing to their low production rate ~ 0.003 nuclei of $^{14}\mathrm{C}$ and ~ 0.001 nuclei of $^{3}\mathrm{H}$ per litre and day in the Ar-CH_4 gas

Wall description	^{238}U chain ^{238}U→^{226}Ra	^{218}Po→^{210}Po	^{235}U chain	^{232}Th chain	^{40}K
North and lower East	25 ± 2		1.1 ± 0.7	10 ± 2	113 ± 10
South and upper East	923±274	32±5	40±12	34 ± 6	388 ± 45

Table 6.2: *Mean gamma production in the CAST site* [Bq/kg]. *For the radioactive chains, equilibrium activities are quoted. In the case of radon emanation from the ^{238}U chain, equilibrium is broken and activities for the nuclides before and after ^{222}Rn are given separately.*

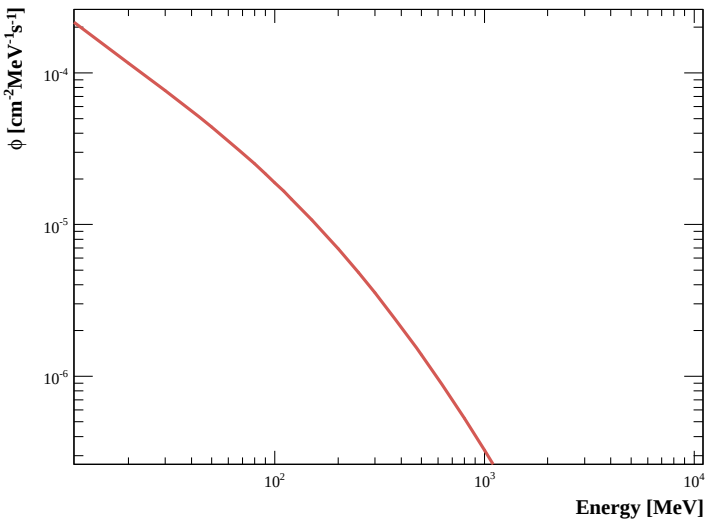

Figure 6.24: *Environmental sea level background spectrum of cosmic neutrons [66].*

used by the TPC detector [65]. Another gamma contribution corresponds to the cosmic ray photon flux, being only a small fraction ($\leq 1\%$) of the total [69].

Most of the gamma radiation described above would traverse the active volume of the detector without interacting at all. However, the presence of energetic gammas in the surrounding of the detector may create secondary photons able to contribute significantly to the background signal of the TPC.

Neutron background Quantitative measurements of neutron background have been performed in the experimental site with a BF_3 detector. The homogeneous measured flux of neutrons in the CAST site is around $3{\times}10^{-2}\,\mathrm{n\,cm^{-2}\,s^{-1}}$. This value, and its homogeneity, points to a cosmic source. Cosmic ray generated neutrons have energies below a few GeV and the spectrum shows a dependence as $1/\mathrm{E}^{0.88}$ up to 50 MeV and as $1/\mathrm{E}$ above this energy [70]. This is the most important neutron contribution, not only for its intensity but also for its high energy.

Other sources of neutron background are neutrons induced by cosmic muons in the surrounding materials, (α, n) reactions on light elements and the spontaneous fission from nuclides like ^{238}U, ^{235}U and ^{232}Th.

Cosmic	Muon induced	Fission	(α, n)
$\sim 10^{-2}$	$\sim 10^{-3}$	$\sim 10^{-5}$	$\sim 10^{-5}$

Table 6.3: *Comparison of the estimated order of magnitude for neutrons coming from different sources. Values are given in neutrons per cm^2 and second.*

6.6 The shielding of the CAST TPC detector

The TPC has been designed to reduce the background in a complementary way to the effect of the off-line software cuts [62] as we have mentioned in *Section 6.5*.

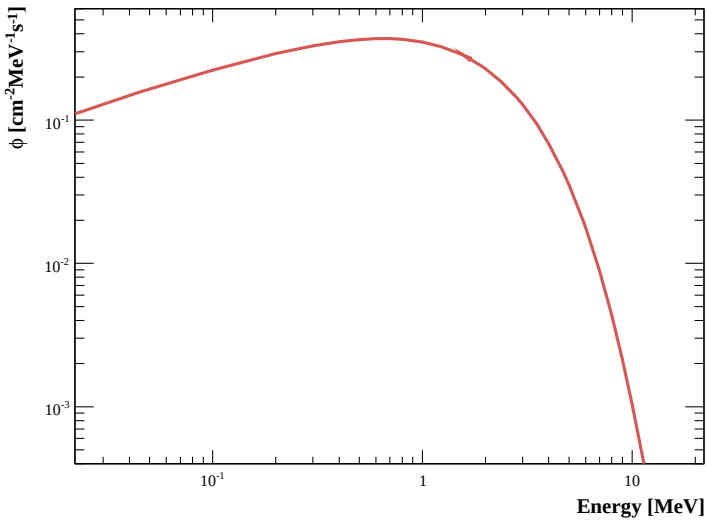

Figure 6.25: *Spectrum of neutrons coming from fission [67].*

The main goal of the shielding is to reduce the background levels coming from external sources and decrease the background spatial inhomogeneity observed in the experimental site. Its final configuration is a compromise among the shielding effect and the CAST technical limitations such as weight and size restrictions imposed by the experimental moving structure.

From the outside to the TPC detector, the CAST TPC shielding *(see figure 6.26)* is composed of:

i) A PVC bag which covers the whole shielding assembly. This tightly closes the entire set-up allowing to flush the inner part with pure N_2 gas coming from liquid nitrogen evaporation in order to purge this space of radon.

ii) Polyethylene pieces, 22.5 cm thick, used to slow the medium energy envi-

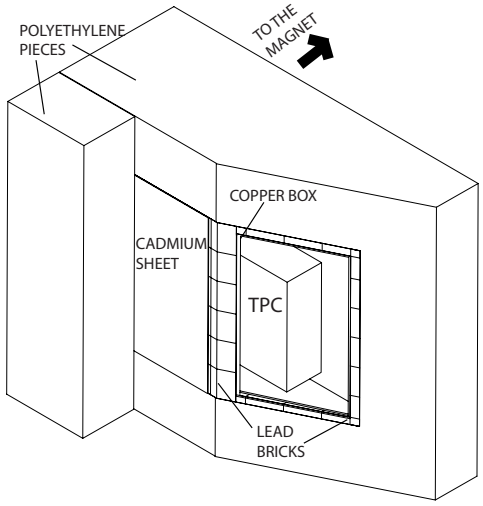

Figure 6.26: *Schemematic of the TPC shielding in order to show the 3D arrangement of the whole structure.*

ronmental neutrons down to thermal energies. It also reduces the gamma contamination and helps the mechanical stability of the whole structure.

iii) A cadmium layer, 1 mm thick, to absorb the thermal neutrons slowed down by the outer polyethylene wall.

iv) Lead bricks, 2.5 cm thick, which reduces the low and medium energy environmental gamma radiation.

v) A copper box, 5 mm thick. This Faraday cage reduces the electronic noise and stops low energy X-rays produced in the outer part of the shielding by environmental gamma radiation. It is also used for mechanical support purposes.

vi) Plexiglass, 17 mm thick: not really part of the shielding but the wall of the TPC vessel itself. X-ray fluorescence from the copper would be stopped by this layer.

The described scheme is the outcome of several simulations and experimental tests.

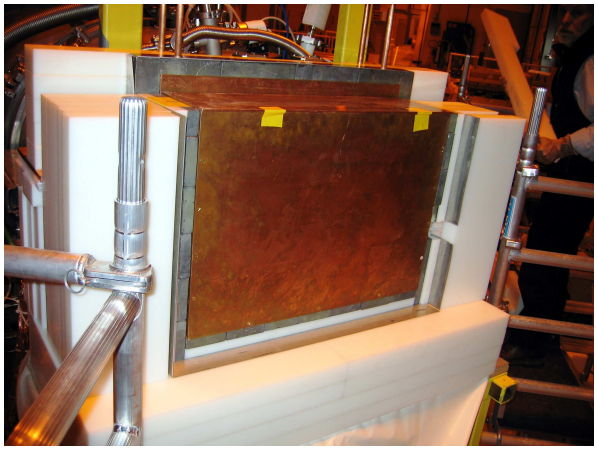

Figure 6.27: *TPC installation on the CAST experiment. In white the polyethylene pieces of the TPC shielding surrounding not only the detector, but also the cadmium, lead and copper of shielding.*

6.6.1 Monte Carlo simulations

In order to estimate the external background contribution to the TPC detector, Monte Carlo simulations with the GEANT4 toolkit [71] have reproduced the TPC detector and its shielding.

To discriminate the expected X-ray signal, the cluster criteria has been also implemented. Its application to the GEANT4 simulated data implies a reduction of the registered events by two orders of magnitude, which is in good agreement with the experimental data.

We will focus on gamma simulations since this is the main contribution to the TPC background. Three different shielding configurations have been com-

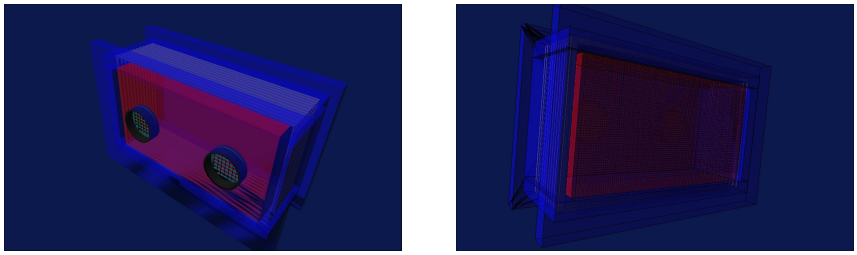

Figure 6.28: *Recreation of the front side of the TPC detector with the GEANT4 toolkit on the left. On the right an image of the backside of the TPC detector with the anode-cathode wire planes. In blue, the plexiglass used for the construction of the detector. The* $Ar - CH_4$ *gas in which X-ray photons may deposit energy and be detected appears in red. It can also be seen the two mylar-aluminum windows with strongback that face the magnet bores through which the signals from axions may appear. On the right, the backside of the TPC detector with the anode-cathode wire planes. The reconstruction of the TPC detector with the GEANT4 toolkit include as well the field shaper rings in grey.*

pared: a 5 mm-thick copper box, the copperbox plus 2.5 cm of lead, and a complete shielding consisting of 5 mm-thick copper box plus 2.5 cm of lead plus 22.5 cm of polyethylene.

Simulations for external gamma Primary events, corresponding to the radioactive chains and potassium, have been generated uniformly and isotropically on a sphere surrounding the external surface of different shielding configurations.

The shielding made of 5 mm of copper plus 2.5 cm of lead plus 22.5 cm of polyethylene reduces the external gamma background by more than one order of magnitude, (92±3)% in the 3-7 keV range.

Since the thick layer of polyethylene helps in the gamma attenuation, the same shielding without polyethylene is about a 15% less effective, causing an estimated reduction of (77±4)%.

Compton interactions in the polyethylene result in lower energy photons which

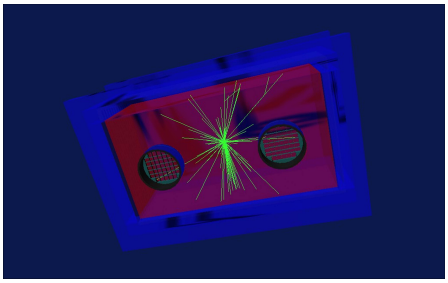

Figure 6.29: *Simulation with GEANT4 of a calibration done with a ^{55}Fe source situated inside the TPC detector. The green lines represent the free path of the X-ray photons from the source in the $Ar - CH_4$ gas.*

are easily absorbed in the lead. Though a thicker layer of lead could stop a larger fraction of the external gammas, it can be a source of secondary neutrons and it would add too much weight to one of the ends of the magnet.

Due to the spatial inhomogeneity of the gamma background coming from walls, simulations allow us to make just a rough estimate of the TPC recorded counts. These external photons cause between 30 and 55 counts per hour in the volume of the detector facing the two windows for the $3 - 7\,\mathrm{keV}$ energy region in the case of the copper shielding (2003 data taking configuration). In the case of a complete shielding, 2004 and second phase configuration, the GEANT4 simulations give between 2 and 5 counts per hour.

The GEANT4 package has also been used to simulate the effect of the radon trapped inside the copper box [65].

Neutron simulations Though neutrons interacting in materials can produce γ particles, more neutrons, α particles and fission fragments depending on materials and energies, the most efficient reaction is the elastic scattering, energy transferred to nuclear recoils (E_R). This energy is determined by the energy of the incident neutron (E_n) and the scattering angle θ:

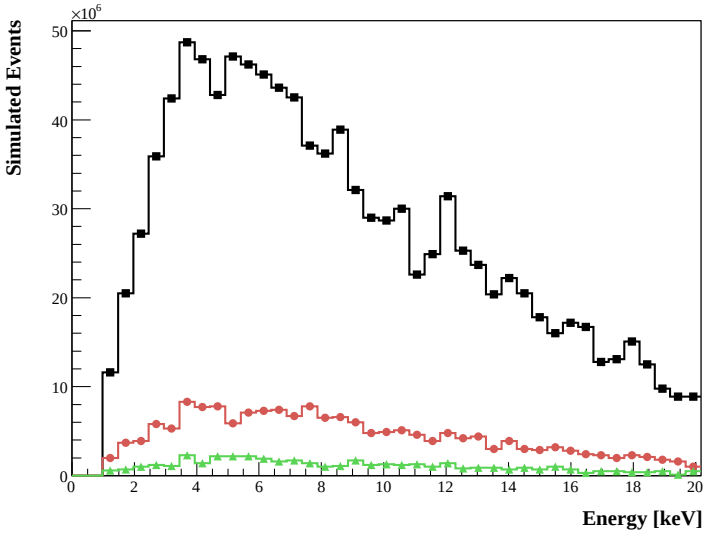

Figure 6.30: *GEANT4 simulated spectra of the TPC for an isotropically distributed sphere of* ^{40}K *arround the different shielding setups for the TPC. In black the spectra resulting from using a copper box of* 5 mm *as shielding for the TPC detector. The red spectra shows the effect of adding* 2.5 cm *lead to the copper shielding (*84 % *of reduction), while in green can be observed the effect of a complete shielding composed of* 5 mm *copper,* 2.5 cm *lead,* 1 mm *cadmium and* 22.5 cm *polyethylene (*96 % *of reduction).*

$$E_R = \frac{4A}{(1+A)^2}(\cos^2\theta)\cdot E_n. \tag{6.1}$$

In the case of argon, $A = 40$, assuming a quenching factor of 0.28, the maximum visible energy and the neutron energy are related as follows:

$$E_{R,max} = 0.0266 \cdot E_n. \tag{6.2}$$

Therefore, the neutrons able to deposit a visible energy in the analysed range of 3–7 keV are mostly those with an energy between 0.11 and 0.27 MeV.

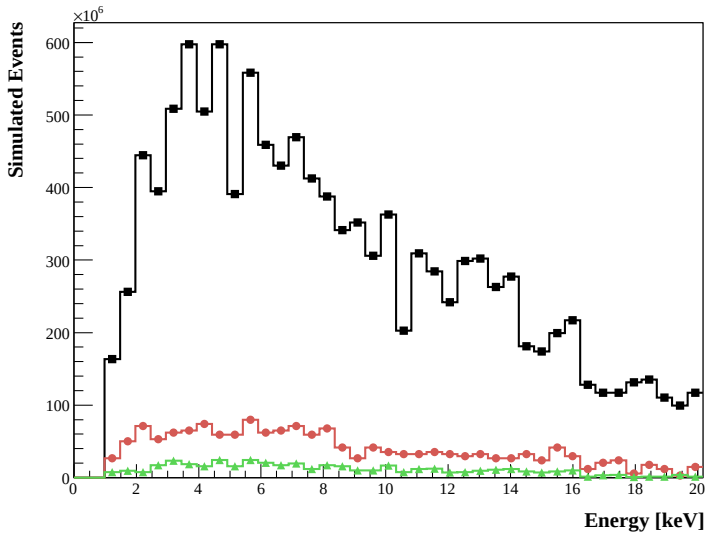

Figure 6.31: *Spectra obtained from the GEANT4 simulation of an isotropically distributed sphere of* ^{238}U *arround a copper box of* 5 mm *covering the TPC detector (black). The red spectra shows the improvement of adding* 2.5 cm *lead reffered to the copper shielding (*87 % *of reduction). In green the effect of a complete shielding composed of* 5 mm *copper,* 2.5 cm *lead,* 1 mm *cadmium and* 22.5 cm *polyethylene for the TPC detector (*96 % *of reduction).*

Using a real cosmic spectrum as input and the G4NDL3.5 neutron data library, a GEANT4 simulation has allowed us to roughly estimate about 2 counts per hour caused by cosmic neutrons inside the two windows of the TPC in the $(3-7)$ keV visible energy region in the case of the copper shielding.

To understand the effects of the different layers of shielding FLUKA code [65] shows the effects of every layer of shielding material on cosmic neutrons: while polyethylene decreases the number of background neutrons per cosmic neutron, the 2.5 cm of lead increases this number due to $(n, 2n)$ processes *(see figure 6.33)*. Cadmium absorbs thermal and epithermal neutrons with energies below 1keV.

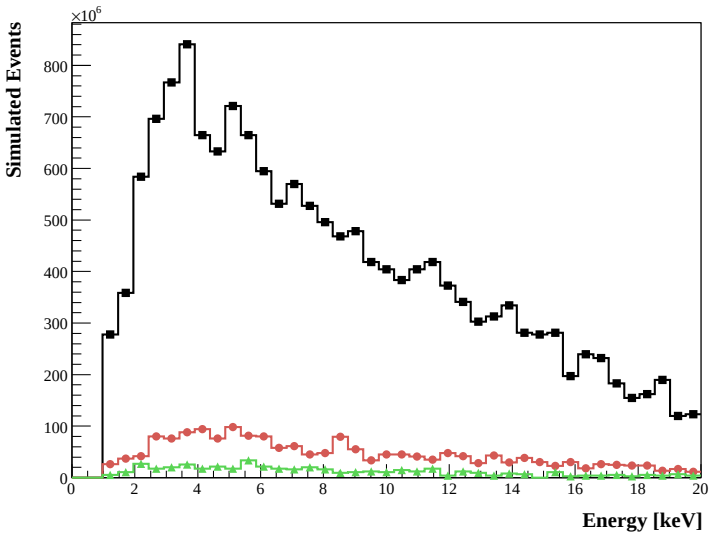

Figure 6.32: *Spectra for a* ^{232}*Th source isotropically distributed around the different shielding configurations. In black the spectra resulting from using a copper box of* 5 mm*. The red spectra shows the effect of adding* 2.5 cm *lead to the copper shielding (*88 % *of reduction), while in green can be observed the effect of a complete shielding composed of* 5 mm *copper,* 2.5 cm *lead,* 1 mm *cadmium and* 22.5 cm *polyethylene (*97 % *of reduction).*

The shielding without polyethylene has been also compared to the complete configuration. The number of cosmic neutrons able to produce nuclear recoils and a deposit of visible energy in the TPC in the $3 - 7\,\mathrm{keV}$ range decreases by only 20% after the complete shielding due to the production of neutrons in lead. The number of neutrons could even increase by 10% if the 22.5 cm of polyethylene are taken off.

The neutron production in the shielding due to muons has also been investigated. Most of these neutrons are produced in lead, but its contribution is three orders of magnitude smaller than the measured background rates [65].

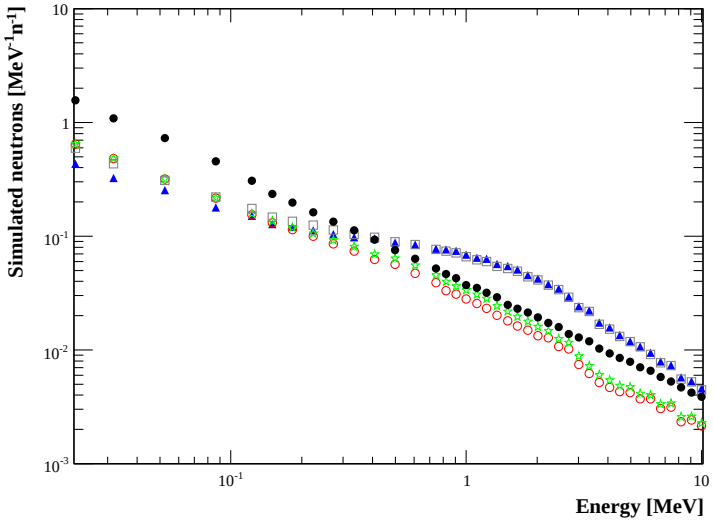

Figure 6.33: *Cosmic neutrons in the 10 keV-20 MeV range after traversing every layer of shielding: incoming cosmic neutrons (black solid circles), neutrons after traversing 22.5 cm of polyethylene (open red circles) plus 1 mm of cadmium (green stars) plus 2.5 cm of lead (open grey squares) plus 5 mm of copper (solid blue triangles). Spectra are normalised to one cosmic neutron.*

6.6.2 TPC background data

First tests of the full shielding showed a reduction factor of ~ 8 below the background level of the chamber. Howewer, this test were made not in the CAST experimental area but in the laboratory and with a lead shielding of 5 cm.

Once the detector was mounted in the magnet, this factor became smaller. Different shielding setups based on the studies and simulations showed in *Section 6.6.1* were investigated at the CAST experimental site to observe the effects of every component of the shielding. The measurements were carried out with and without nitrogen flush at the same spatial position and one right after the other to avoid time variations.

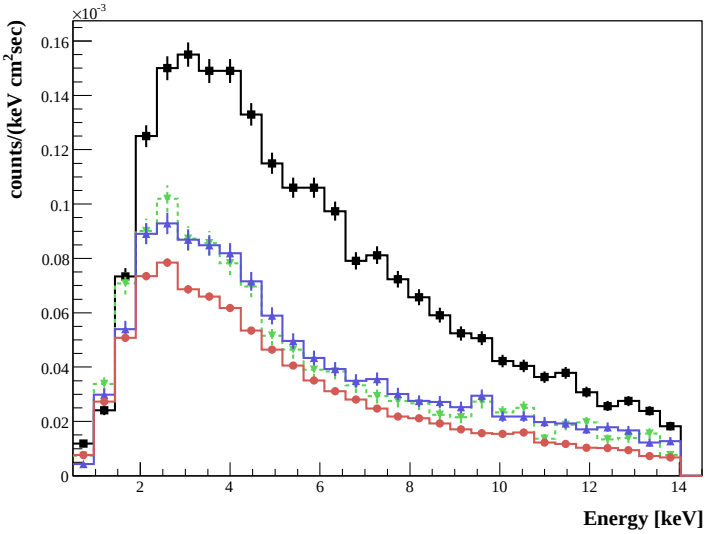

Figure 6.34: *Background data obtained in the shielding test at the experimental site for different shielding configurations: full shielding set-up (red bottom line), the copper box plus* 2.5 cm *of lead (solid blue line in the middle), the copper box plus a double layer of lead (dotted green line in the middle) and just the copper box (black line).*

A full shielding composed of copper, lead, cadmium and polyethylene reduces background levels by a factor of ~ 3 in the $3 - 7\,\mathrm{keV}$ energy interval.

Finally, we can also compare the experimental background data during the installation of the TPC for the second phase of the CAST experiment.

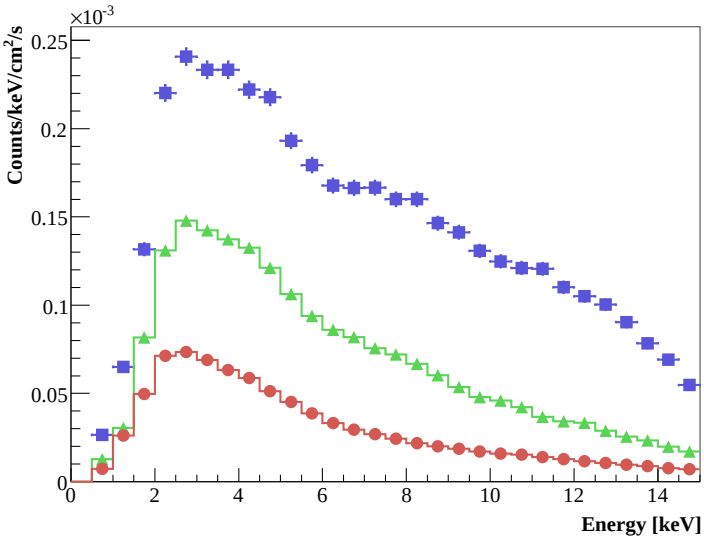

Figure 6.35: *Background data obtained during the installation of the TPC detector for the second phase of the CAST experiment. The blue squares represent the raw background of the TPC detector (no shielding). The green triangles are the backgroun spectrum of the TPC once the* 5 mm *copper box is installed and the nitrogen flux is operative . The red dots is the final achievement of the TPC detector background once the full shielding is installed.*

During the different data taking periods, the TPC detector has recorded background data at any other position. The best control of the background is the study of its inhomogeneity. The *figure 6.36* shows measured background levels for nine positions: the three first measurement points are facing the North wall; the three next points face the NE corner and the last one faces the East wall near one of the metal pillars.

Prior to the installation of the full shielding for the TPC, during the year 2003, the TPC was covered by a 5 mm thick copper box and a nitrogen flush

inside. The background measurements showed a high degree of inhomogeneity as it can be observed in *figure 6.36*. The implementation of the full shielding for the TPC detector have achieved both, a fairly homogeneous background among the different positions of the TPC in the CAST experiment and a factor ~ 4 of reduction in the 1 to 10 keV energy range.

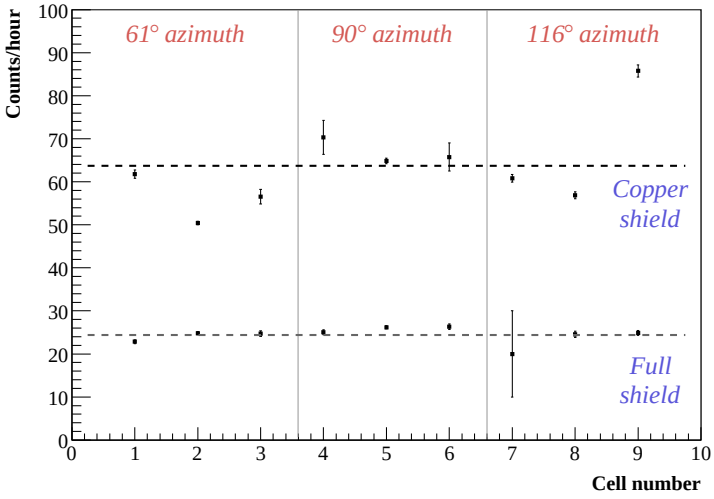

Figure 6.36: *July-August background data obtained during 2003 with the TPC covered by a copper box flushed with Nitrogen (squares). The circles correspond to the data obtained during the Second Phase of CAST once the TPC had the full shielding installed. Measurements corresponds to 3 vertical positions and 3 horizontal positions of the TPC detector. The 9 magnet positions run first vertically and then horizontally.*

Part III

The analysis of the TPC data

Chapter 7

Solar axions for the TPC detector

The description of the CAST experiment and the TPC detector in the previous chapters allow us to implement the axion theory to the data taken by the TPC during the ^{4}He Phase of the CAST experiment. This chapter explains how the axion theory is applied to the TPC of CAST.

7.1 Pressure settings

During the Second Phase of CAST, the different pressure settings of ^{4}He have been able to restore the coherence of the axion-to-photon Primakoff conversion for axions whose masses were up to 0.39 eV. *Section 4.3.1* directly relates the ^{4}He pressure of CAST's cold bore with the effective mass of the photon arising from the conversion via Primakoff effect.

According to the specific conditions of pressure and temperature of the ^{4}He, the axion mass for which the coherence acquires its maximum corresponds to

$$m_a \simeq \sqrt{0.02 \frac{P_{He}[\text{mbar}]}{T_{He}[\text{K}]}}\,\text{eV}. \tag{7.1}$$

In order to scan for axions with masses up to 0.39 eV, CAST has made a total of 160 pressure settings that were distant ~ 0.085 mbar from each other. From now on we will refer to an specific j-setting where j is an integer index that goes from 1 to 160. This will simplify the notation of the formulas of this chapter.

7.2 Expected axion flux in the TPC detector

Once the pressure and temperature of the ^{4}He inmersed in the cold bore are stable, the axion-to-photon probability of conversion is the same for all CAST detectors. However, the specific experimental setup of each one of them may influence the expected outcoming photons.

The TPC detector, as well as the rest of detectors has taken into account the experimental conditions at CAST. The existence of the cold windows that hold the ^{4}He gas of the cold bore *(see section 5.3.1)* translates to a loss of efficiency for the TPC. The reason is that the cold windows are not fully transparent: the strongback of the cold windows has an optical free path of a 87.4 % while the 15 μm of polypropylene reduces the transmission of the Primakoff photons to the TPC.

The overall efficiency of the TPC detector during the ^{4}He run of the Second Phase of CAST is a 48 % and has been obtained by multiplying the TPC efficiency during the ^{4}He run *(see figure 7.1)* by the differential axion flux on Earth given in *section 4.2.2*.

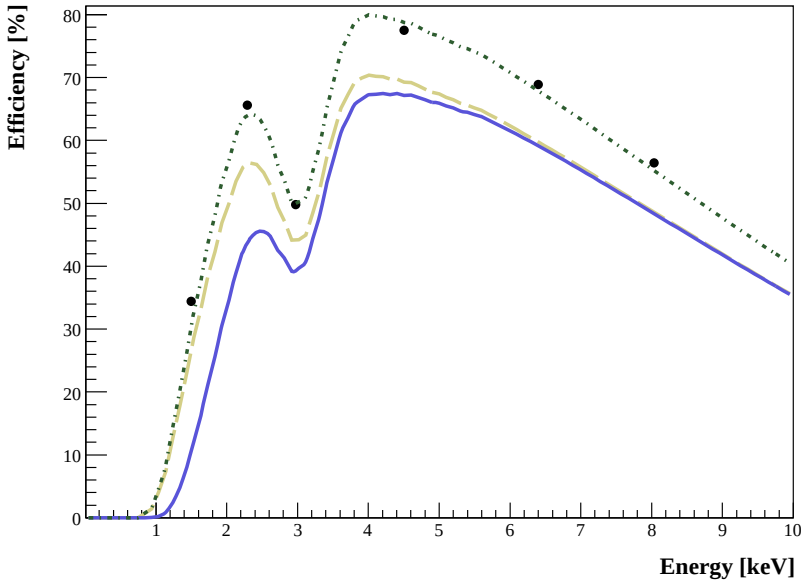

Figure 7.1: *The green dashed-dotted line is the analytical function used to interpolate the experimental points measured at the PANTER facility with the TPC detector (black dots). The yellow dashed line is the effect of the* 12.6 % *transparency of the cold window strongback. The solid blue line includes not only the effect of the strongback but also the transmission of the* 15 μm *polypropylene layer deposited on the cold window. phase.*

Taking into account the overall efficiency of the TPC and the exposure times of each pressure setting, we can proceed to calculate the Primakoff phontons that the TPC will be able to observe in a certain j-setting:

$$\mathcal{N}_{\gamma,j} = \frac{(\mathcal{N}_\gamma(P_j, m_a))_j}{(g_{a\gamma\gamma} \cdot 10^{10}\,\mathrm{GeV})^4} =$$

$$\int_0^L \frac{(d\phi_a/dE_a)}{(g_{a\gamma\gamma} \cdot 10^{10}\,\mathrm{GeV})^2} \cdot \frac{(\mathcal{P}_{a\to\gamma}(P_j, m_a, E_a))_j}{(g_{a\gamma\gamma} \cdot 10^{10}\,\mathrm{GeV})^2} \cdot S_{TPC} \cdot t_j \cdot \varepsilon(E_a) \cdot dE_a, \tag{7.2}$$

where $\varepsilon(E_a)$ is the efficiency of the TPC detector *(see figure 7.2)*, S_{TPC} is the sensitive area of the TPC detector ($29.54\,\mathrm{cm}^2$) and t_j the exposure time of the j-setting.

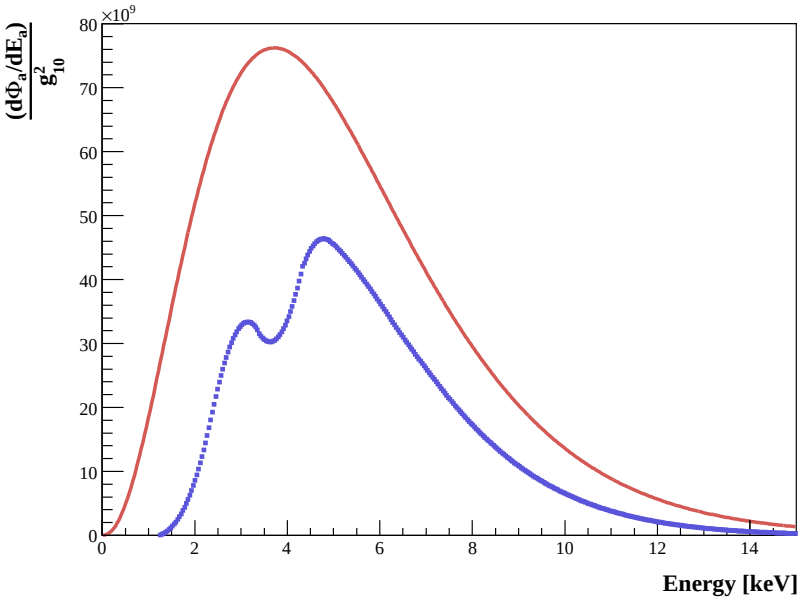

Figure 7.2: *In blue dots the differential axion spectrum, while the red line represents the overall efficiency spectrum of the TPC. A 48 % of the signal is expected to arrive to the detector.*

Equation 7.2 shows how the number of Primakoff photons expected by the TPC depends on the pressure of the j-setting and the mass of the axion that converts.

7.3 Axion-to-photon conversion probability

The coherence of the conversion due to the Primakoff effect tunes different axion masses for each one of the settings. *Equation 7.2* makes reference to the probabilty of converison $(\mathcal{P}_{a\to\gamma}(P_j, m_a, E_a))_j$ to express such dependence. For a specific j-setting, the axion-to-photon probability is:

$$\mathcal{P}_j = (\mathcal{P}_{a\to\gamma}(P_j, m_a, E_a)\,)_j = \\ \Big[\frac{g_{a\gamma\gamma}}{10^{-10}\,\mathrm{GeV}^{-1}}\Big]^2\Big[\frac{B_\perp}{2}\Big]^2 \cdot \frac{1}{q_j^2 + \Gamma_j^2/4} \cdot [1 + e^{-\Gamma_j L} - 2e^{-\Gamma_j L/2}\cos q_j L], \tag{7.3}$$

where q_j is the momentum transferred by the axion to the arising photon and Γ_j is the absorption that the photon suffers due to the fact that CAST uses ^{4}He as damping gas in the Primakoff conversion region.

Momentum transfer The transfer of momentum to the photons that are produced via the Primakoff effect in the CAST magnet depends not only on the energy of the axion, but also on its mass. *Section 4.3.1* shows into detail how the momentum transfer sets the axion masses for which the coherence of the Primakoff conversion is restored.

For a specific j-setting, the transfer of momentum q_j can be written as it appears in the following equation

$$q_j = \Big|\frac{m_\gamma^2 - m_a^2}{2E_a}\Big|. \tag{7.4}$$

Its dependency with m_a, allows not only to restore the coherence for a single axion mass, but for neibourghing axion masses too.

The momentum transfer can be unserstood as the acquirance of an effective mass by the arising photon and the maximum of the axion-to-photon probabilty of conversion is achieved when the effective mass is the one of the incoming

axion:

$$m_\gamma \equiv m_a \simeq \sqrt{0.02 \frac{P_{He}[\text{mbar}]}{T_{He}[\text{K}]}}\,\text{eV}. \tag{7.5}$$

From the above equation we can observe that the mass acquired by the outcoming photon is proportional to the square root of the ^{4}He pressure inside the magnet bore. Therefore, an increase of the ^{4}He density inside the cold bore of CAST restores the coherence of the conversion for axions with higher masses.

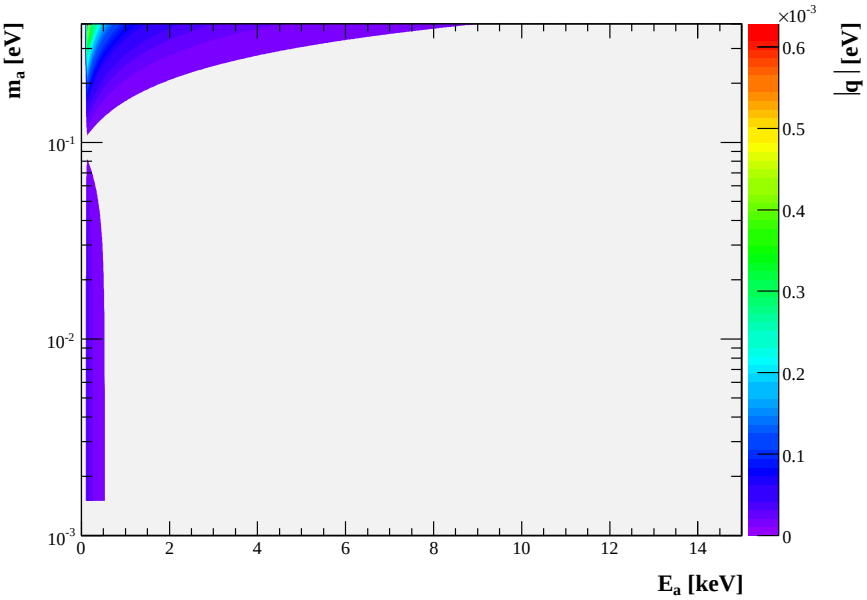

Figure 7.3: *Parametrization of the momentum transfer as a function of the incoming axion mass and the outgoing photon energy. Graph corresponding to the 10-setting.*

Figures 7.3 and *7.4* clearly show how for different pressure settings, the coherent axion mass range is varying.

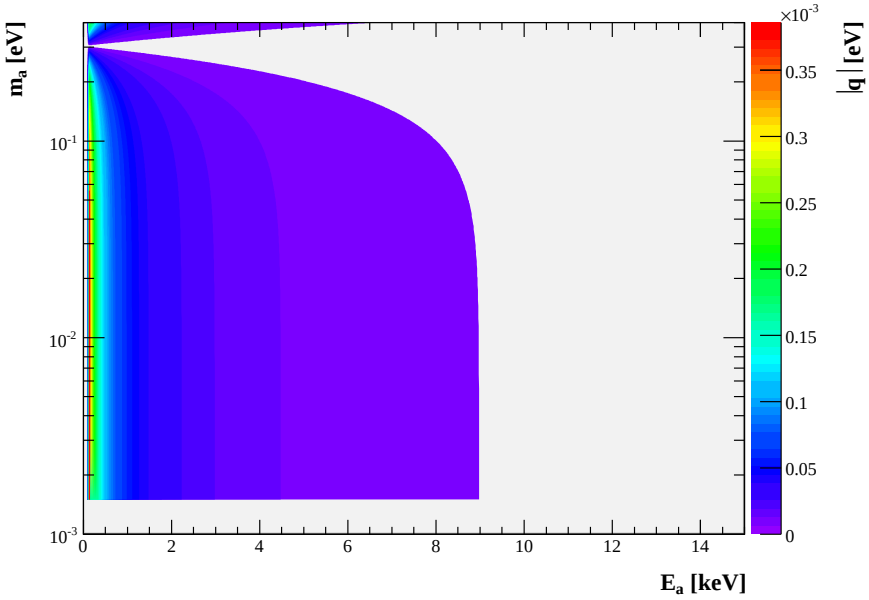

Figure 7.4: *Momentum transfer parametrization as a funtion of the incoming axion mass and the outgoing photon energy for the 100-setting.*

The absorption function Following the detailed explanation of *Section 4.3.2*, the presence of ^{4}He gas in the cold bore of CAST would diminish the expected number of photons to be detected by the TPC.

Absorption of Primakoff photons due to photoelectric effect, coherent and incoherent scattering in the ^{4}He depends on the gas density and on the energy of the photon arising from the conversion *(see figure 7.5)*.

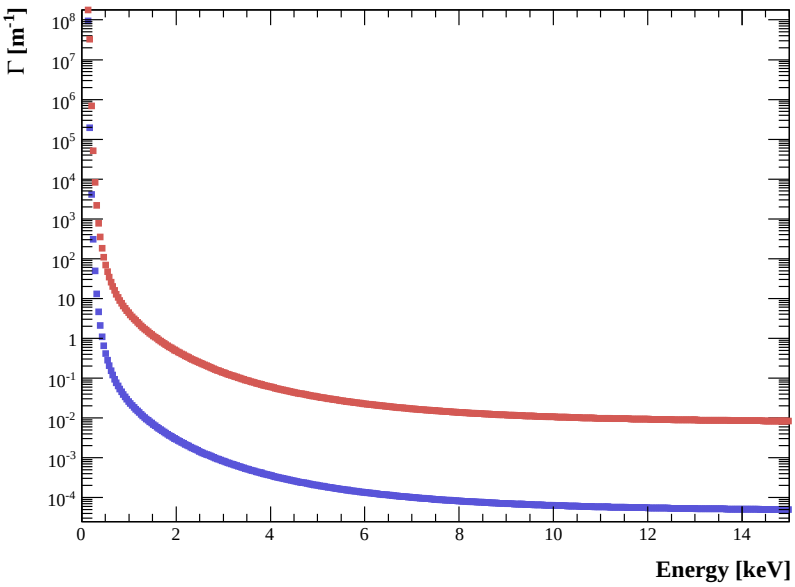

Figure 7.5: *Absorption of photons after the* 9.26 m *of CAST's magnet bore for the energy range of the TPC detector. In blue, the absorption as a function of energy in the 1-setting of CAST while the red line corresponds to the absorption in the 160-setting.*

7.4 TPC axion signal

Once the main contributions to the probabilty have been implemented to the TPC case, we can calculate the probabilities of an axion-to-photon conversion for all the j-settings measured at CAST. Since the momentum transfer to the photon depends on the mass of the axion arriving to CAST, the probability of conversion is also a function of m_a. A parametrization of the probabilities respect the energy of the outgoing photons and the incoming axion masses is a nice exercise from which we will know what is the energy range more likely to have a signal.

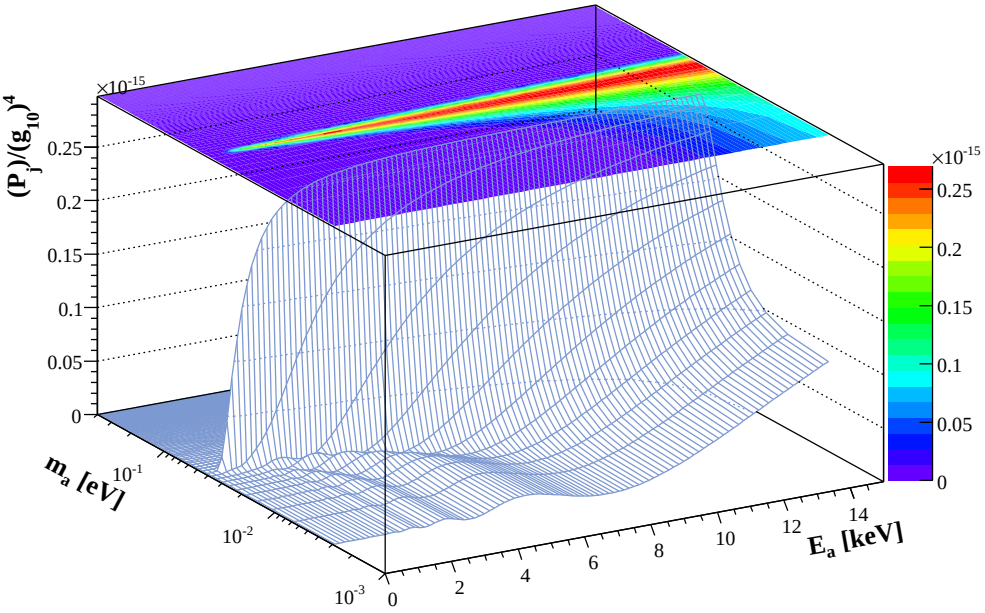

Figure 7.6: *Probability of conversion of the 2-setting.*

Figure 7.6 shows how the conversion probability achieves its maximum for the axion mass range nearby the effective mass of the arising photon. Also, for axions whose masses are off-coherence, the probability of detection is enhaced to specific energy regions of the spectra.

Axion flux, sensitive area and statistics After calculating the probability of conversion for all the j-settings measured at CAST, the next step is to include the differential axion flux on Earth. The sensitive area of the TPC detector ($29.54\,\mathrm{cm}^2$), together with the measuring times for each j-tracking have to be taken into account in order to make a precisse calculation of the differential photon flux that the TPC expects from the axion-to-photon Pri-

makoff conversion happening in the CAST magnet.

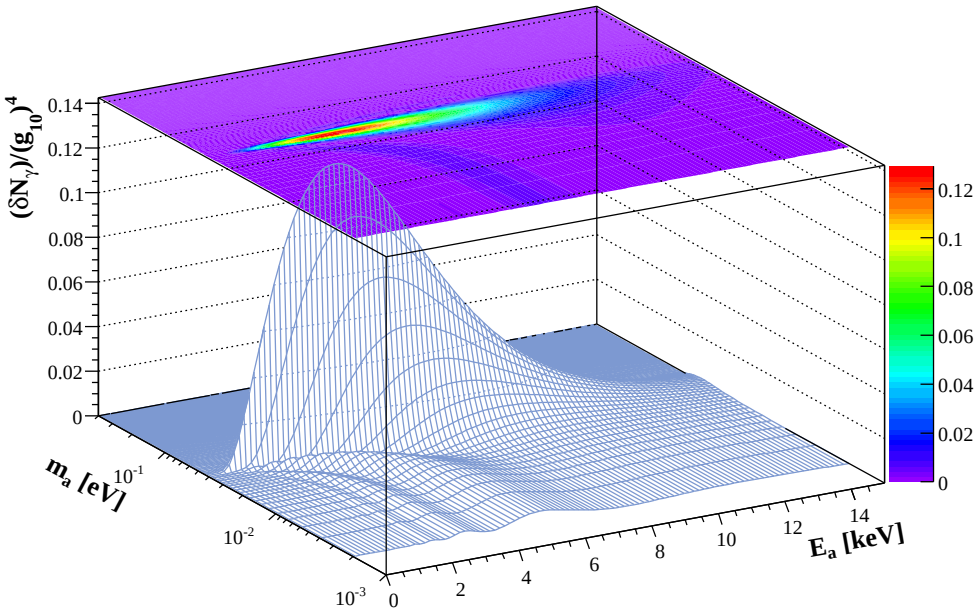

Figure 7.7: *Differential flux of photons on the TPC detector once the statistic of each j-tracking and the sensitive area of the detector are taken into account.*

Overall TPC efficiency A further step to be done is the implementation of the efficiency of the TPC detector during the ^{4}He run of CAST's Second Phase. As pointed out in *Section 7.2*, the overall efficiency of the TPC detector is a 48 % of the differential axion flux *(see figure 7.8)*.

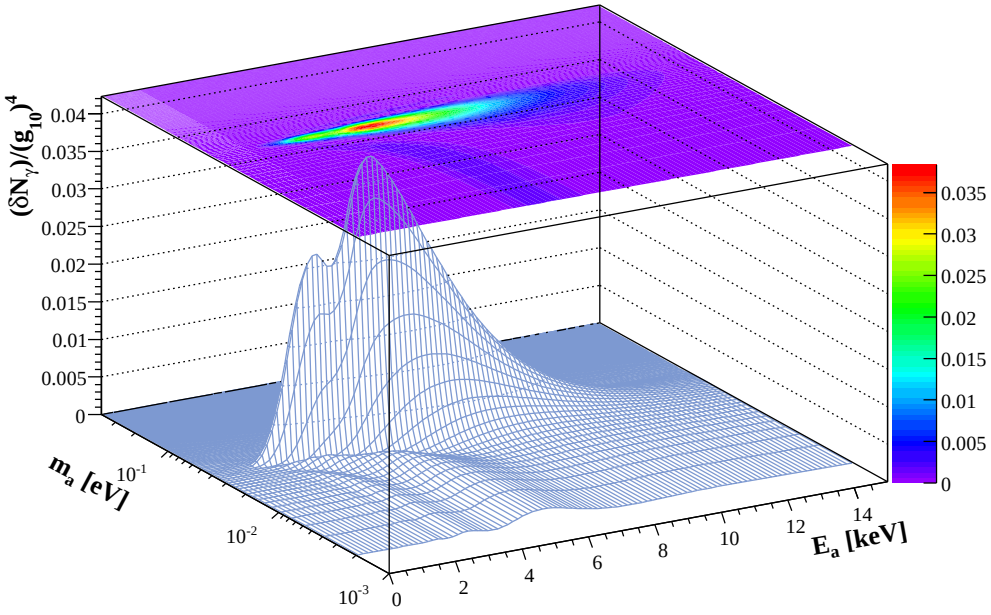

Figure 7.8: *Differential axion flux of the TPC detector once it has been convolutioned with the TPC overall efficiency.*

Expected number of photons of the j-setting The TPC energy resolution is 0.5 keV and, therefore, the expected number of photons must be compared to the TPC signal with an energy interval according to the one of the detector. Integrating the expected photons over the energy range of each i-bin of the TPC spectra we will obtain

$$(\mathcal{N}_\gamma)_{i,j} = \int_{E_o}^{E_f} \frac{d\phi_a}{dE_a}(E_a) \cdot \mathcal{P}_{a\to\gamma}(E_a) \cdot S \cdot t \cdot dE_a, \tag{7.6}$$

that can be directly compared to the tracking counts observed by the detector in a j-setting. This number, obtained for the $[E_o, E_f]$ energy range whose $\Delta E = E_f - E_o = 0.5\,\text{keV}$, is proportional to the fourth power of the axion-to-

photon coupling (g_{10}^4) and it is the one needed in order to discriminate wether the tracking and background spectra of the j-setting are compatible with the absence of axion signal in the TPC detector.

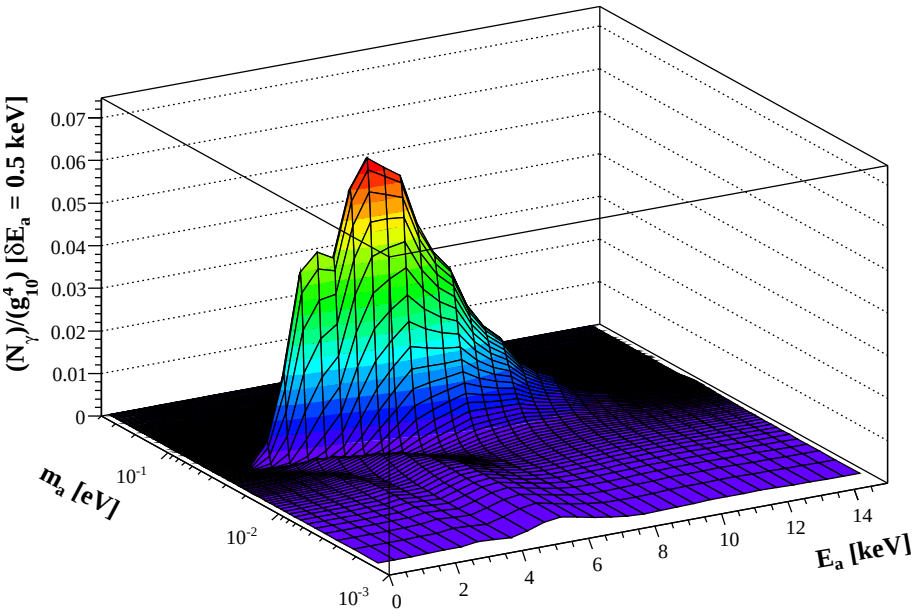

Figure 7.9: *Expected number of photons for each TPC bin spectra in the 2-setting.*

The total number of photons expected by the TPC in a j-setting is obtained by integrating *figure 7.9* over the whole energy range of the detector.

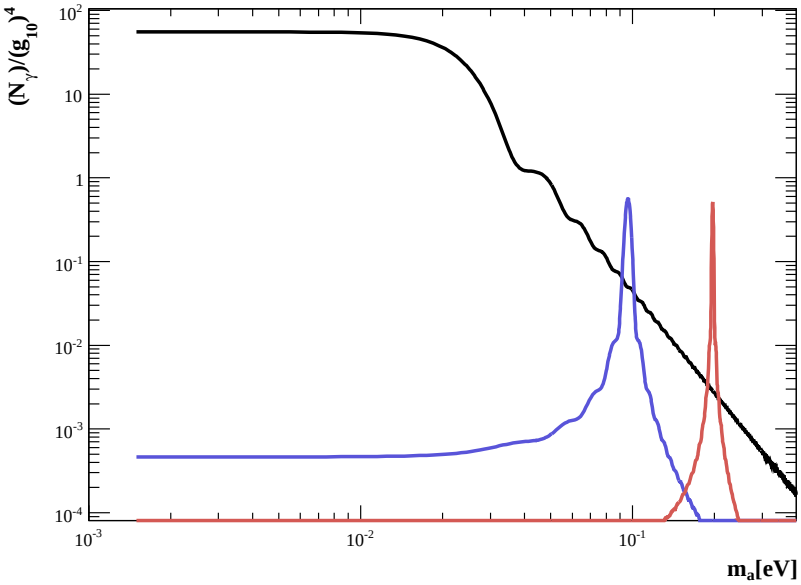

Figure 7.10: *Comparison between the expected photons in the TPC detector during the First phase of the CAST experiment (black) and the expectation for two different pressure settings during the* ^{4}He *Phase (red and blue). CAST First Phase loss coherence for photons with masses above* 0.02 eV, *but the technique of the pressure settings used at CAST restores it for the narrow regions that correspond to the effective mass of the photon. The black line, which corresponds to the vacuum phase is below the corresponding red or blue lines that represent two different pressure settings for which the coherence is restored.*

Chapter 8

TPC analysis

The present chapter is a detailed explanation of the analysis that have been done to the data obtained with the TPC detector in the ^{4}He phase of the CAST experiment. The following lines try to explain the process that allows the obtention of a limit to the axion-to-photon coupling via the Primakoff effect.

8.1 Analysis methodology

The analysis of the data gathered by the TPC detector during the ^{4}He run of CAST's Second Phase has two different stages. The first test consists on searching for axion-to-photon Primakoff signals in the TPC data obtained for the different j-settings. This is accomplished by comparing tracking and background spectra in order to check for compatibility of the data within statistical fluctuations. Unfortunately, no traces of an axion signal have been identified after crosschecking the tracking and background spectra data collected by the TPC at all the j-settings.

Under the absence of signal assumption, the analysis of the TPC detector extracts the limit to the axion-to-photon coupling via the Primakoff effect.

The detection process of a physical event due to the background is Poissonian and, therefore, the expected counts in the detector for a specific j-tracking in the i energy bin of the spectrum goes as a Poissonian distribution with mean

$$\lambda_{ij} = b_{ij} + N_{\gamma,ij}(m_a) \times g_{10}^4. \tag{8.1}$$

In the above expression, b_{ij} is the number of counts in the i-bin of the j-tracking background spectrum. The perfect knowledge of the expected photons coming from the axion-to-photon conversion that take place in the CAST magnet allows to calculate the term $N_{\gamma,ij}(m_a) \times g_{10}^4$, the expectation from the theoretical calculation for the i-bin of the j-setting *(see figure 8.1)*.

As a matter of fact, the compatibility of tracking and background spectra can be done by using the likelihood method, that with the mean above mentioned is built as

$$\mathcal{L}_j = \prod_i^n \frac{t_{ij}!}{e^{-t_{ij}} t_{ij}^{t_{ij}}} \prod_i^n \frac{e^{-\lambda_{ij}} \lambda_{ij}^{t_{ij}}}{t_{ij}!} = \frac{1}{\mathcal{L}_{0j}} \prod_i^n \frac{e^{-\lambda_{ij}} \lambda_{ij}^{t_{ij}}}{t_{ij}!}, \tag{8.2}$$

where we compare the tracking counts of the i-bin in the j-tracking t_{ij} with the expected mean for the same bin and tracking λ_{ij}.

Once the individual likelihoods of all the j-settings are built, we can con-

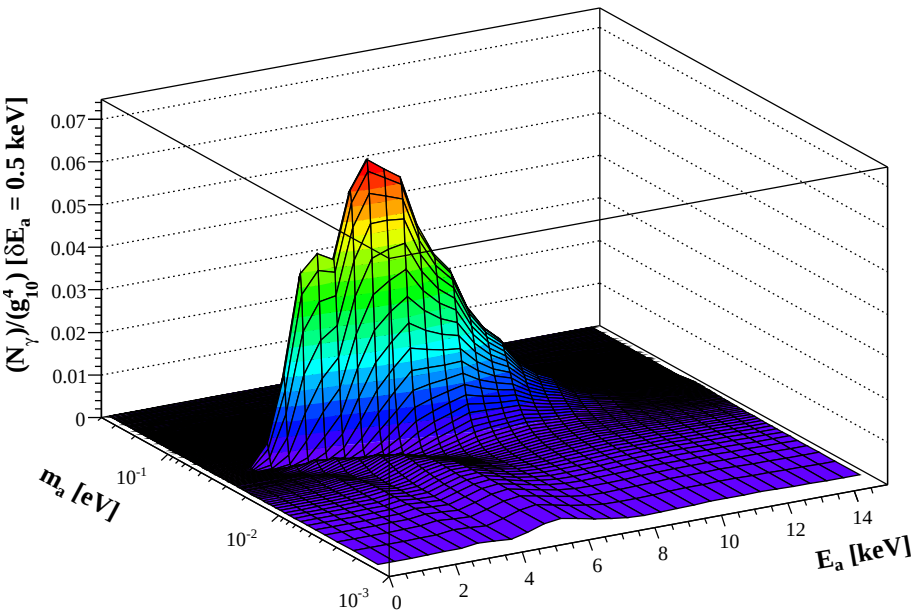

Figure 8.1: *Dependence of the $N_{\gamma,ij}$ expected in the different energy bins of the TPC spectra relative to the effective ^4He gas pressure P_i^* of the corresponding axion mass m_a for the case of setting number 2, which corresponds to $P_i^* = 0.16162$ mbar inside the magnet bore of the CAST experiment.*

struct the global likelihood, product of all the j-setting likelihoods. The global likelihood is the instrument that we will use in order to obtain the axion mass dependence of $N_{\gamma,ij}$ with the strength of the coupling g_{10}:

$$\mathcal{L}_{Global} = \prod_j \mathcal{L}_j. \tag{8.3}$$

Since by construction we have made the likelihoods compatible within the χ^2 method, we can also calculate the χ^2 of the specific j-settings as well as the global one:

$$\chi^2_{Global} = \sum_j \chi^2_j = \sum_j [-2\log(\mathcal{L}_j)]. \tag{8.4}$$

The advantage of using the χ^2, besides the computational accuracy due to the simple addition of the logarithms for all the settings, is the goodness of fit test.

The term $\mathcal{L}_{0j}$ that was introduced in the j-likelihoods is a normalizing constant that makes $[-2\log\mathcal{L}_j]$ to behave as a χ^2 distribution in the asintotic limit. Therefore, it allows the goodness of fit test for the j-settings measured by the TPC:

$$\chi^2_{null,j} = \chi^2_j(g^4_{10} = 0). \tag{8.5}$$

The $\chi^2_{null,j}$ distribution can be compared with the theoretical $\chi^2_{d.o.f}$ *(see equation 8.6)* curve that can be reproduced for the degrees of freedom that are being used for the analysis, the *N-1* bins of the tracking and background spectra. In such histogram, we can represent the different values of the $\chi^2_{null,j}$ in the x-axis, while the y-axis represents the multiplicity of each value:

$$\chi^2_{Th}[d.o.f = N-1] = \frac{1}{2^{[d.o.f]/2}\Gamma([d.o.f]/2)} \quad x^{([d.o.f]/2)-1} \quad e^{-x/2}. \tag{8.6}$$

The whole likelihood method applied to the TPC data in order to obtain a limit to the axion-to-photon coupling constant relies on the accumulation of enough statistics for the background, since it assumes the absence of statistical errors in the background data to calculate the mean λ_{ij} of *equation 8.1*.

8.2 TPC data

The TPC detector has taken a total of 4422 hours, 33 minutes and 50 seconds of data, which corresponds to

- *Tracking data:* 296 hours, 16 minutes and 56 seconds.
- *Background data:* 4126 hours, 16 minutes and 54 seconds.

The tracking data taken by the TPC during this period implies a 92.5 percent efficiency. However, the TPC was not able to take tracking data for 12 settings and a total of 148 over 160 pressure settings measured by CAST have been taken into account to make the corresponding likelihoods for the final TPC analysis.

8.2.1 Tracking data

The definition of the "tracking spectra" for a j-setting consider all the data of the j-setting while tracking time that was taken in normal operation by the TPC and that corresponds to the required *accuracy of Sun tracking* in CAST. Moreover, the condition of *B field* presence in the magnet (8.80 T) as well as the opening of *VT1 and VT2 valves* is forced in order to include the data into the analysis.

8.2.2 Background data

For the background spectra of each one of the j-settings, the definition has been done in several independent ways:

- **Daily background:** defined as the data taken by the TPC while the magnet was not in evening tracking during the days in which the j-trackings were taken.
- **Nearby background:** defined as the data taken by the TPC while the magnet was not in evening tracking and nearby the corresponding day of the setting.
- **Off-coherence tracking:** TPC tracking data in off-coherence settings.
- **Combined background:** The addition of the Off-coherence and the Nearby backgrounds above mentioned.

From the first phase of the CAST experiment it is known that the background of the TPC detector is dependent on its position along the CAST experimental hall. A shielding of polyethylene, lead, cadmium and copper managed to

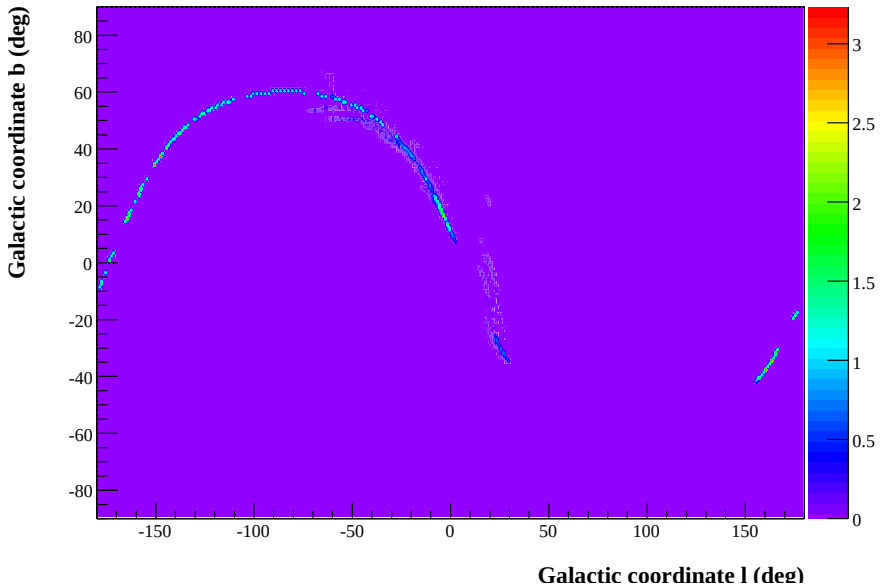

Figure 8.2: *Exposure hours of the TPC detector to the solar core during the* ^{4}He *run of the Second Phase of CAST. It can be seen how the positioning of the TPC detector corresponds to the ecliptic that the Sun describes in galactic coordinates.*

diminish the effects of the position during the first phase of CAST and so it did during the second phase.

The possibility of a Radon contamination due to its presence in the air of the experimental setup is eliminated thanks to a flux of Nitrogen gas such that it generates an overpressure inside the shielding layers avoiding the air from the experiment to go into deep layers of the shielding and contaminate it. The technique was already used during the first phase of CAST since the Radon gas contamination is, in fact, the most dangerous TPC systematic once the shielding is installed.

It happened that for the settings *1* to *27* of CAST second phase, there existed

an air leak towards the TPC detector, which allowed Radon to go through the different layers of shielding and increase the level of counts per hour *(see figure 8.4)*. This leak was solved afterwards and the contribution of Radon to the TPC background remained stable and under control till the end of the data taking.

In the following lines I will explain more into detail the criterium of background selection that has been used.

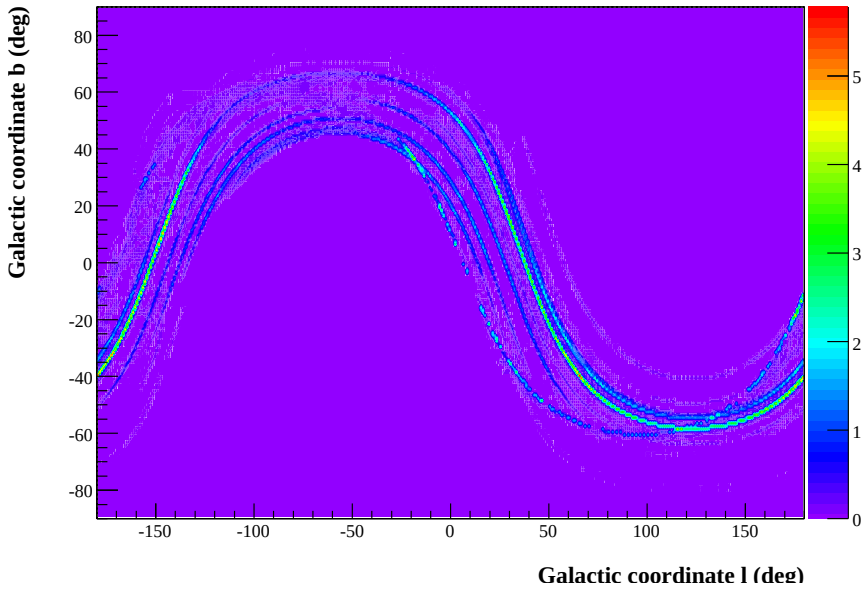

Figure 8.3: *Hours of background exposure (no Sun tracking) of the TPC detector in galactic coordinates.*

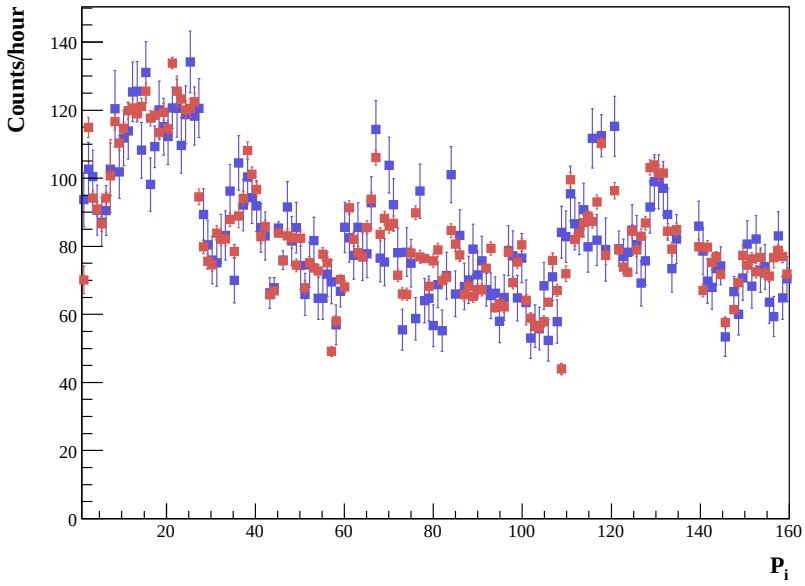

Figure 8.4: *Daily variation of the background (red) and tracking counts (blue) in counts per hour that the TPC detector has in the two windows for each j-setting. The energy range that has been taken into account goes from 2 to 12 keV*

Nearby background In the situation of no evening tracking, the TPC detector was placed all around the CAST hall experiment along the year. Different parking positions of the magnet as well as the need of data taking for the morning detectors makes neccessary a selection criteria for the data taken by the TPC in such conditions.

As for the trackings, the very first requirement to the background data is to have the CAST magnet with current and to have the valves VT1 and VT2 open.

The selection criterium for the Nearby background has been to group the backgrounds of the ten nearest days to the tracking that corresponds to the

j-setting:

$$\mathcal{B}_{ij}(b) = \sum_{k=j-5}^{k=j+5} b_{ik} \quad , \qquad \forall j. \tag{8.7}$$

Taking into account that most of the settings have a tracking of the order of 1 hour and 45 minutes, the corresponding statistics coming from the grouping above mentioned makes the error bar of the outcoming Nearby background of the j-setting to reduce a factor $\simeq$ 10 relative to the tracking error bars *(figure 8.5)*.

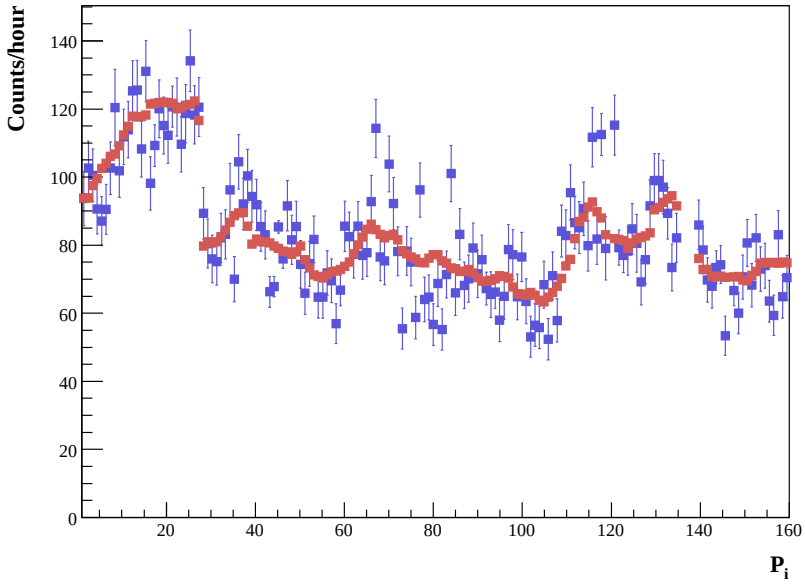

Figure 8.5: *Rate of events for the Nearby background definition (red) versus the tracking rates (blue) for all the j-settings. Rates calculated for the energy range of 2 to 12 keV.*

Off-coherence tracking Another possible definiton of background for the detectors of the CAST experiment is given by the fact of the coherence effect in the axion-to-photon conversion.

Those trackings off-coherence referred to a j-tracking can be used as background of the j-setting. In other words, trackings far from the j-setting do not contribute to the expected photons from axion-to-photon Primakoff coupling of the j-tracking and, therefore, they can be used as backgrounds.

As it has been seen in *figure 8.4* the effect of statistical and systematic fluctuations of the daily background and tracking spectra forces a selection of the trackings that are to be consider as background for an specific j-setting.

The criteria chosen to build the Off-coherence tracking constructs a background spectra for each j-setting that corresponds to the addition of the closest possible off-coherence trackings.

We will define the Off-coherence tracking as

$$\mathcal{B}_{ij}(t) = \sum_{k=j-3}^{k=j-10} t_{ik} + \sum_{k=j+3}^{k=j+10} t_{ik}. \tag{8.8}$$

The accumulated statistics are not as large as for the Nearby background definition, but even like that, the error bar of the backgrounds are still in average a factor $\simeq 4$ times smaller than the ones from the trackings as it can be seen in *figure 8.6*.

Combined background Combinedly, after the previous studies we could procceed to build what we will call Combined background of the j-setting:

$$\mathcal{B}_{ij} = \mathcal{B}_{ij}(t) + \mathcal{B}_{ij}(b) = \sum_{k=j-3}^{k=j-10} t_{ik} + \sum_{k=j+3}^{k=j+10} t_{ik} + \sum_{k=j-5}^{k=j+5} b_{ik}. \tag{8.9}$$

The Combined background is the simple addition of the statistics generated by the previous cases which has an inherent biasing of $\simeq 28$ hours from the Off-coherence tracking and $\simeq 200$ hours from the Nearby background.

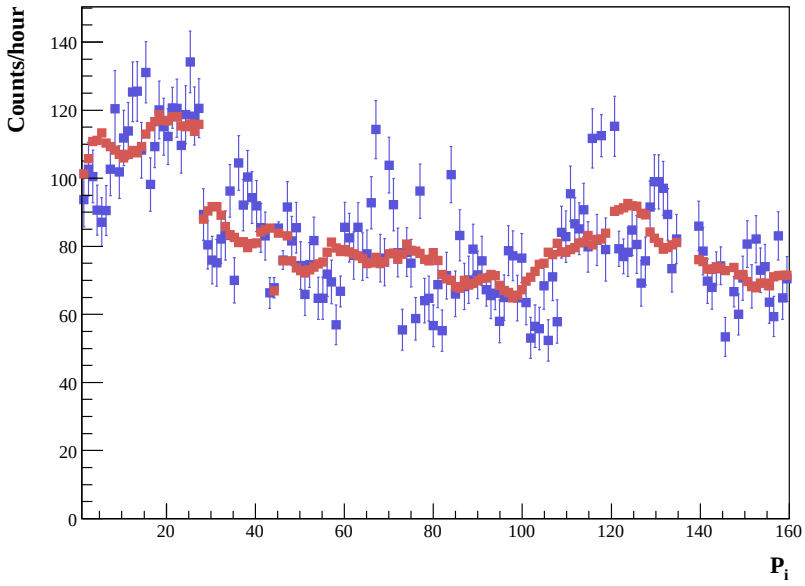

Figure 8.6: *Counts per hour of the Off-coherence trackings (red) for all the j-settings versus their tracking counts per hour (blue) in the 2 to 12 keV energy range.*

This becomes a total of $\simeq$ 228 hours of background. Statistically, the error bars of the Combined background spectra are $\simeq$ 15 times smaller than the ones from the tracking of the specific setting. The reduction factor depends on the accumulated statistics for the Combined background of the setting that we consider.

8.3 Analysis of the TPC data

Once we have clearly defined the spectra of tracking and background that are to be used in the likelihood method of the analysis we should procceed first of all to build the individual j-setting likelihood.

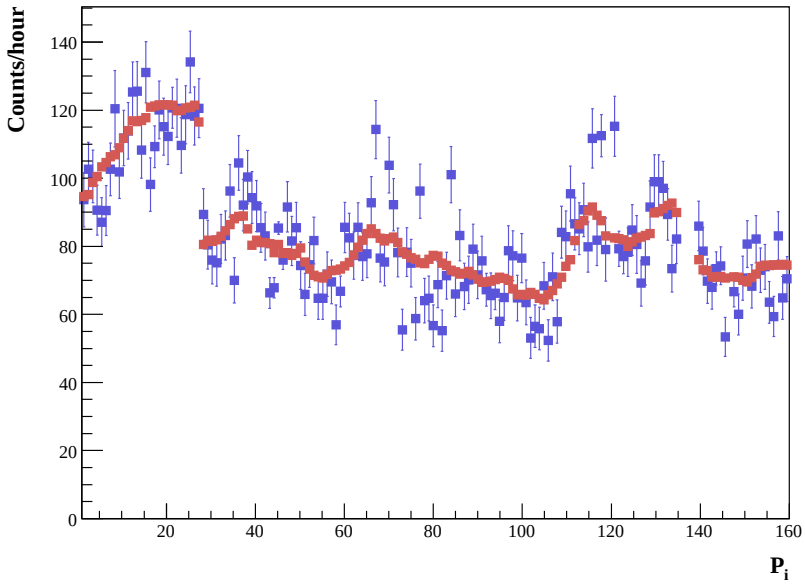

Figure 8.7: *Counts per hour of the Combined backgrounds for all the j-settings versus their tracking counts per hour. Energy range from 2 to 12 keV.*

8.3.1 Construction of the individual likelihoods

With the knowledge of the expected number of photons from axion-to-photon conversion due to Primakoff effect in the CAST magnet as a function of the axion mass and the value of the coupling constant g_{10} we can procceed to the application of the likelihood method that has been introduced in *Section 8.1*.

The criterium of the analysis is to scan the different axion masses for which the values of g_{10}^4 minimize the χ^2. The most probable value for the axion-to-photon coupling constant validating our data of tracking and background.

Since the scan of m_a has to be comparable within the rest of the detectors, the range of axion masses under study has been set to those corresponding

to a ^{4}He pressure between 0 and 15 mbar inside the coldbore of the CAST experiment assuming its temperature constant at 1.8 K. The interval of the scan is 0.01 mbar which implies the generation of 1500 χ^2 for each one of the j-settings of the TPC detector.

The evaluation of the χ^2_j is done by giving a value of g^4_{10} and plotting it for each m_a. In the case of the TPC, the range of values that has been selected for g^4_{10} is between -85 and 40000 units and two different step sizes are used.

- $g^4_{10} \in [-85, 256]$*:* Step size of 0.125 units. Allows a fine reconstruction of the χ^2_j up to $g_{a\gamma\gamma} = 4 \times 10^{-10}\,\mathrm{GeV}^{-1}$. Almost 100 percent of the j-settings have the $\chi^2_j \pm 3\sigma$ within this range for the axion mass that corresponds to the coherent one.
- $g^4_{10} \in [257, 40000]$*:* Step size of 100 units. Allows the computation of $g_{a\gamma\gamma}$ up to almost $1.42 \times 10^{-9}\,\mathrm{GeV}^{-1}$. A useful range for those axion masses in which the lost of coherence starts to appear.

By using the *equation 8.4* we are able to evaluate the χ^2 of the j-settings. The term λ_{ij} is the mean of the Poissonian distribution of the i-bin for the j-setting *(equation 8.1)* and introducing it into the calculation of the individual χ^2 allows to express

$$\chi^2_j = -2 \times \log\left[\mathcal{L}_j\right] = -2 \times \sum_{i=1}^{n} [(t_{ij} - \lambda_{ij}) + t_{ij} \times (\log \lambda_{ij} - \log t_{ij})]. \quad (8.10)$$

Since the χ^2_{null}, also known as null hypothesis test, is valid for the definition of the likelihood that we are using, we can make a representation of the multiplicity of the $\chi^2_{null,j}$ values and their correspondence with the theoretical $\chi^2_{Th}[d.o.f]$. *Figure 8.8* includes the representation of the theoretical curve and the $\chi^2_{null,j}$ obtained with the daily TPC data. The range of the analysis is done from 2 to 12 keV and the energy bins have a size of 0.5 keV. Therefore, the corresponding theoretical $\chi^2_{Th}[d.o.f]$ is being calculated for 19 degrees of freedom:

$$\chi^2_{null,j} = -2 \times \sum_{i=1}^{n} [(t_{ij} - b_{ij}) + t_{ij} \times (\log b_{ij} - \log t_{ij})]. \quad (8.11)$$

This method, allows the visualization of the agreement between the background

and tracking data of the TPC. We just have to notice the fact that by doing $g_{10}^4 = 0$ all the terms that are involved in the $\chi^2_{null,j}$ calculation are just the counts of tracking and background of the j-setting in the i-bin of the spectra.

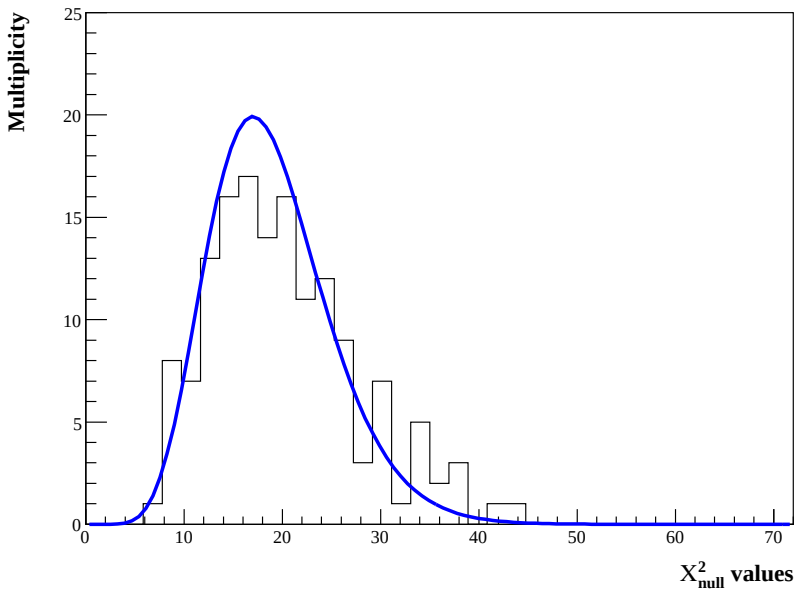

Figure 8.8: *Representation for the multiplicity of the $\chi^2_{null,j}$ values of the j-settings (black histogram) versus the theoretical curve for the 19 degrees of freedom of the TPC analysis (thick blue line). Daily background has been used.*

The respective values of the $\chi^2_{null,j}$ in the settings calculated for the specific axion mass of the coherence can be used to plot an histogram to observe the evolution along the settings *(see figure 8.8)*, with

$$m_a[\mathrm{eV}] \backsimeq \sqrt{0.02 \quad \frac{\mathrm{P_j^*[mbar]}}{\mathrm{T_j^*[K]}}}. \tag{8.12}$$

This provides us an idea of how compatible the induvidual likelihoods of the

j-settings are with the hypothesis of absence of signal. This can be seen by the fact that $\chi^2_{min,j}$ should be around $g^4_{10} = 0$ since in absence of signal, the most probable value of the coupling constant is zero.

8.3.2 Construction of the global likelihood

Once we have been able to calculate each one of the likelihoods for the j-settings, we can proceed to build what we called in *Section 8.1* the global likelihood *(equation 8.3)*. As in the previous section, instead of multiplying the probabilities of each one of the j-settings for each axion mass, we will just add the values of the χ^2_j.

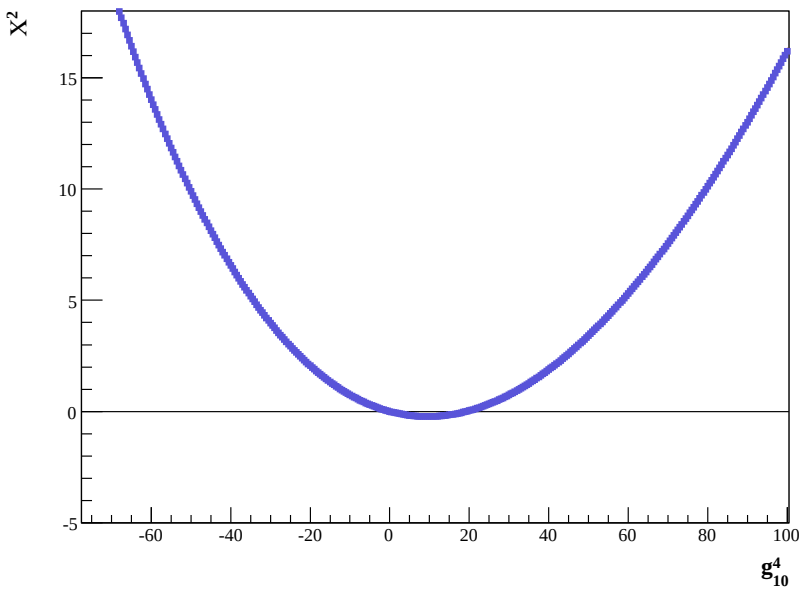

Figure 8.9: *Example of a $\chi^2_{m_a}$ curve obtained for the global likelihood analysis. It corresponds to $m_a = 0.149\,eV$ and its value is depending on the axion-to-photon coupling g^4_{10}.*

Following the expression from *equation 8.4*, we can write

$$\chi^2_{Global} = \sum_{j=1}^{sets} \chi^2_j = -2 \times \sum_{j=1}^{sets} \sum_{i=1}^{n} [(t_{ij} - \lambda_{ij}) + t_{ij} \times (\log \lambda_{ij} - \log t_{ij})], \quad (8.13)$$

and with this definition, we can easily calculate all the 1500 $\chi^2_{m_a}$ of the analysis if we just plot the dependence of g^4_{10} versus the χ^2 value once we have fixed m_a *(figure 8.9)*.

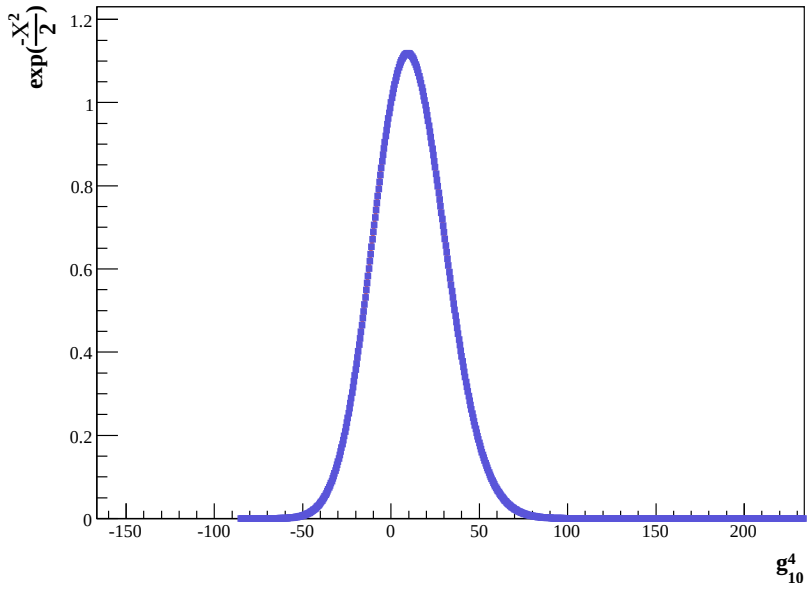

Figure 8.10: *Example of a probability function choosen for one of the axion masses of the analysis:* $m_a = 0.149\,eV$.

From the χ^2 curves of the specific axion masses, we can build the probability functions of each mass:

$$\mathcal{P}_{m_a} = \exp \frac{-\chi^2}{2}. \quad (8.14)$$

Therefore, we will know the most probable value of g_{10}^4 that fits our data *(see figure 8.10)* .

Each one of the $\chi^2_{m_a}$ has been fitted to an eighth polynomial in order to simplify the portability of the data.

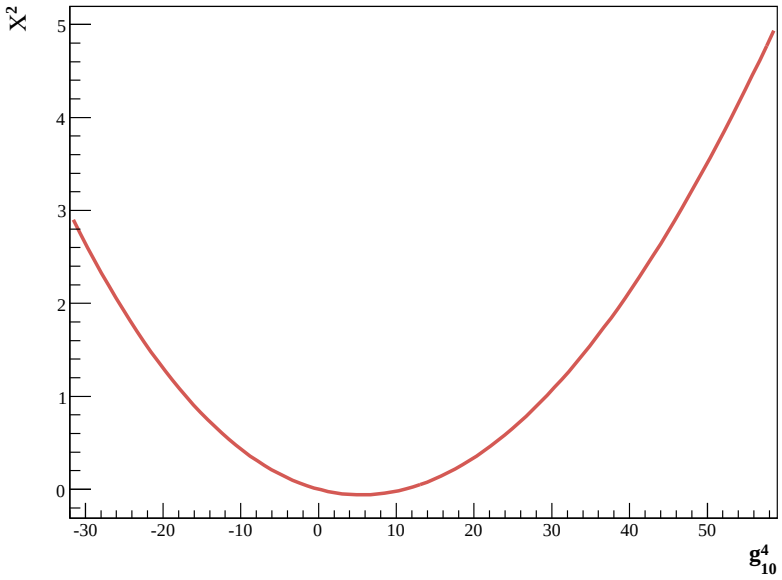

Figure 8.11: *Example of a fit to the $\chi^2_{m_a}$ curve obtained for the global likelihood analysis at* $\mathrm{m_a} = 0.149\,\mathrm{eV}$.

A important crosscheck that can be done before the combination of the data is the so-called $\Delta\chi^2_{m_a}$.

Having into account that in the whole global likelihood there is only one free parameter, the statistical fluctuation theory tells us that the value of the difference between χ^2_{min,m_a} and χ^2_{null,m_a} should follow a Gaussian distribution

centered in 0 and with FWHM of 1σ. Hence, it can be a nice quality check for our analysis *(see figure 8.12)*:

$$\Delta\chi^2_{m_a} = |\chi^2_{min,m_a} - \chi^2_{null,m_a}| \leq 1. \tag{8.15}$$

The result of this crosscheck tell us that the data of the TPC that are out of the 1σ boundary are a 27.17 %, result compatible with the percentage of area below a sigma in a Gaussian distribution 31.8 %. The data out of the 2σ boundary are a 4.89 % while for a Gaussian distribution is a 4.6 %.

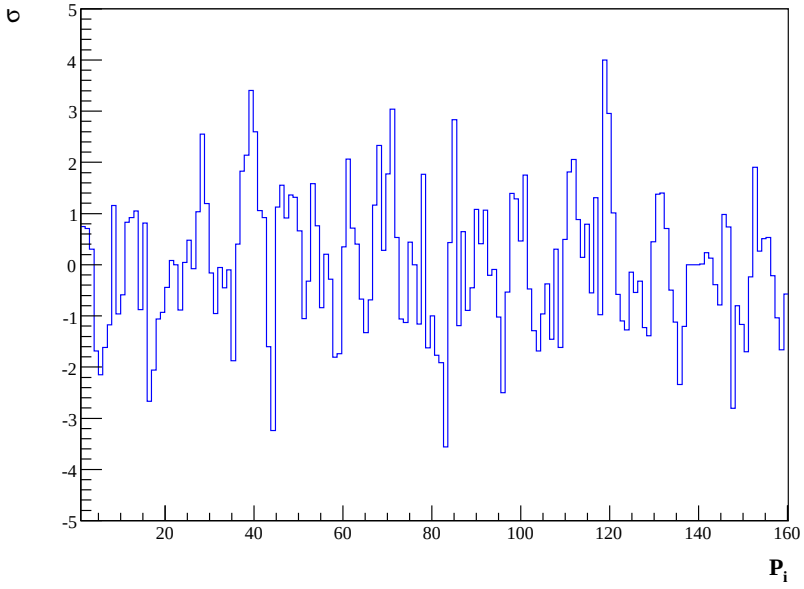

Figure 8.12: *Representation of the evolution of the difference in sigmas between $\chi^2_{null,j}$ and $\chi^2_{min,j}$ for the equivalent axion mass m_a coherent to the pressure P^*_j with which the cold bore of the CAST magnet was filled during j-setting for the TPC detector.*

Statistical errors The estimation of the standar deviation errors of the analysis carried out for the TPC data follows the formula

$$[\chi^2(g_{10}^4)]_{m_a} = [\chi^2_{min}(g_{10}^4)]_{m_a} + \sigma^2 \tag{8.16}$$

and, it has also considered that the χ^2 distributions of the TPC are not symmetric *(see Table 8.1)*.

Statistical error $[g_{10}^4]$
$g_{10}^4(\min)^{+11.921}_{-4.726}$

Table 8.1: *Statistical errors in g_{10}^4 units for the $g_{10}^4(min)$ result of the TPC.*

8.4 Study of the systematic errors for the TPC detector

Previous presentation of the final result for the TPC detector of CAST, we must evaluate the possible systematic errors that might affect the analysis of its data. This section introduces and evaluates the effect of the most important experimental uncertainties of the CAST experiment as well as the effect of different background definitions for the TPC.

8.4.1 Experimental uncertainties

A first attempt to study the systematics of the TPC analysis includes the most critical uncertainties of CAST. The errors of the magnetic field intensity, its length and the uncertainties of the TPC efficiency detector are of vital importance for the study of the systematics.

Strength of the magnetic field The LHC dipole magnets, and CAST among them, use electric current in order to be able to generate a certain magnetic field in the cold bores. The intensity of the field that an LHC dipole magnet like CAST can provide has a linear dependence with the electric intensity applied to it.

Intensity I [A]	**Magnetic field B [T]**	**Step B/I [$T \cdot kA^{-1}$]**
0	0	0.682
4988	3.4	0.682
8981	6.12	0.6811
10977	7.46	0.6796
12000	8.13	0.678
12808	8.66	0.676
13330	9.00	0.675

Table 8.2: *List of values for the magnetic field of the CAST magnet according with the current applied to it.*

The data shown in the *table 8.2* was obtained at the test bench of the CERN dipole magnets and allow to generate the linear dependence of the magnetic field with the intensity applied:

$$B[\mathrm{T}] = (6.758 \times 10^{-4} \pm 2.3 \times 10^{-6}) \times \mathrm{I}[\mathrm{A}] + (1.9 \times 10^{-2} \pm 2.3 \times 10^{-2}). \quad (8.17)$$

During the ^{4}He run of the Second Phase of CAST, the intensity applied to the magnet was 13 kA, which corresponds to a magnetic field intensity of 8.805 ± 0.037 Tesla.

To include the systematic errors of the magnetic field intensity in the TPC analysis, we have evaluate the displacement of the $(g^4_{10})_{min}$ in the $\chi^2_{m_a}$ curves and its effect to the axion-to-photon coupling.

Magnetic field [B]	χ^2 **systematic error** [g^4_{10}]
8.8 ± 0.037 Tesla	$g^4_{10}(\text{min})^{+0.097}_{-0.098}$

Table 8.3: *Systematic errors in g^4_{10} units from the uncertainties of the magnetic field intensity.*

Length of the magnetic field Another possible source of systematic errors at the CAST experiment is the accuracy of the magnetic field length. The magnet that is being used in the CAST experiment was fully characterized in the test bench at CERN. The intensity of magnetic field is confined to a length of 9.26 m. However, this value is not exent of a certain error ± 0.05 m.

An study for the effect of such differences has been also applied to the case of the TPC data

Magnet length [L]	χ^2 **Systematic error** [g^4_{10}]
9.26 ± 0.05 meter	$g^4_{10}(\text{min})^{+0.006}_{-0.005}$

Table 8.4: *Systematic errors in g^4_{10} units from the uncertainties of the magnet length.*

Efficiency of the TPC detector As for tthe rest of the detectors of CAST, the overall efficiency of the TPc depends on the quantum efficiency as well as transmission of the Primakoff photons generated in the magnet of CAST through the different components of the experiment such as the cold windows and the TPC windows.

As a reminder we will mention that the overall efficiency of the TPC considered for the analysis of the ^{4}He data is 48.23%. However, as for the two quantities mentioned in the previous lines, the determination of the efficiency is not exent of systematics.
Luckily, the measurements carried on in Panter with the TPC detector characterized the behaviour of the TPC data. For the effect of the efficiency uncertainties to the axion-to-photon limit extraction we have consider then the errors arising from the Panter characterization together with the ones arising from the transmissionn coeficients used for the cold windows and the TPC windos.

The inclusion of such errors slightly shift the efficiency to be used for the analysis of the data. A way of quantifvying the effect in the efficiency of the TPC is calculating the overall efficiency arising for each one of the cases and giving an upper and a lower limit for the efficiency systematics of the TPC as it appears in the following table:

TPC overall efficiency [ε]	χ^2 **Systematic error** [g^4_{10}]
$48.23^{+1.56}_{-1.05}$ %	$g^4_{10}(\min)^{+0.105}_{-0.223}$

Table 8.5: *Systematic errors in g^4_{10} units from the uncertainties of the TPC efficiency.*

CAST systematics In order to give an upper and a lower limit to the systematics of the CAST experiment affecting the final result of the TPC *(see*

table 8.6) we can combine all the previously mentioned systematics and express its effect in terms of g_{10}^4 units or of a percentage to the limit obtained by the TPC.

χ^2 **Systematic error** [g_{10}^4]
$g_{10}^4(\text{min})^{+0.143}_{-0.244}$

Table 8.6: *Systematic errors in g_{10}^4 units from the uncertainties of the CAST experiment.*

8.4.2 Background data

The analysis of the TPC data is highly biased by the background selection criteria and conditions the final result. The background that has been used for the final analysis of the TPC detector corresponds to the Daily definition of *section 8.2.2*. However, the quality of it and the crosscheck of any other possible background applied to the TPC data has been evaluated.

Tracking [counts $\cdot$ keV^{-1} $\cdot$ cm^{-2} $\cdot$ s^{-1}]	**Background** [counts $\cdot$ keV^{-1} $\cdot$ cm^{-2} $\cdot$ s^{-1}]
$4.51959 \times 10^{-5} \pm 2.79348 \times 10^{-7}$	$4.46895 \times 10^{-5} \pm 7.44341 \times 10^{-8}$

Table 8.7: *Level of counts during tracking and background for the TPC detector during the ^{4}He run of the second phase of CAST.*

The accumulated statistics of the TPC detector during the ^{4}He run of CAST allow us to stablish the level of background and tracking counts for the 2 to

12 keV energy range as it appears in the *Table 8.7*.

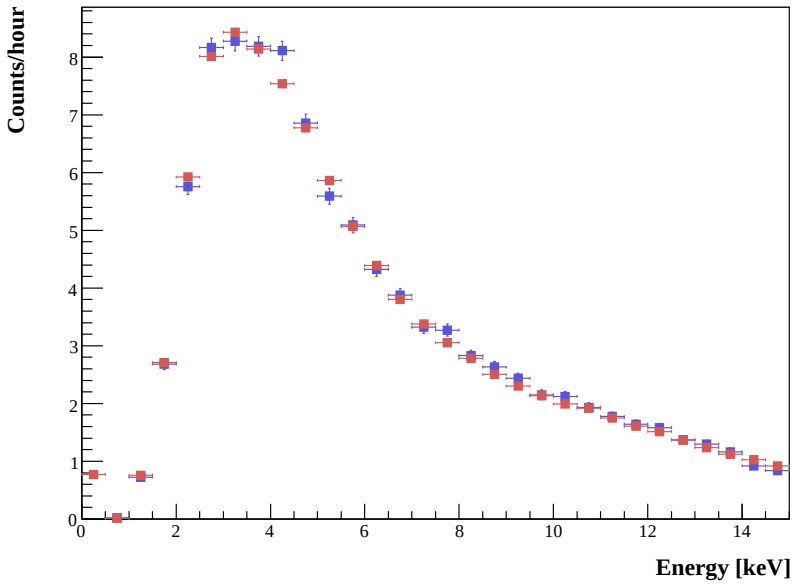

Figure 8.13: *Total statistics for the tracking and background of the TPC detector during the* ^{4}He *run of the CAST experiment.*

Since the TPC of the CAST experiment has another three independent background definitions:

- *Nearby background*
- *Off-coherence tracking*
- *Combined background*

It is natural to attempt the systematic effects studies with the help of all the background definitions and compare each of them in order to see its independent result. In order to check for the quality of the background used, the $\Delta\chi^2_{m_a}$

method has been. The result of this quality check naturally selects the best background candidate to be used for the TPC analysis.

Nearby analysis As it has been shown in *section 8.2.2*, due to slightly variation of the background levels between days, the selection of the background for the j-setting has been such that it includes the statistics of the ten nearest days to the tracking of the specific setting.

This definition provides us with background spectra that can be used as an input for the analysis independently of the final criteria that has been choosen in order to analyze the TPC data.

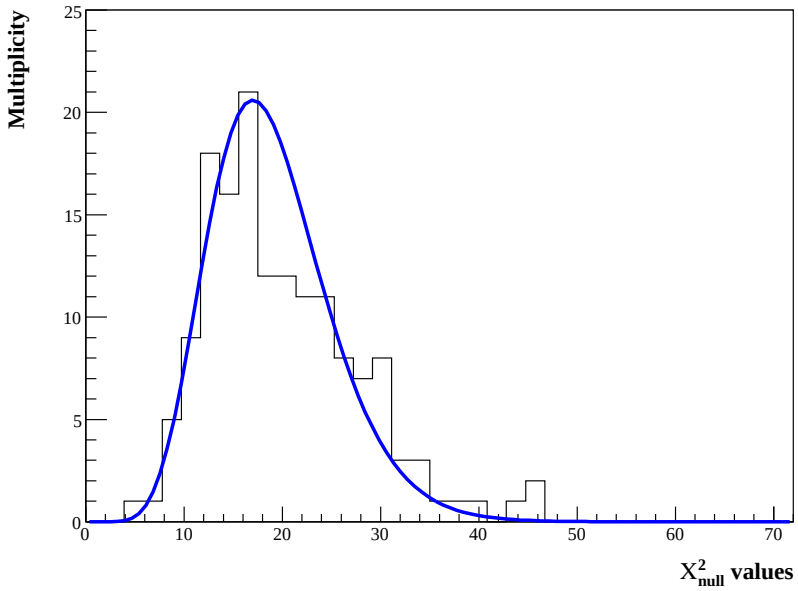

Figure 8.14: *Multiplicity of the $\chi^2_{null,j}$ values of the j-settings (black) versus the theoretical curve (blue) of the Nearby background definition.*

The application of such backgrounds will provide us with the same graphs that

can be seen in *sections 8.3.1 and 8.3.2* and the corresponding crosschecks for the $\chi^2_{null,j}$ of each individual j-likelihood can be generated by using now the Nearby background *(see figure 8.14)*.

Also the global likelihood can be evaluated with the use of the Nearby background, giving us the chance to use the $\Delta\chi^2_{m_a}$ crosscheck method of *equation 8.15* whose result can be seen in *figure 8.15*.

We can observe that a 39.13 % of the data are out of 1σ and a 8.69 % out of the 2σ boundary when we use the Nearby background for the final analysis of the TPC data.

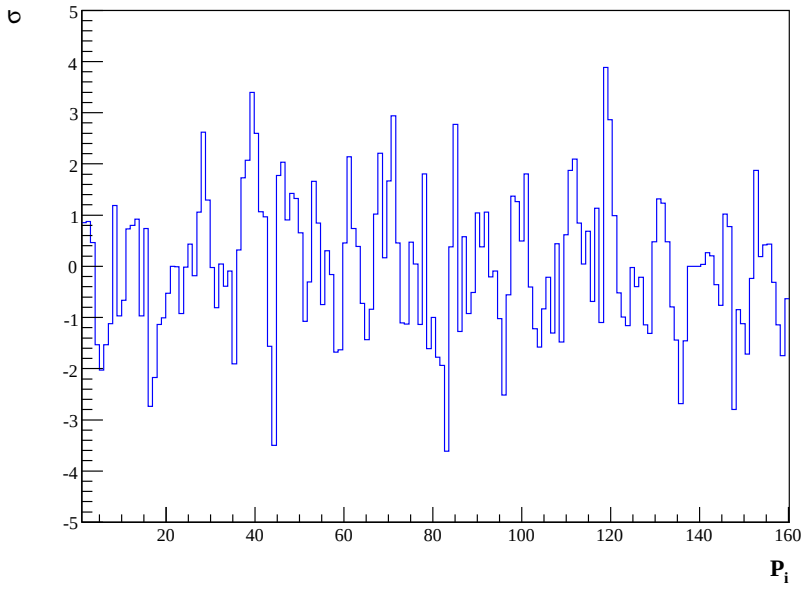

Figure 8.15: *Difference between the χ^2_{min,m_a} and the χ^2_{null,m_a} after the combining of all settings to generate the global likelihood using the Nearby background.*

Off-coherence analysis With its definition detailed in the *section 8.2.2* and, since the procedure of the analysis does not differ from the rest of the cases above mentioned, we can directly proceed to the evaluation of the cross-check plots for the Off-coherence tracking definition. The multiplicity of $\chi^2_{null,j}$ *(see figure 8.16)* and, as in the previous cases, the compatibility of the $\Delta\chi^2_{m_a}$ method *(see figure 8.17)*.

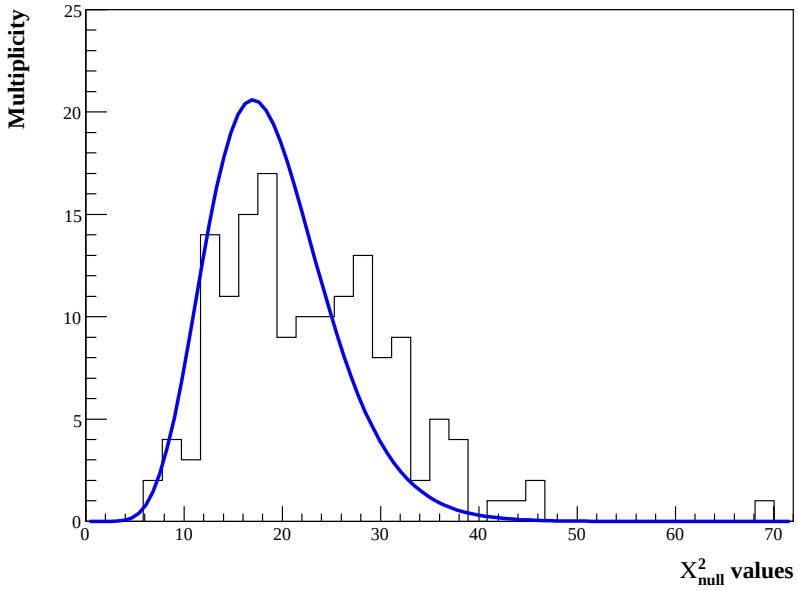

Figure 8.16: *Multiplicity of the $\chi^2_{null,j}$ values for the Off-coherence tracking as background (black histogram) versus $\chi^2_{Th}[d.o.f]$.*

The result from the quality check applied to the Off-coherence definition of background does not follow the expected Gaussian distribution since it has a 54.35 % of the data out of 1σ, and a 20.11 % out of 2σ. we must remember that only a 4.6 % of the data is expected to be out of the 2σ boundary in a Gaussian distribution.

With this result, the Off-coherence tracking definition is the less compatible with the tracking data as it has shown the $\Delta\chi^2_{m_a}$ quality check.

The reason for it is that in an effort of accumulating statistics, the off-coherence range of trackings that contribute to the background are far from the j-tracking of the j-setting is wide, which makes this background to be more sensitive to the daily environmental conditions.

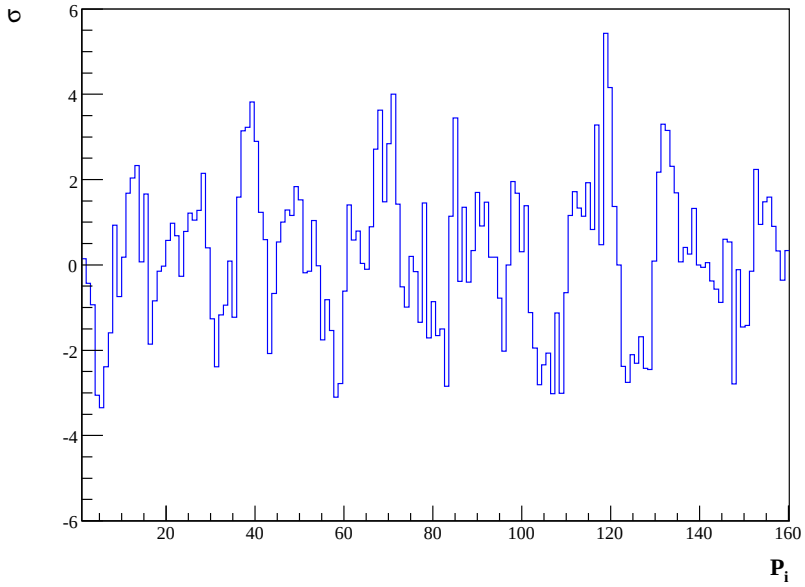

Figure 8.17: *Difference between the χ^2_{min,m_a} and the χ^2_{null,m_a} after the combining of all settings to generate the global likelihood using the Off-coherence tracking as background for the analysis.*

Combined background analysis Furthermore, it is possible to apply the same method to the combination of the two previous backgrounds. This background has been called Combined background in *Section 8.2.2* and gather the

statistics of the Nearby background and the Off-Coherence trackings together for an specific j-setting.

This background has $\simeq$ *228* hours of accumulated statistics and therefore is the one with the smallest error bars $\simeq$ *15* times smaller than the tracking ones.

Figure 8.18 corresponds to the multiplicity distribution of $\chi^2_{null,j}$, while the $\Delta\chi^2_{m_a}$ plot can be seen in *(figure 8.19)*

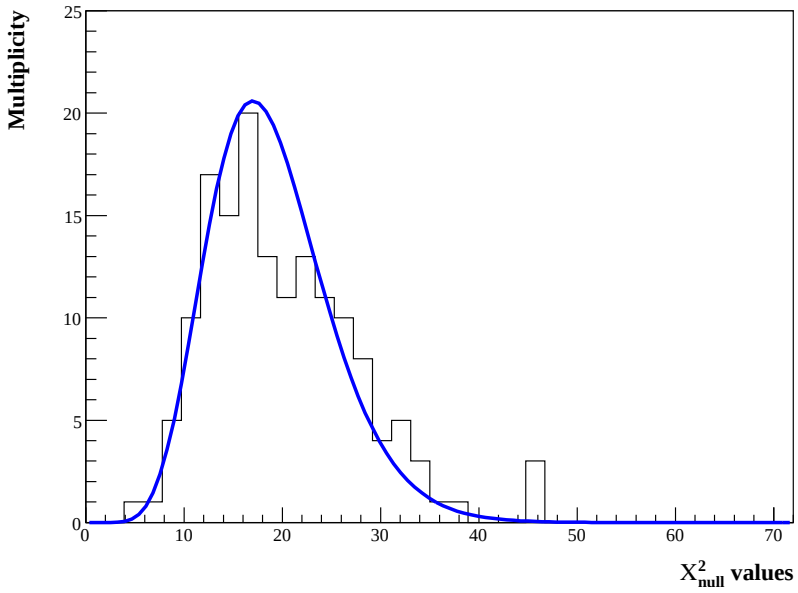

Figure 8.18: *Comparison of the theoretical and obtained $\chi^2_{null,j}$ distribution for the Combined background definition of background analysis.*

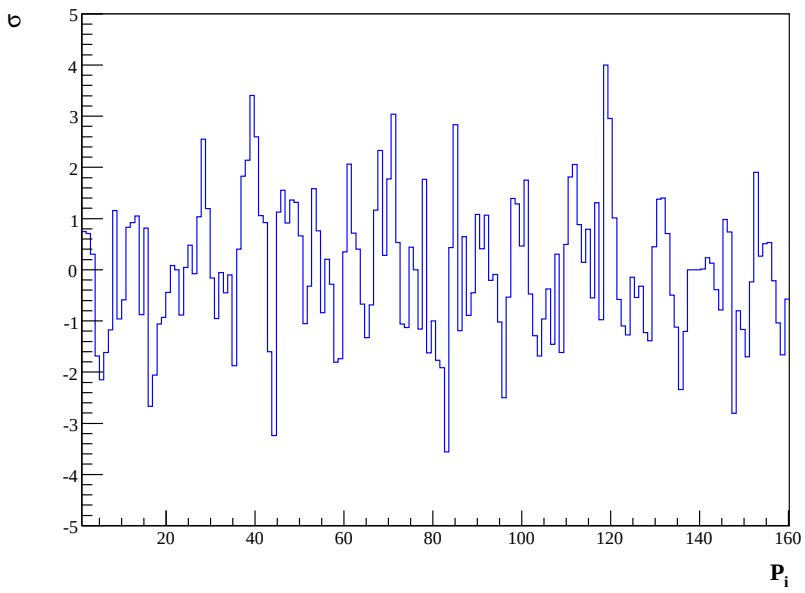

Figure 8.19: *Difference between the χ^2_{min,m_a} and the χ^2_{null,m_a} after the combining of all settings to generate the global likelihood using the Combined background.*

Statistical deviation from the one free parameter statistical distribution A way of showing the results obtained from the different definitions of background can be the representation of the multiplicity of $\Delta\chi^2_{ma}$ for each one of the criterias versus the expected statistical probability density function.

Such plot *(see figure 8.20)* shows how the different background criterias used for the study of the sytematics generate specific probability density functions that are in agreement or not with the statistical expected deviation.

As it has been previously mentioned, the Daily background is the one that agrees better with the expected deviation, something that can be easily understood since it is the one that better follows different daily experimental

conditions. On the other hand, the Off-coherence tracking is the background definition that follows worst the statistical deviation. As a matter of act, the Off-coherence tracking is the less sensitive to the specific experimental conditions of the different j-trackings.

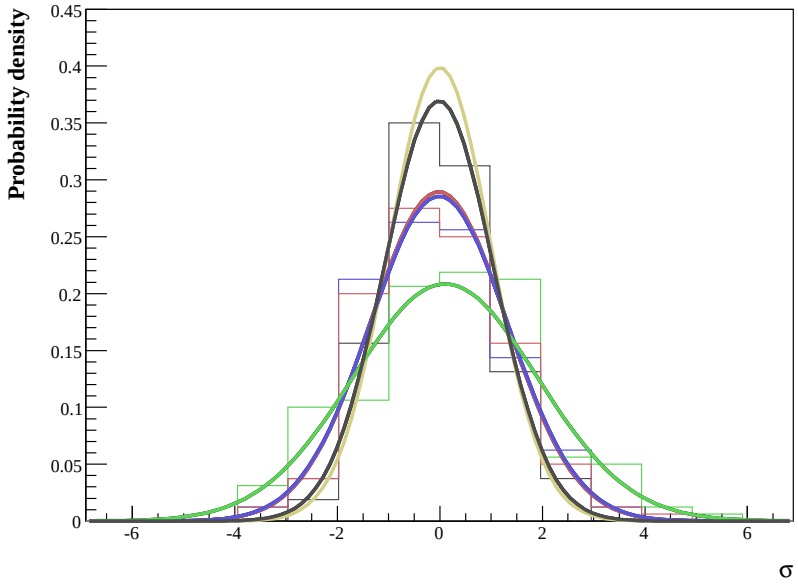

Figure 8.20: *Representation of the different probability density functions that recreate each one of the background criteria chosen for the study of the systematics. In gold and continuous line it can be seen the theoretical statistical deviation, a Gaussian centered at zero and whose FWHM is 1σ. The black line corresponds to the use of the Daily background. The blue line corresponds to the Nearby background definition and the green line to the Off-Coherence background. Also, in red, the cumulative background of the TPC.*

We can conclude then that the Daily background is the one to be use for the TPC detector analysis, since it is the one that better corresponds with the theoretical expectations.

Induced systematics from the background definitions Beside the fact that the $\Delta\chi^2_{ma}$ method has allowed us to choose the Daly background definition among the others, the systematic effect of using different background definitions for the TPC analysis can be quantify. Indeed, for each one of the different background definitions we observe an effective shift for the χ^2_{min,m_a}. Referring the mean shift of the different background definitions relative the the values obtained with the Daily background is an exercise that quantifies the systematic errors arising from the background selection.

	Nearby $[g^4_{10}]$	**Off-coherence** $[g^4_{10}]$	**Combined** $[g^4_{10}]$
χ^2 **Deviation**	$g^4_{10}(\min) + 2.937$	$g^4_{10}(\min) + 3.508$	$g^4_{10}(\min) - 1.243$

Table 8.8: *Mean deviation from the Daily background χ^2_{min} in g^4_{10} units from the uncertainties of the TPC background.*

With the help of *table 8.8* we can now obtain an upper and lower limit for the background induced systematic errors of the TPC analysis. The systematic erros from the background uncertainties are calculated as the mean above and below the minimums obtained for the Daily background with the other definitions of background that have been considered in 8.4.2.

χ^2 **Systematic error** $[g^4_{10}]$
$g^4_{10}(\min)^{+3.222}_{-1.243}$

Table 8.9: *Overall systematic errors in g^4_{10} units from the uncertainties of the TPC induced by the background definitions.*

8.5 Exclusion plot of the TPC

An upper limit to the strength of the axion-to-photon Primakoff coupling has been extracted as result of the TPC detector measurements during the ^{4}He run of the CAST experiment.

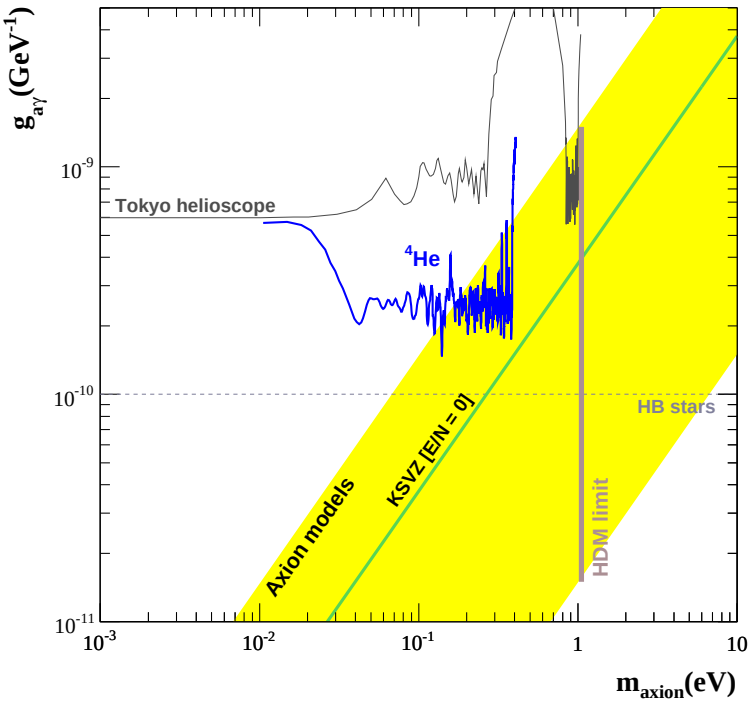

Figure 8.21: *Exclusion plot result for the axion-to-photon coupling measured by the TPC detector during the ^{4}He run of CAST's Second Phase compared with other constraints (Tokyo helioscope [87, 88] and HB stars [10, 47]). The vertical line (HDM) is the hot dark matter limit for hadronic axions $m_a < 1.05\,\text{eV}$ [89] inferred from observations of the cosmological large-scale structure. The yellow band represents the typical theoretical models with $|E/N - 1.95|$ in the range $0.07 - 7$ while the green solid line corresponds to the case when $E/N = 0$ is assumed.*

This upper boundary has been calculated by integrating the Bayesian probability from zero up to 95 % of its area.

Chapter 9

Conclusions

After the data taking of CAST during its ^{4}He run, the TPC detector, a multiwire proportional chamber, is able to present limits to the axion-to-photon coupling via Primakoff effect in the axion mass space parameter.

After crosschecking the tracking and background spectra collected by the TPC during the ^{4}He run of CAST Second Phase, no axion signal has been identified. However, the acccumulated statistics allows to obtain an upper limit for the Primakoff coupling of axions.

Due to coherence restrictions of the axion-to-photon conversion, the axion mass range suitable to study goes from 0.02 to 0.39 eV. This range has also been used by the other two detectors of CAST, which allows to provide the combined exclusion plot of CAST Second Phase.

The compatibility of tracking and background spectra can be done by using the likelihood method. The global likelihood, product of the individual likelihoods of the different pressure settings measured in CAST, is the instrument that has been used in order to obtain the axion mass dependence with $g_{a\gamma\gamma}$, the strength of the coupling.

The TPC analysis scans for different axion masses and obtains the most probable value of $g_{a\gamma\gamma}$ that validates the tracking and background data. A total of 1500 $\chi^2_{m_a}$ have been generated from the data gathered by the TPC. The estimation of the standar deviation errors of the analysis carried out for the TPC data has considered that the χ^2 distributions are not symmetric. Also, the knowledge of experimental uncertainties and the study of the different background definitions has allowed to determine an upper and lower boundary for the systematic errors of the performed analysis. A summary of both, statistical and systematic errors analysis can be seen in the following table:

	Statistical error $[g^4_{10}]$	**Systematic error** $[g^4_{10}]$
TPC	$g^4_{10}(\min)^{+11.921}_{-4.726}$	$g^4_{10}(\min)^{+3.225}_{-1.267}$

Table 9.1: *Statistical and systematic errors in g^4_{10} units for the $g^4_{10}(min)$ result of the TPC.*

An upper limit to the strength of the axion-to-photon Primakoff coupling has been extracted as result of the TPC detector measurements during the ^{4}He run of the CAST experiment. This upper boundary has been calculated by integrating the Bayesian probability from zero up to 95 % of its area and it is dependent with the axion mass, as can be observed in the figure below:

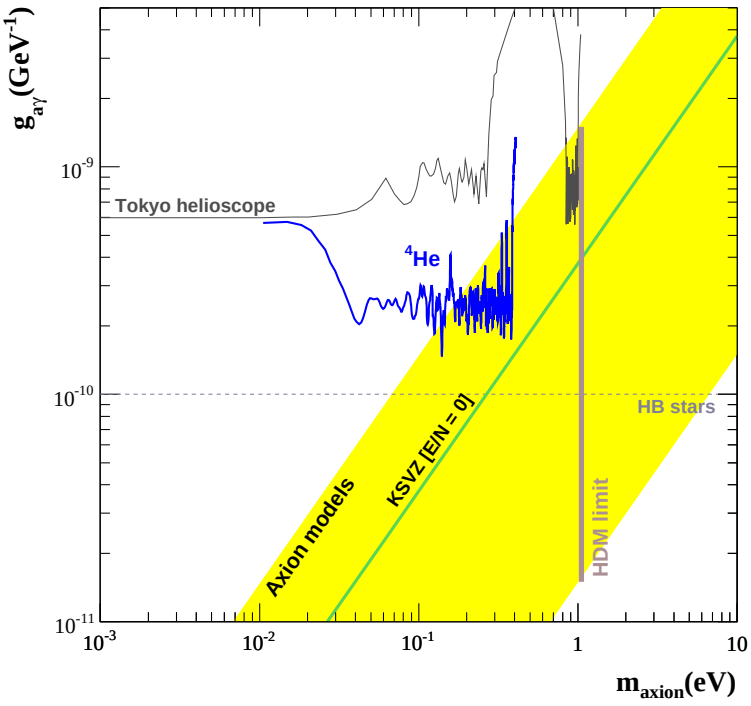

Figure 9.1: *Exclusion plot result for the axion-to-photon coupling measured by the TPC detector during the* ^{4}He *run of CAST's Second Phase compared with other constraints (Tokyo helioscope [87, 88] and HB stars [10, 47]). The vertical line (HDM) is the hot dark matter limit for hadronic axions* $m_a < 1.05$ eV *[89] inferred from observations of the cosmological large-scale structure. The yellow band represents the typical theoretical models with* $|E/N - 1.95|$ *in the range* $0.07 - 7$ *while the green solid line corresponds to the case when* $E/N = 0$ *is assumed.*

The mean of the axion-to-photon coupling litmit overall axion masses between 0.02 and 0.39 eV obtained by the TPC during the ^{4}He run of CAST Second Phase is:

$$g_{a\gamma\gamma}(95\,\%\ C.L) \lesssim 2.57 \times 10^{-10}\,\mathrm{GeV}^{-1}$$
$$0.02\,\mathrm{eV} \lesssim \mathrm{m_a} \lesssim 0.39\,\mathrm{eV}. \tag{9.1}$$

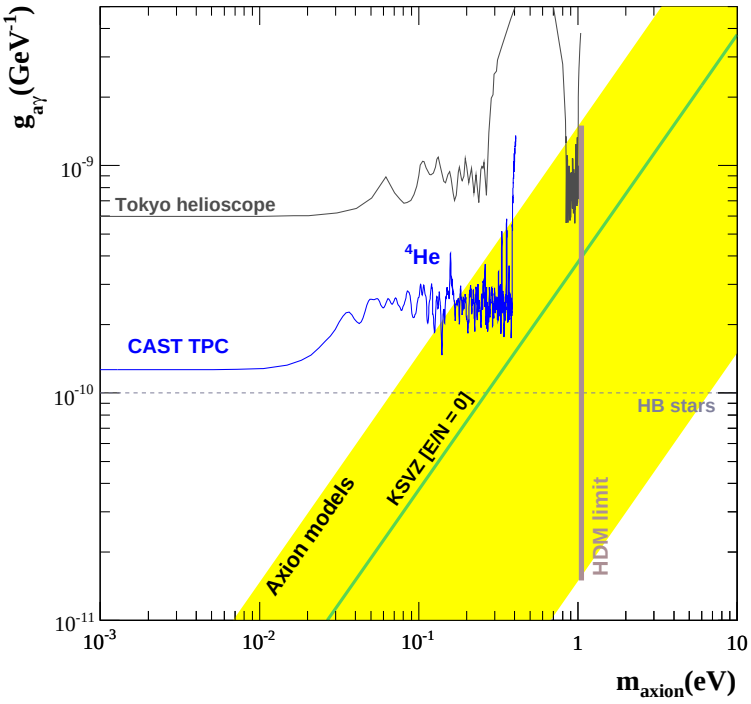

Figure 9.2: *Combined exclusion plot for the TPC detector of the CAST experiment. First and Second Phase of CAST have been included.*

Systematic uncertainties may influence on the best fit value of $g_{a\gamma\gamma}$ and on the upper limit. Studies concerning the background definitions and rates as a function of time, or the ^{4}He pressure inside the magnet bore, have been carried out for the TPC detector. In fact, the background definition used to calculate the final result has been chosen such that minimizes systematics effects. Moreover, the overall effect of the systematic errors on the result obtained by the TPC detector has been quantified and it is smaller than a 9.83 %.

The TPC detector, that during the First Phase of CAST had already contributed to provide the most restrictive laboratory limit on the two-photon coupling of axions and axion-like particles for $m_a \lesssim 0.02\,\mathrm{eV}$, has extended the search for axions up to $m_a \lesssim 0.39\,\mathrm{eV}$. The absence of signal above background excludes a new range in the $g_{a\gamma\gamma} - m_a$ plane not previously explored in laboratory experiments. As result, the TPC is able to set the strongest limit to the axion-to-photon coupling.

Chapter 10

Resumen

CAST (CERN Axion Solar Telescope) es un experimento emplazado en el CERN, un gran laboratorio de partículas situado en Ginebra, Suiza.

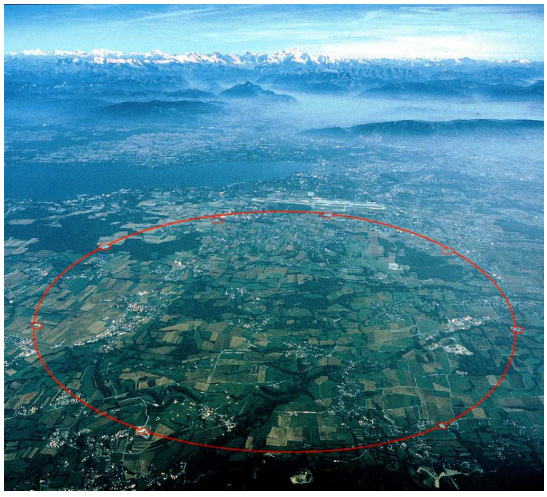

Figure 10.1: *Anillo del LHC en el CERN.*

El telescopio de axiones solares del CERN. Experimento CAST, fase II

El Modelo Estándar de las Partículas Elementales predice que la fuerza fuerte debería violar una de la simetrías fundamentales de la naturaleza, CP (carga-paridad), al igual que lo hace la fuerza débil (lo que se denomina "strong CP problem", o problema CP fuerte en el argot usual), pero hasta la fecha, ningún experimento ha detectado dicha violación, hecho que empezó a intrigar a los físicos de partículas a comienzos de los años 70.

En 1977, R. Peccei y H. Quinn introdujeron en dicho modelo un nuevo mecanismo teórico para preservar dicha simetría en la fuerza fuerte [1] que, hasta la fecha, es la solución más "elegante" al problema. Posteriormente, en 1978 F. Wilczeck [4] y S. Weimberg [3] se dieron cuenta, independientemente, de que, en el marco de esta nueva teoría, esto implicaba la existencia de una nueva partícula, un bosón al que bautizaron con el nombre de axión. Así, un nuevo bosón pseudoescalar entraba a formar parte del ya de por si extenso zoo de las partículas elementales. Su observación experimental permitiría confirmar el mecanismo introducido por Peccei y Quinn.

En principio, esta partícula podría tener cualquier masa, pero consideraciones astrofísicas (velocidad de enfriamiento de las estrellas y explosiones de supernovas) y cosmológicas (nucleosíntesis primordial) han permitido acotar enormemente su valor, de forma que hoy, todos lo experimentos que buscan axiones lo hacen en un rango de masas menor que el electronvoltio.

Este bosón interaccionaría de una forma muy débil con la materia, convirtiéndose así en una partícula muy esquiva. Su observación supone, por tanto, un reto para los físicos, ya que hemos de recurrir a métodos más sofisticados para su búsqueda que los habituales.

Una de las propiedades presentes en todos los modelos de axiones es su conversión en fotones en el seno de un campo magnético. Esto, en 1983, inspiró a P. Sikivie la idea de usar un imán como "telescopio" para poder detectar estas partículas [24]. Como el modelo estándar del Sol predice que esta estrella sería

una fuente muy intensa de axiones, bastaría seguir su movimiento en la esfera celeste con un imán lo más potente posible para poder detectarlos.

El experimento CAST

En la actualidad, hay dos experimentos que tratan de detectar axiones siguiendo al Sol con un imán: CAST y un dispositivo similar, pero de menor eficiencia, instalado en la universidad de Tokio, en Japón.

Figure 10.2: *Imagen del telescopio de axiones del CERN (CAST).*

En la *figura 10.3*, podemos ver una representación esquemática del funcionamiento del telescopio: Los axiones procedentes del Sol pueden convertirse, mediante el efecto Primakoff, en fotones de unos pocos keV al atravesar el intenso campo magnético transversal del imán. Estos rayos X se detectan en el otro lado del imán.

CAST hace uso de un imán superconductor de 9.26 metros de largo capaz de generar un campo magnético de 9 Tesla, diseñado inicialmente como imán de pruebas para el futuro gran colisionador de hadrones, LHC ("Large Hadron Collider"), que se está construyendo en el CERN, Ginebra.

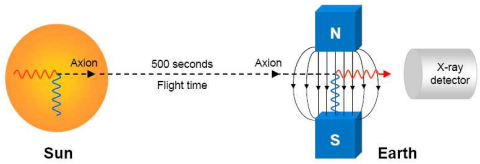

Figure 10.3: *Ilustración del vuelo de un axión generado en el núcleo del Sol viajando hasta la Tierra. En la Tierra, CAST y su campo magnético son capaces de convertir éste axión en fotones de rayos X. Con la ayuda de detectores, CAST es capaz de distinguir cuántos axiones llegan a la Tierra.*

La distribución energética diferencial de axiones en la superficie terrestre sigue la *figura 10.4* .

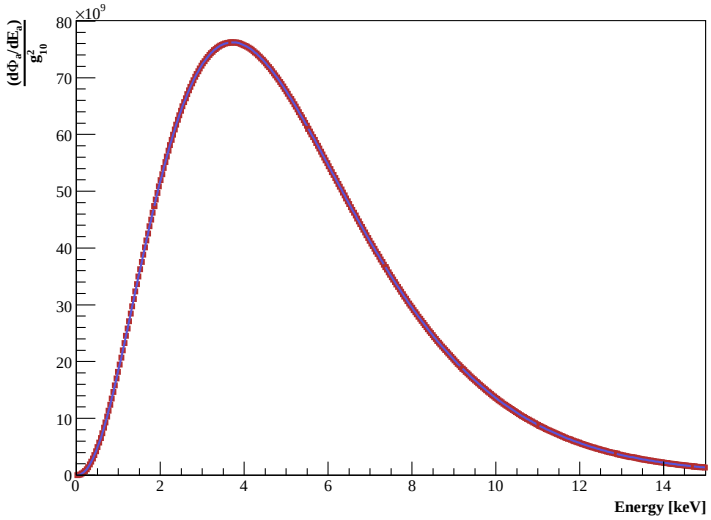

Figure 10.4: *Distribución diferecial de axiones en la superficie terrestre.*

El efecto Primakoff se produce en el interior del imán, pero la coherencia de la conversión limita la observación de los rayos X producidos en el seno del campo magnético. Este fenómeno no es sino la probabilidad de que un axión que sufre el efecto Primakoff salga con el ángulo y velocidad de propagación apropiados para llegar a los detectores de rayos X ubicados en los extremos del imán. El fenómeno está directamente relacionado con la masa del axión incidente.

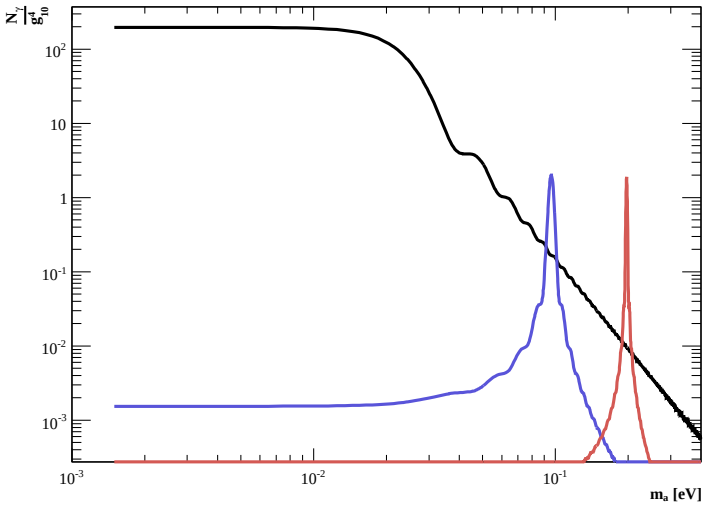

Figure 10.5: *Ejemplo de dos presiones diferentes de* ^{4}He *para las que se restablece la coherencia de la conversión Primakoff en CAST (líneas roja y azul) en comparación con el rango de masas del axión en el que CAST era coherente durante la primera fase del experimento (línea negra).*

La primera fase del experimento CAST tuvo lugar durante los años 2003 y 2004. La condición de coherencia de CAST fase I, es válida para masas del axion de hasta 0.02 eV. Por tanto, la probabilidad de detectar un fotón en los detectores de rayos X disminuye drásticamente cuando se consideran masas de axiones superiores a 0.02 eV. La *figura 10.5* muestra cómo la sensibilidad de la TPC, uno de los detectores de CAST disminuye conforme la masa de los

axiones supera los 0.02 eV.

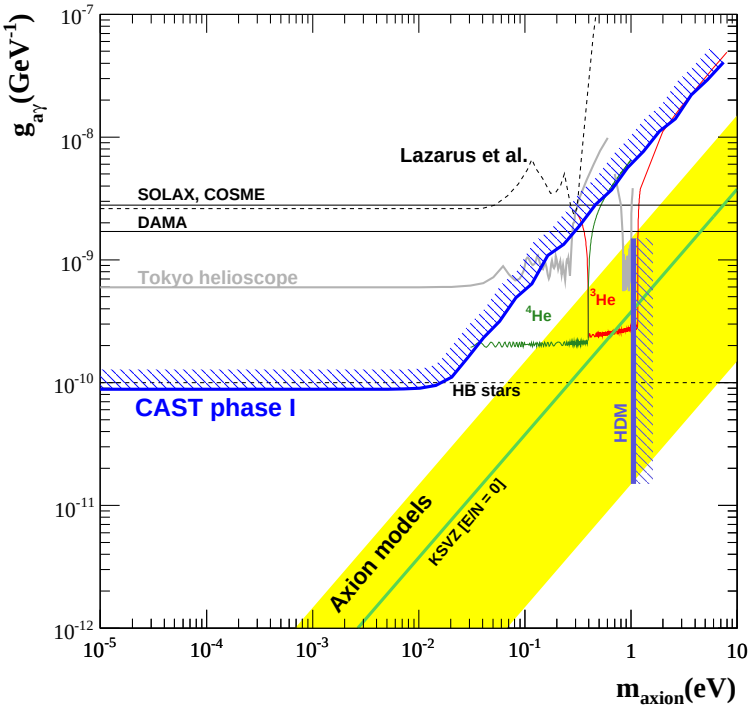

Figure 10.6: *Gráfica de exclusión combinada de la constante de acoplo axión-fotón obtenida durante la primera fase de CAST.*

En la primera fase de CAST, la ausencia de señal de axiones sobre el fondo experimental permitió la obtención del límite para la constante del acoplo axión-fotón. El límite, $g_{a\gamma\gamma} \lesssim 8.8 \times 10^{-11}\,\mathrm{GeV}^{-1}$, se calculó al 95% de confianza para axiones con $m_a \lesssim 0.02\,\mathrm{eV}$ [68].

La fase II de CAST trata de solucionar la pérdida de sensibilidad para axiones más pesados. Dado que la coherencia es dependiente de la masa del fotón generado en la conversión Primakoff, CAST fase II ha creado un sistema capaz

de albergar gases tales como ^{4}He ó ^{3}He. En el seno del campo magnético de 9 Tesla de CAST un posible fotón generado en la conversión Primakoff adquiere una masa efectiva capaz de restaurar la coherencia de la misma. El uso de ^{4}He permite a CAST adentrarse en la región teórica de masas para las cuales el axión solucionaría el problema de violación fuerte CP. Debido a las limitaciones técnicas del experimento, la coherencia de la conversión con ^{4}He está limitada a axiones de masas inferiores a 0.39 eV y es necesario recurrir a un gas más ligero, el ^{3}He, para extender la coherencia de CAST hasta masas de 1.20 eV.

CAST fase II es capaz de contener el Helio en el seno de un campo magnético de 9 Teslas mediante la utilización de ventanas de 15 μm de polipropileno sobre un soporte de acero inoxidable permite contener los gases anteriormente mencionados con fugas de Helio del orden de 10^{-9} mbar/l sec. Es de reseñar que valores de fuga de órdenes superiores harían que el experimento fuera inviable, debido al alto costo del gas ^{3}He.

El diseño, fabricación, e instalación de las ventanas en el experimento ha sido todo un éxito y la elección del diseño definitivo de las ventanas corresponde con el diseño más permeable posible al flujo de los rayos X producidos en el interior del imán (transmisión del 85 %) y a su vez el más restrictivo para la difusión de Helio a través de las ventanas.

Figure 10.7: *Imagen de una de las ventanas instaladas en CAST para la contención del Helio gas en el campo magnético de CAST.*

El detector TPC

El grupo de Física Nuclear de Zaragoza ha sido el encargado del mantenimiento y análisis de los datos de uno de los tres detectores que han medido en CAST con ^{4}He: una cámara de multi-hilos de proyección temporal.

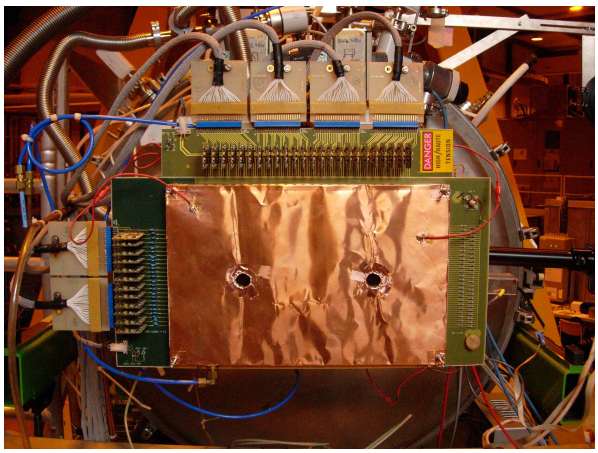

Figure 10.8: *Imagen del montaje experimental de la TPC en el experimento CAST.*

La TPC buscó la posible señal de axiones provenientes del Sol al atardecer durante la toma de datos con ^{4}He del experimento CAST realizada los años 2005 y 2006.

Uno de los objetivos de ésta tésis ha sido la completa caracterización electrónica del sistema de adquisición de la TPC, así como la optimización del mismo para ser competitivo durante la toma de datos con ^{4}He. Dada la existencia de gas en el seno del campo magnético de CAST y la estadística de Poisson de la toma de datos, los programas de análisis usados durante la primera fase han sido modificados consecuentemente. Las condiciones de coherencia para cada uno de los gases mencionados con anterioridad varía en función de la presión y temperatura, parámetros que han sido incluidos en el análisis de los datos.

Para la correcta comprensión de la TPC así como para la optimización del blindaje se han realizado simulaciones con GEANT4 [61,65].

Resultados

Tras la toma de datos y posterior análisis, la TPC de CAST no ha descubierto ninguna señal de axiones con masas inferiores a 0.39 eV. La ausencia de señal, sin embargo, permite la obtención de un límite para la constante del acoplo axión-fotón por medio del efecto Primakoff.

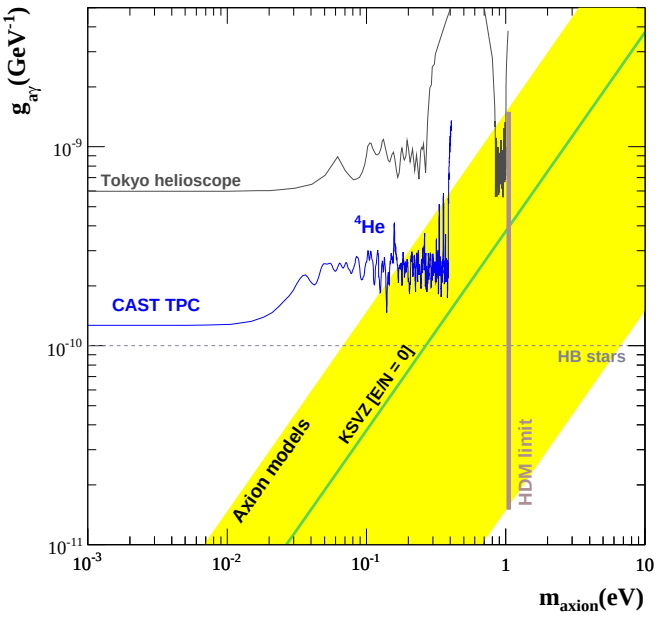

Figure 10.9: *Gráfica de exclusión para la constante de acoplo axión-fotón obtenida durante la primera y segunda fase de CAST con la TPC.*

El uso de ^{4}He en la fase II de CAST es compatible con la ausencia de señal de axiones provenientes del núcleo solar. Por ese motivo, CAST ha preparado al igual que en la primera fase del experimento, el correspondiente límite para cada una de las masas de axiones en las que CAST ha sido capaz de re-establecer la coherencia de la conversión axión-fotón.

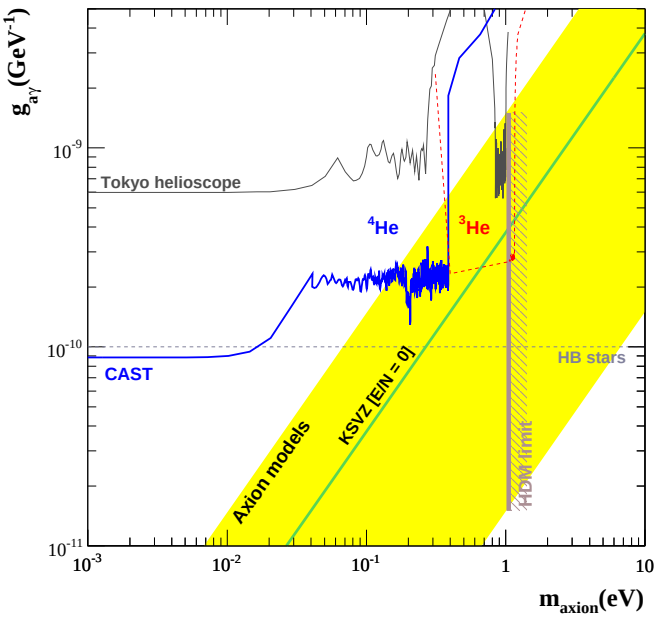

Figure 10.10: *Gráfica de exclusión combinada de la constante de acoplo axión-fotón obtenida durante la primera y segunda fase de CAST.*

Durante esta tésis, se ha formado la base de una colaboración entre el CERN, Saclay y el grupo de la Universidad de Zaragoza que han construido nuevos detectores que han sustituido a la TPC en CAST. Estos detectores (MICROMEGAS) alcanzan un potencial de descubrimento del axión mucho mayor que el de la TPC, hecho que permitirá a CAST mejorar su rendimiento durante la toma de datos con ^{3}He en la segunda fase.

Part IV

Appendix

Appendix A

Heaviside-Lorentz units

The proper study of the probability for an axion-to-photon conversion *(see Equation 4.18)*, requires the unification of units between the magnetic field, the natural mechanical units and the Gaussian electromagnetic units. As a matter of act, we are interested in a unit system for which $(\mathrm{GeV}\cdot\mathrm{m}\cdot 1/\mathrm{T})$ is dimensionless.

Considering the *SI*, the charge of an electron is $e = 1.60217646\times 10^{-19}\cdot\mathrm{C}$, that I will represent as $e = |e|\cdot\mathrm{C}$. Also, the speed of light is $c = 299792458\,\mathrm{m/s}$, but for our considerations I will use $c = |c|\,\mathrm{m/s}$.

$$1\cdot\frac{\mathrm{GeV}}{c} = \frac{10^9\mathrm{eV}}{c} = \frac{10^9\cdot|e|\cdot\mathrm{J}}{|c|\cdot\mathrm{m/s}} = \frac{10^9\cdot|e|\cdot\mathrm{C}\cdot\mathrm{J/C}}{|c|\cdot\mathrm{m/s}} = \frac{e\times 10^9}{|c|}\frac{\mathrm{J}\cdot\mathrm{s}}{\mathrm{C}\cdot\mathrm{m}^2}\cdot\mathrm{m} \tag{A.1}$$

The *SI* defines the magnetic field intesity as a Tesla:

$$1\cdot\mathrm{T} = 1\cdot\frac{\mathrm{N}\cdot\mathrm{s}}{\mathrm{m}\cdot\mathrm{C}} = 1\cdot\frac{\mathrm{J}\cdot\mathrm{s}}{\mathrm{m}^2\cdot\mathrm{C}} \tag{A.2}$$

Equation A.1 can be written then in terms of the magnetic intensity unit as it appears in *equation A.2*. The ratio between GeV and Tesla depends then on the chosen unit system.

$$1 \cdot \frac{\mathrm{GeV}}{c} = \frac{e \times 10^9}{|c|} \cdot \mathrm{T} \cdot \mathrm{m} = \mathrm{e} \times 3.335640952 \cdot \mathrm{T} \cdot \mathrm{m} \tag{A.3}$$

In the natural mechanical units, c is consider as 1. The Gaussian electromagnetic units have $\hbar = c = 1$ with the propierty of making the electric charge dimensionless. In these units the elementary charge is $e = \sqrt{\alpha} = 0.08542453$. The electric charge is also dimensionless in the "natural Heaviside-Lorentz" units, $e = \sqrt{4\pi\alpha} = 0.3028221$.

Gaussian and Heaviside-Lorentz units are different by factors of $\sqrt{4\pi}$. For historical reasons, from now on I will make use of the "natural Heaviside-Lorentz" units that stablishes:

$$1 \cdot \mathrm{GeV} = 1.010105865 \cdot \mathrm{T} \cdot \mathrm{m} \tag{A.4}$$

List of Figures

List of Tables

Bibliography

[1] R.D.Peccei and Helen R. Quinn, *"CP Conservation in the Presence of Pseudoparticles"*. Phys. Rev. Lett. **38** (1977) 1440.

[2] G. 't Hooft, *"Computation of the quantum effects due to a four-dimensional pseudoparticle"*. Phys. Rev. D **14** (1976) 3432.

[3] S. Weinberg, *"A new light boson?"* Phys. Rev. Lett. **40** (1978) 223.

[4] F. Wilczek, *"Problem of Strong P and T Invariance in the Presence of Instantons"*. Phys. Rev. Lett. **40** (1978) 279.

[5] S. L. Adler, *"Axial-Vector Vertex in Spinor Electrodynamics"*. Phys. Rev. **177** (1969) 2426.

[6] J. S. Bell and R. Jackiw,*"A PCAC puzzle: $\pi_0 \to \gamma\gamma$ in the σ - model"* Nuovo Cimento A **60** (1969) 47.

[7] J. Gasser and H.Leutwyler, *"Quark Masses"*. Phys. Rep. **87** (1982) 77.

[8] S. Eidelman *et al, "Review of Particle Physics. Particle Data Group."* Phys. Lett. B **592** (2004) 1.

[9] H. Leutwyler, *"The ratios of the light quark masses"*. Phys. Lett. B **378** (1996) 77.

[10] G. G. Raffelt, *"Stars as Laboratories for Fundamental Physics"*. University of Chicago Press, Chicago/London (1996).

[11] J. Ellis and M. Karliner, *"Determination of $_s$ and the nucleon spin decomposition using recent polarized structure function data"*. Phys. Rev. Lett. **341** (1995) 397.

[12] H. Primakoff, *"Photo-Production of Natural Mesons in Nuclear Electric Fields and the Mean Life of the Neutral Messon"*. Phys. Rev. Lett. **899** (1951) 81.

[13] E. W. Kolb and M. S. Turner, *"The Early Universe"*. Redwood City, USA: Addison-weslay (1990).

[14] R. A. Battye and E. P. S. Shellard, *"Global string radiation"*. Nucl. Phys. B **423** (1994) 260.

[15] M. S. Turner, *"Early-Universe Thermal Production of Not-so-Invisible Axions"*. Phys. Rev. Lett. **59** (1987) 2489.

[16] J. Preskill, M. Wise and F. Wilczek, *"Cosmology of the Invisible Axion"*. Phys. Lett. B **120** (1983) 127.

[17] L. Abbot and P. Sikivie, *"A Cosmological Bound On The Invisible Axion"*. Phys. Lett. B **120** (1983) 133.

[18] G. Bertone, D. Hooper and J. Silk, *"Particle dark matter: Evidence, candidates and constraints"*. Phys. Rept. **405** (2005) 279.

[19] J. E. Kim, *"Light Pseudoscalars, Particle Physics and Cosmology"*. Phys. Rep. **150** (1987) 1.

[20] J. E. Kim, *"Weak-Interaction Singlet and Srong CP invariance"*. Phys. Rev. Lett. **45** (1979) 103.

[21] M. A. Shifman, A. I. Vainshtein and V. I. Zakharov, *"QCD and Resonance Physics: the ρ-ω Mixing"*. Nuc. Phys. B **147** (1979) 519.

[22] A. R. Zhitnitskiĭ, *"On Possible Suppression Of The Axion Hadron Interactions"*. Sov. J. Nucl. Phys. **31** (1980) 260.

[23] M. Dine, W. Fischler, M. Srednicki, *"A Simple Solution to the Strong CP Problem with a harmless Axion"*. Phys. Lett. B **104** (1981) 199.

[24] P. Sikivie, *"Experimental Test of the invisible Axion"*. Phys. Rev. Lett. **51** (1983) 1415.

[25] Y.Semertzidis *et al, "Limits on the production oflight scalar and pseudoscalar particles"*. Phys. Rev. Lett. **64** (1990) 2988.

[26] B.D.Blout *et al, "A Radio Telescope Search for Axions"*. arXiv:astro-ph/0006310v1 (June 2000).

[27] E.Zavattini *et al, "Experimental Observation of Optical Rotation Generated in Vacuum by a Magnetic Field"*. Phys. Rev. Lett. **96** (2006) 110406.

[28] E. Massó and J. Redondo, *"Compatibility of CAST Search with Axion-like Interpretation of PVLAS Results"*. Phys. Rev. Lett. **97** (2006) 151802.

[29] E. A. Paschos and K. Zioutas, *"A Proposal for Solar Axion Detection via Bragg Scattering"*. Phys. Lett. B **323** (1994) 367.

[30] R. J. Creswick *et al, "Theory of the Direct Detection of Solar Axions by Coherent Primakoff Conversion in germanium Detectors"*. Phys. Lett. B **427** (1998) 225.

[31] F. T. Avignone III *et al,* [SOLAX Collaboration] *"Experimental Search for Solar Axions via Coherent Primakoff Conversion in a Germanium Spectrometer"*. Phys. Rev. Lett. **81** (1998) 5068.

[32] A. Morales *et al,* [COSME Collaboration] *"Particle Dark Matter and Solar Axion Searches with a small Germanium Detector at the Canfranc Underground Laboratory"*. Astropart. Phys. **16** (2002) 325.

[33] R. Bernabei *et al, "Search for Solar Axions by Primakoff effect in NaI Crystals"*. Phys. Lett. B **515** (2001) 6.

[34] S. Cebrian *et al, "Prospects of Solar Axion Searches with Crystal Detectors"*. Astropart. Phys. **10** (1999) 397.

[35] D. M. Lazarus *et al, "Search for Solar Axions"*. Phys. Rev. Lett. **69** (1992) 2333.

[36] K. van Bibber *et al, "Proposed experiment to produce and detect light pseudoscalars"*. Phys. Rev. Lett. **59** (1987) 759.

[37] R. Cameron *et al, "Search for nearly massless, weakly coupled particles by optical techniques"*. Phys. Rev. D **47** (1993) 3707.

[38] F. Hoogeveen and T. Ziegenhagen, *"Production and detection of light bosons using optical resonators"*. Nucl. Phys. B **358** (1991) 3.

[39] G. Ruoso *et al, "Search for photon regeneration in a magnetic field"*. Z. Phys. **56** (1992) 505.

[40] P. Pugnat *et al, "Feasibility study of an experiment to measure the vacuum magnetic birefringence"*. Czech. J. Phys. **55** (2005) A389.

[41] R. Ballou *et al, "CERN Report CERN-SPSC-2007-039"*. SPSC-M-762 (2007).

[42] A.Afanasev *et al, "New Experimental limit on Optical Photon Coupling to Neutral, Scalar Bosons"*. arXiv.org/pdf/0806.2631v1 (2006).

[43] R. Rabadan *et al, "Photon regeneration from pseudoscalars at X-ray laser facilities"*. Phys. Rev. Lett. **96** (2006) 110407.

[44] K. Zioutas *et al, "A decommissioned LHC model magnet as an axion telescope"*. Nuclear Instruments and Methods A **425** (1999) 480.

[45] K. Zioutas *et al,* [CAST Collaboration] *"First Results from the CERN Axion Solar Telescope"*. Phys. Rev. Lett. **94** (2005) 2130.

[46] K. Zioutas *et al,* [CAST Collaboration]*"An Improved Limit on the Axion-Photon Coupling from the CAST Experiment"*. JCAP **04** (2007) 010.

[47] G. G. Raffelt, *"Astrophysical Axion Bounds"*. arXiv:hep-ph/0611350v1 28 Nov 2006.

[48] G. G. Raffelt and A. Weiss, *"Red Giant Bound on the Axion-Electron Coupling Revisited"*. Phys. Rev. Lett. D **51** (1995) 1495.

[49] R. L. Davis, *"Cosmic Axions from Cosmic Strings"*. Phys. Lett. B **180** (1986) 225.

[50] L. D. Landau and E. M. Lifshitz, *"Statistical Physics"*. Addison-Wesley, Reading, Mass. (1958).

[51] P. Debye and E. Hückel, *"On the Theory of electrolytes"*. Physikalische Zeitschrift **24** (1923) 185.

[52] E. E. Salpeter, Aust. J. Phys. **7** (1954) 373.

[53] D. D. Clayton, *"Principles of Stellar Evolution and Nucleosynthesys"*. McGraw-Hill, New York (1968).

[54] G. G. Raffelt and L. Stodolsky, *"Mixing of the photon with low-mass particles"*. Phys. Rev. Lett. D **37** (1988) 1237.

[55] J. Bahcall *et al, "Standard solar models and the uncertainties in predicted capture rates of solar neutrinos"*. Rev. Mod. Phys. **54** (1982) 767-799.

[56] K. van Bibber *et al, "Design for a practical laboratory detector for solar axions"*. Phys. Rev. D **39** (1989) 39.

[57] N. F. Ramsey, *"Electric Dipole Moment Of The Neutron"*. Ann. Rev. Nucl. Part. Phys. **40** (1990) 1.

[58] J. M. Pendlebury *et al, "Fundamental Physics With Ultracold Neutrons"*. Ann. Rev. Nucl. Part. Phys. **43** (1993) 687.

[59] Private communication with Julia Vogel, Freiburg, June 2008.

[60] Private communication with Nuno Alexandre Elias, CERN, June 2006.

[61] J. Ruz *et al, " The TPC shielding of the CAST experiment"*. Journal of Physics: Conference Series **39** (2006) 191.

[62] D. Autiero *et al, "The CAST time projection chamber"*. New Journal of Physics **9** (2007) 171.

[63] M. Kuster *et al, "The x-ray telescope of CAST"*. New Journal of Physics **9** (2007) 169.

[64] P. Abbon *et al, "The Micromegas detector of the CAST experiment"*. New Journal of Physics **9** (2007) 170.

[65] G. Luzón *et al, "Background studies and shielding effects for the TPC detector of the CAST experiment"*. New Journal of Physics **9** (2007) 208.

[66] W. N. Hess *et al, "Cosmic-Ray Neutron Energy Spectrum"*. Phys. Rev. **116** (1959) 445.

[67] A. Fassò *et al, Proc. Monte Carlo 2000 Conf. (Lisbon)*. Ed. A. Kling, F. Barao, M. Nakagawa, L. Tavora and F. Vaz (Berlin:Springer-Verlag) (2000) 159 and 955.

[68] K. Zioutas *et al,* [CAST Collaboration] *"An improved limit on the axion-photon coupling from the CAST experiment"*. JCAP journal **04** (2006) 010.

[69] G. Heusser, *"Low-Radioactivity Background Techniques"*. Annu. Rev. Nucl. Part. Sci. **45** (1995) 543.

[70] W. N. Hess *et al, "Cosmic-Ray Neutron Energy Spectrum"*. Phys. Rev. Lett. **116** (1959) 445.

[71] S. Agostinelli *et al, "GEANT4: A Simulation toolkit"*. Nucl. Inst. Meth. A **506** (2003) 250.

[72] B. L. Henke, E. M. Gullikson and J. C. Davis, At. Data and Nucl. Data Tables **54** (1993) 181-342.

[73] L. Musa *et al, "The ALICE TPC Front End Electronics"*. IEEE Nucl. Sci. Symp. Conf. Record **5** (2003) 3647-51.

[74] R. Brun and F. Rademakers, *"ROOT: An object oriented data analysis framework"*. Nucl. Instrum. Methods Phys. Res. A **389** (1997) 81-6.

[75] M. J. Freyberg *et al, "The XMM-Newton Slew Survey"*. Exp. Astron. **20** (2005) 405-12.

[76] J. Altmann *et al, "X-Ray Optics, Instruments and Mission"*. Proceedings of SPIE (1998) 350.

[77] P. Friedrich *et al, "X-Ray Optics, Instruments and Mission"*. Proceedings of SPIE (1998) 369.

[78] L. Strüder *et al, "The European Photon Imaging Camera on XMM-Newton: The pn-CCD camera"*. Astronomy and Astrophysics **365** (2001) L18.

[79] NOVAS, *"Naval Observatory Vector Astrometry Subroutines"*. http://www.usno.navu.mil/, http://aa.usno.navy.mil/software/

[80] JPL, *"Jet Propulsion Laboratory's HORIZONS System"*. http://www.ssd.jpl.nasa.gov/horizons.html.

[81] O. Montenbruck, *"Practical Ephemeris Calculations"*. Springer-Verlag, Heidelberg, Germany (1989).

[82] K. Barth *et al, "Commissioning and first operation of the cryogenics for the CERN Axion Solar Telescope (CAST)"*. AIP Conference Proceeding **710** (2004) 168.

[83] MeteoSwiss, http://www.meteoswiss.ch.

[84] J. I. Collar, *"11th CAST Collaboration Meeting"*. CERN (March 2001).

[85] J. I. Collar, *"12th CAST Collaboration Meeting"*. Halkidiki (September 2002).

[86] J. Vogel, *"The Precision of the Tracking Systemin Search of Solar Axions"*. Diploma Thesis, Albert-Ludwigs-Universität. Freiburg im Breisgau (2005).

[87] S. Moriyama *et al, "Direct search for solar axions by using strong magnetic field and X-ray detectors"*. Phys. Lett. B **434** (1998) 147.

[88] I. Inonue *et al, "Search for sub-electronvolt solar axions using coherent conversion of axions into photons in magnetic field and gas helium"*. Phys. Lett. B **536** (2002) 18.

[89] S. Hannestad, A. Mirizzi, G. G. Raffelt and Y. Y. Y. Wong, *"Cosmological constraints on neutrino plus axion hot dark matter"*. JCAP **0708** (2007) 015.